

Contributions to the Xenon dark matter experiment

**Simulations of detector response to calibration sources
and electric field optimization**

Ricardo José Mota Peres

Dissertation submitted to the Faculty of Science and Technology of the
University of Coimbra
for the degree of Master in Physics under the supervision of
Doutor Fernando Amaro

September 2018



**UNIVERSIDADE DE
COIMBRA**

**FACULDADE
DE CIÊNCIAS
E TECNOLOGIA**

Abstract

Dark Matter (DM) still stands as one of the great mysteries of current day Physics, fueling massive experimental and theoretical endeavors to understand its behavior and properties. The XENON detectors aim to directly detect these elusive particles, mostly focusing on Weakly Interactive Massive Particles, or WIMPs, in a large volume of liquid Xenon, using double phase time projection chamber (TPC) detectors. Since its latest results were published, the XENON1T detector stands as the most sensitive Dark Matter experiment up to date.

In this work, a journey through the evidences on the existence of Dark Matter in the Universe and some of its most notorious models leads to a presentation of the current generation XENON1T detector and, later on, the next generation XENONnT detector. The core of this dissertation focuses, at first, on the simulation and analysis of neutron generator (NG) nuclear recoil (NR) calibration data from the XENON1T detector. Here, a full simulation of a NG calibration run is computed and its results compared with data taken with the XENON1T detector. A separate analysis of other NR calibration data to look into the NR band model and its empirical fit is achieved. Later, in the last chapter, the focus changes to the construction of the geometry model and electric field finite-element simulation of the XENONnT TPC. The main objective is to optimize the resistive chain that ensures the uniformity of the field inside the TPC, changing the geometry and voltage of the field shaping rings, preliminary based on the design used for XENON1T.

Sumário

A Matéria Escura continua a ser dos maiores mistérios do atual mundo da Física, potenciando imensos esforços no estudo do seu comportamento e das suas propriedades, tanto a nível experimental como teórico. Os detetores XENON tentam detetar de forma direta estas esquivas partículas, focando-se principalmente nas Partículas Pesadas que Interagem por Força Fraca, ou WIMPs, em grandes volumes de Xenon líquido com detetores de Câmaras de Projeção Temporal (TPC) de dupla fase. Desde a publicação dos seus últimos resultados, o detetor XENON1T é reconhecido como a mais sensível experiência de Matéria Escura.

Neste trabalho, enumeram-se as principais evidências da existência de Matéria Escura no Universo e alguns dos seus mais reconhecidos modelos teóricos, passando depois à apresentação do detetor XENON1T e, de seguida, do futuro detetor XENONnT. O principal foco desta dissertação é, numa primeira instância, a simulação e análise de calibrações de recuos nucleares (NR) com um gerador de neutrões (NG), feitas no detetor XENON1T. Uma simulação de todo o detetor é feita para estudar o comportamento esperado e os resultados de análise comparados com os resultados em dados do detetor real. Mais ainda, é de seguida feita uma análise a outras campanhas de calibração com o NG de forma a estudar e modelar a banda de recuos nucleares. Mais tarde, no último capítulo, o foco muda para a construção do modelo geométrico e simulações de elementos finitos de campo elétrico da TPC do detetor XENONnT. Aqui, o principal objetivo é otimizar a geometria e diferenças de potencial aplicadas aos anéis de deformação do campo elétrico(FSR), responsáveis por o manter o mais uniforme possível dentro da TPC.

Acknowledgements

First of all, I would like to thank my supervisor, Professor Doutor Fernando Amaro, for his guidance, support and trust throughout the last two years and during the writing of this dissertation. I would also like to deeply thank Prof. Dr. José Matias Lopes for inviting me and letting me be part of something greater than I could have dreamed of, as well as Prof. Joaquim Santos for inviting me to be part of LIBPhys-UC, or GIAN, among friends.

I would like to thank the jury of this dissertation Prof. Dra. Filipa Soares, Prof. Dr. Alexandre Lindote, Prof. Dr. Carlos Azevedo and, my supervisor, Prof. Dr. Fernando Amaro.

A word of gratitude to all members of GIAN for their welcoming spirit that made working in the fourth floor a pleasure and rewarding experience.

To my friends Patrícia, David, Rita (x2), Tomás and Maria João. After all this journey over the last five years, may we always keep as out of our minds as in the first day we stepped into DF.

Overtly I thank the XENON Collaboration, for proving each day that everyone is important in some way or another when you want to reach the top. To Julien - the Mighty Panda, Michelle, Alex and Junji, I'll be forever in dept for pushing me into trying to reach further and for everything they taught me about the experiment.

A long distance word to my long term friends, Pedro, Joel, António and Catarina, thank you for your presence and support in a place where we can all call home.

Nearly after 20 years of friendship, to Henrique, the friend with whom too much time is invested to consider going back.

A special word to Leonor, for her patience and wise advices, promptly delivered whenever needed.

To the family of TAUC, Daniel, Rita, Paulo, Inês, Filipa, Bernardo, Ricardo and many others. Thank you for being part of the greatest adventure I have ever lived. I couldn't be more proud of our team in the last four years and everything we have accomplished. Where no one succeeded, we made it happen and a full size amateur symphonic orchestra was born (can that be beaten?).

To my parents, I am truly grateful for teaching me that there is enough time for everything one cares about, even though it might not look like it and for teaching me to fight as hard as possible for what one desires to achieve.

List of Acronyms

CP - Charge-parity

CMB - Cosmic Microwave Background

DM - Dark matter

D-D - Deuterium-deuterium

ER - Electronic recoil

FSR - Field shaping rings

FC - Full-chain

GXe - Gaseous xenon

LXe - Liquid xenon

MOND - Modified Newtonian Dynamics

MC - Monte carlo

NG - Neutron generator

NR - Nuclear recoil

PMT - Photomultiplier tube

PTFE - Polytetrafluoroethylene

QCD - Quantum Chromodynamics

ROI - Region of interest

SR1 - Science run one

SR0 - Science run zero

SD - Spin dependant

SI - Spin independant

SM - Standard model

SUSY - Supersymmetry

TeVS - Tensor-vector-scalar gravity

TPC - Time projection chamber

WIMP - Weakly Interactive Massive Particle

Contents

List of figures	xi
List of tables	xv
1. Sightings of darkness	1
1.1. Introduction	1
1.2. Evidences of dark matter	2
1.3. Dark matter nature and its major particle candidates	5
1.4. The WIMP	7
2. The XENON project for direct dark matter search	13
2.1. Interaction of Radiation with Matter	14
2.2. Gaseous detectors and light signals in noble gases	19
2.2.1. Operation principle of gaseous detectors	19
2.2.2. From interaction to signal	21
2.3. The XENON1T detector	28
2.3.1. The Double-Phase TPC Principle	28
2.3.2. Detector subsystems and TPC	30
2.3.3. Backgrounds	33
3. Simulation and analysis of nuclear recoil calibration with a neutron generator in the XENON1T detector	37
3.1. Nuclear Recoil band calibrations in XENON1T	38
3.1.1. Use of a neutron generator in XENON1T	39
3.2. Simulation of a neutron generator run	41
3.2.1. The XENON1T Geant4 model	41
3.2.2. Simulation results	43
3.3. Calibration data analysis and data-mc matching study	45
3.3.1. Neutron generator data taken during SR1 and analysis cuts	45

3.3.2.	Data-MC matching and cut acceptance comparison	50
3.3.3.	Post-SR1 NG data analysis	64
4.	Electric field simulations for XENONnT	75
4.1.	Upgrading the search equipment	76
4.1.1.	Physics reach	76
4.1.2.	TPC and cryostat	77
4.1.3.	Purification and storage	79
4.1.4.	Calibration	80
4.1.5.	DAQ and computing	80
4.2.	Electric field simulations of the TPC and field shaping rings optimization	81
4.2.1.	Geometry model of the XENONnT TPC	81
4.2.2.	Study of field shaping rings	83
5.	Final Remarks	93
5.1.	Conclusion	93
5.2.	Future work	95
A.	Simulation and Analysis environment	97
A.1.	Simulation framework	97
A.2.	Analysis framework	98
A.2.1.	Data from simulation	98
A.2.2.	Data from the XENON1T detector	101
	Bibliography	105

List of figures

1.1. Velocity distribution curve of the NGC 3198 galaxy; Coma Galaxy Cluster	3
1.2. Planck 2015 temperature power Spectrum	5
1.3. Freeze out of WIMP particles	8
1.4. Feynman diagrams for SI and SD WIMP scatters	10
1.5. Current limits on SI and SD WIMP-nucleon cross sections	11
2.1. Bragg peak dependence on radiation	15
2.2. Attenuation of different the different photons-matter processes sketched and in Xenon	16
2.3. Photoelectric process	17
2.4. Compton scattering process	18
2.5. Operating regions of gaseous/liquid detectors	19
2.6. WIMP-nucleon interaction rates for different target materials	22
2.7. Waveform from XENON1T	25
2.8. ER and NR photon and charge yields	27
2.9. Dual-Phase TPC principle	29
2.10. S2/S1 discrimination	30
2.11. XENON1T TPC	31
2.12. Rn222 decay chain and emanation from XENON1T components	35
2.13. ER background in XENON1T	36

2.14. NR background in XENON1T	36
3.1. NR calibration events during SR1	38
3.2. Total detection and selection efficiency for WIMP-like NR events . . .	39
3.3. NG positions inside the water tank	40
3.4. GEANT4 geometry model of XENON1T	41
3.5. NG neutron energy spectrum	43
3.6. Energy spectrum of particles reaching the cryostat	44
3.7. Spacial distribution and energy spectrum of NG simulated particles . .	46
3.8. Spatial distributions of DM search data during SR0+SR1	49
3.9. Spatial distribution of FC MC reconstructed events	53
3.10. Spatial distribution of real NG data reconstructed events	54
3.11. $cS2/cS1$ spectrum of MC and real data NG reconstructed events	55
3.12. Spacial distribution and $cS2/cS1$ spectrum of post-SR1 NG runs	66
3.13. Tuning of the distance to source cut threshold.	68
3.14. $cS2/cS1$ vs $cS1$ spectra before and after the <i>distance to source</i> cut application	68
3.15. All three position spectra with the calculated percentiles	70
3.16. Percentiles fit result plots	71
3.17. Comparison between SR0, SR1 and post-SR1 NR medians	73
4.1. XENONnT projected sensitivity	77
4.2. XENONnT TPC drawing	78
4.3. Geometry of the XENONnT TPC	82
4.4. Simulated electric field of the XENONnT detector with 1T FSRs, without tuning	84

4.5. Simulated electric field of the XENONnT detector with 1T FSRs, with tuning	85
4.6. Different FSR geometry simulations	86
4.7. Different FSR T-shaped geometries with bump simulations	87
4.8. Simulated electric field of the XENONnT detector with long T-shape FSRs	88
4.9. Simulated electric field of the XENONnT detector with 145 small T-shape FSRs	89
4.10. Electric-field angle study	90
5.1. The XENON Collaboration	95

List of tables

2.1. W values in liquid rare gases	21
2.2. Background rates in XENON1T	34
3.1. Statistics for a 10M event simulation of a NG run	43
3.2. Coordinates of the NG positions in the water tank	46
3.3. Statistics for simulated and real NG data	51
3.4. Statistics and spectrum of CutInteractionPeaksBiggest	56
3.5. Statistics and spectrum of CutNGFiducial	57
3.6. Statistics and spectrum of CutS2Threshold	58
3.7. Statistics and spectrum of CutS2AreaFractionTop	59
3.8. Statistics and spectrum of CutS2Width	60
3.9. Statistics and spectrum of CutS2PatternLikelihood	61
3.10. Statistics and spectrum of CutS2Tails	62
3.11. Statistics and spectrum of CutS2SingleScatter	63
3.12. Neutron generator runs after SR1	64
3.13. Cut acceptance statistics for NG 2018 runs	65
3.14. Statistics of the <i>distance to source cut</i>	67
3.15. Percentiles fit result parameters	70
4.1. Geometry and voltages of the eletrodes	83

4.2. Distances between electrodes of XENONnT 83

4.3. Details of the most representative FSRs models studied 88

Chapter 1.

Sightings of darkness

“The sky is like a monochromatic contemporary painting, drawing me in its illusion of depth, pulling me up.”

— John Green, in Paper Towns, 2008

Since the dawn of Humanity, the vast Universe, with its countable yet too large to count number of stars in the night sky, has been a mystery everyone is eager to comprehend. Documented studies of the skies go back milenia before modern age, where the first efforts to analyze and describe the movement of astronomical entities were made. Centuries passed, civilizations collapsed and rose, knowledge was lost, recovered and deepened, the Newton’s movement of the planets was mathematically described, the laws of nature began to unveil, Einstein’s relativity was presented, Man went into space, gravitational waves were observed. The accomplishments on the field of astronomy and cosmology are enormous in both quantity and relevance but even now, whenever someone looks up into the sky, only a small percentage of all the matter is known. This unobserved part of the Universe is called dark matter and dark energy.

1.1. Introduction

In this chapter, the groundworks of dark matter theory are discussed: why it is thought it exists, what it is and how can it be detected are the main subjects. Following this premise, some evidences that led to the concept of this non-observed type of matter are

presented in Section 1.2. Section 1.3 focuses in possible dark matter particle candidates and Section 1.4 discusses in more detail one of the most popular models, the WIMP, its interactions with baryonic matter and the approaches taken to detect it.

1.2. Evidences of dark matter

The dark matter problem has been around since the early twentieth century. Its first mention in a scientific journal was due to Fritz Zwicky and his measurement of the velocity and mass of the Coma cluster, in 1933 [1,2]. In his article, Zwicky used the Virial Theorem, that relates kinetic and potential energies in Newtonian systems, to deduce the mass of each galaxy using their velocity dispersion. He found a major discrepancy between the mass values he got from his study and the ones at the time published using the luminous emission of the galaxies, at the order of 400 times bigger than the latter. Amid other explanations, Zwicky proposed the existence of non-luminous matter only revealed by gravitational interaction responsible for the missing mass, that he called *dunkle Materie* [1], or dark matter. In more recent years, many more luminous to velocity mass ratios of galaxy clusters were accurately measured, setting the average difference to around 250 times greater values in favour of velocity masses [3]. Further more, from the same galaxy cluster, pictured in Figure 1.1b, X-ray images have indicated a presence of a large amount of hot gas, explained only by a large dark matter component trapping it inside the cluster with a gravitational potential well.

Some decades later, during the 1970s, another evidence that there is more than luminous matter arose studying the rotation curves of galaxies. As predicted by Newtonian mechanics and Kepler laws, the stars velocity around the galaxy center is given by:

$$v(r) = \sqrt{\frac{GM(r)}{r}} \quad (1.1)$$

where G is the gravitational constant of some particular gravitational system and $M(r)$ the mass of the galaxy inside the radius r measured from its the center. Despite this prediction, Ford and Rubin [4] stated that the data shows a flat distribution of velocities, rather than decreasing with the radius of the galaxy. To explain this phenomenon, galaxies must not only be composed of luminous matter but also of

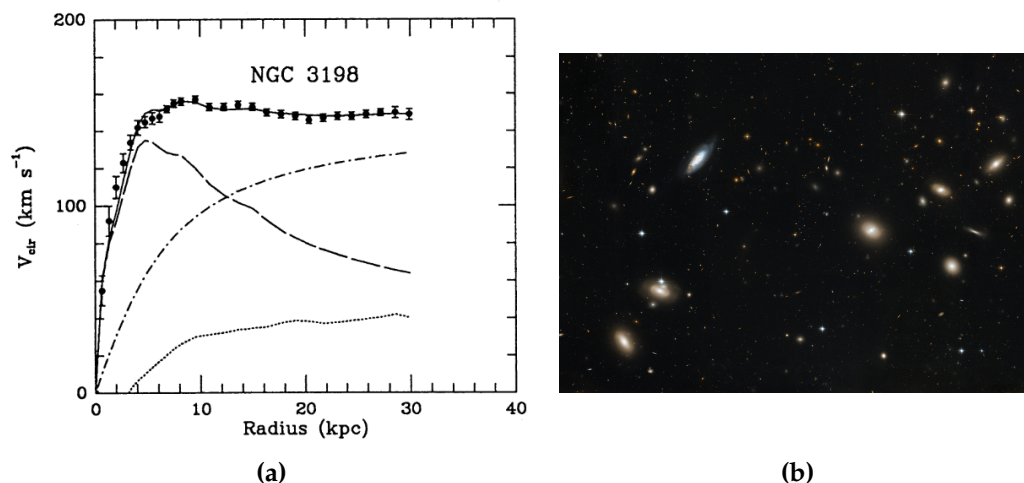


Figure 1.1.: (a) Velocity distribution curve of the NGC 3198 galaxy from [5]. In the figure, the dashed curve corresponds to the visible components for the mass, the dotted curves for the gas and the dash-dot curves to the dark halo. Undoubtedly, only adding the dark halo component the fit agrees with the data points. (b) *The Coma Galaxy Cluster as seen by Hubble*, credit: NASA, ESA, and the Hubble Heritage Team (STScI/AURA).

huge dark halos of matter that do not interact with light, this latter getting as high as 95% of the total mass. In Figure 1.1a the velocity profile of galaxy NGC 6503, where the flat distribution of velocities is shown, as is the fit to data points with the dark matter halo included in the model. As in this example, similar effect has been found in all galaxies studied so far, including the Milky Way.

Another studied evidence of the presence of dark matter in our Universe is given by the effect of Gravitational Lensing. As deduced by Einstein's theory of General Relativity, light, even though massless, is affected by the presence of massive objects, which can act as a lens. This effect can be used to analyze the presence and distribution of mass in galaxies. Contrary to velocity distribution curves, gravitational lensing can be applied to much greater distances, revealing the presence of dark matter up to hundreds of kpc from the center of the galaxy, at least one order of magnitude higher than the first one. All the measurements made with this method seem to lead again into the presence of a non-luminous dark matter acting as a "smooth background component" [6] in addition to the peaks corresponding to the luminous spots of galaxies.

In recent years, yet another hint of the existence of dark matter was gathered from an image of the Bullet cluster, taken by the Chandra X-ray observatory. In what is a

cluster formed by the collision of two galaxy clusters, it is clearly distinguishable the colliding baryonic matter, shaped by friction from the collision (red in Figure 1.2a), and the dark matter, passively not affected by the collision (blue in Figure 1.2a).

All the above stated reasons indicating the presence of dark matter in the Universe fail to deliver a quantification of such existence and are neither of non-local scale. Nonetheless, everything points to luminous matter being only a fraction of the two. This turns out to be entirely true. By 1965, Pezias and Wilson are on their way to discover the Cosmic Microwave Background (CMB) radiation, composed of photons at microwave wavelengths originally form the light-matter decoupling right after the Big Bang. Since then, the temperature of this radiation went down from 3000K to 2.725K due to the Universe expansion. The CMB temperature shows anisotropies of the order of $\delta T/T \sim 10^{-4}$, fluctuations that can be used to infer values for several cosmological values. Figure 1.2b shows the latest results on CMB temperature power spectrum by *Planck*, where the position in angular scale and amplitude of the *acoustic peaks* are used to determine values as the curvature of the Universe, baryon density or dark matter density. The different densities from the *Planck* experiment are [7]:

- $\Omega_b h^2 = 0.02226 \pm 0.00023$
- $\Omega_c h^2 = 0.1186 \pm 0.0020$
- $\Omega_\Lambda h^2 = 0.692 \pm 0.012$

where $\Omega_b h^2$ is the baryonic, $\Omega_c h^2$ the dark matter and $\Omega_\Lambda h^2$ the dark energy densities. From this values, abundances of 4% baryonic, 27% dark matter and 69% dark energy were calculated.

By now, the major observational evidences of dark matter have been mentioned and described. Before moving on it is of importance to note that, while it outreaches the focus of this thesis, the deep theoretical subjects of Cosmological Standard Model (Λ CDM), Einstein's General Relativity and the Friedmann equations are of great importance as they overall agree with the conclusion that there must be some kind of dark matter. Further more, the agreement with the observed values of baryonic, dark matter and dark energy densities is solid. From [8], "*The six-parameter base Λ CDM model continues to provide a very good match to the more extensive 2015 Planck data, including polarization*". For further information on the subject the reader is pointed to [9] and for a challenging model [10].

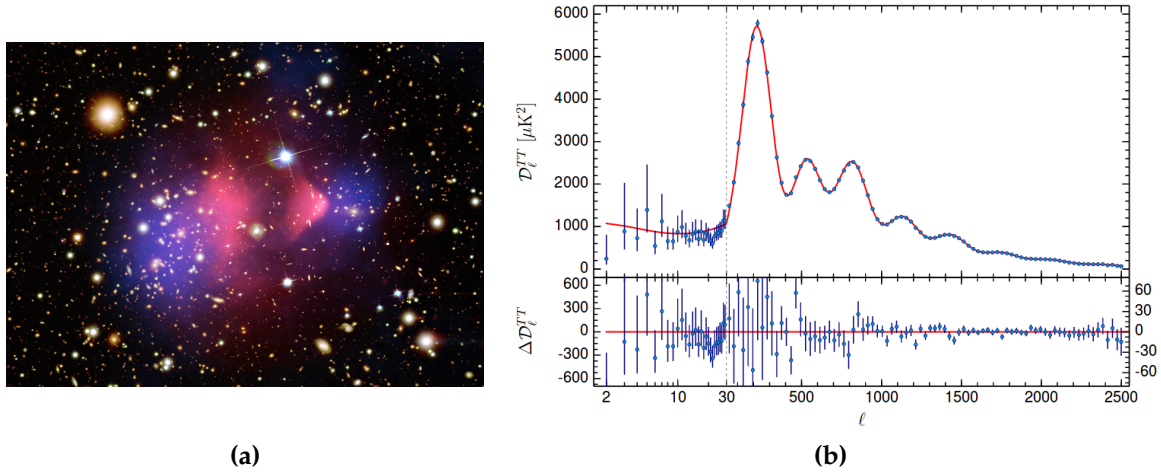


Figure 1.2.: (a) *The Bullet Cluster*, credit: X-ray: NASA/CXC/CfA/M.Markevitch et al.; Optical: NASA/STScI; Magellan/U.Arizona/D.Clowe et al.; Lensing Map: NASA/STScI; ESO WFI; Magellan/U.Arizona/D.Clowe et al. (b) Planck 2015 temperature power spectrum, from [8], with the best-fit to the Λ CDM model.

Although dark matter seems almost inevitable and such a strong case to its existence has been made, little is known about its true nature or exactly how it behaves. Due to the fact that it has never been detected, it can be expected to be neutral, have very low interaction rate with luminous matter and, most likely, to not be baryonic. Then, what can it be? Various answers to this mystery have been suggested across the last decades. In the next Section, the most important ones will be presented and briefly discussed.

1.3. Dark matter nature and its major particle candidates

Different perspectives on how to handle the dark matter nature problem have been discussed since the middle of the twentieth century, from standard baryonic matter and massive neutrinos to an unknown new kind of particle. An alternative to the hidden mass hypothesis is to consider modified models of gravitational laws and Newtonian dynamics, like *Modified Newton Dynamics* (MOND) [11] and its relativistic expansion TeVeS [12]. In despite of their theoretical innovation, both show problems to be overcome. On one hand, the simple MOND paradigm cannot be confirmed on larger scales and, on the other hand, TeVeS can't simultaneously fit observations from gravitational lensing and rotation curves.

Due to its simplicity, the first candidates to solve the dark matter problem were standard massive yet non-luminous objects of baryonic matter, named MACHOs (Massive Compact Halo Objects), like giant planets, black holes, neutron stars, brown stars, among others. In the late nineties, experiments like MACHO [13] and EROS [14] handle this possibility, concluding only 20% of the total dark matter observed in our galaxy could be MACHOs. Moreover, the CMB and the Λ CDM very precise model of the Universe matter densities overall exclude dark matter as a baryonic particle.

Looking into the Standard Model (SM) of Particle Physics, only one particle can be a dark matter candidate: the *neutrino*. It is neutral, has low interaction rate with standard matter and is non-localized. However, observations of atmospheric and Solar neutrinos have given an indication as to its abundance in the Universe, which summed with their very light mass makes them not enough to explain the missing mass. Thus, several candidate particles have been proposed beyond the SM.

The *axion*, proposed by Peccei and Quinn [15], is a light pseudo-scalar particle postulated to solve the *strong CP problem*. The asymmetry between matter and anti-matter in the Universe suggests a violations of charge-parity (CP) in some interactions. As it stands, CP violation was never observed at the Quantum Chromodynamic (QCD) level, giving origin to the *strong CP problem*. The above stated author explains this observation within a QCD model where an axion, acting as a boson, is emitted in order to conserve CP symmetry. As a neutral, very weakly interactive and possibly produced in enough amount, the *axion* is a prime candidate to a dark matter particle. Several experiments were designed to search for it, such as CAST [16], ADMX [17], CASPER [18] or where an *axion* or *axion*-like particle search is possible in LUX [19] and XENON [20].

Also beyond the SM, Supersymmetry (SUSY) has its own dark matter particle candidates. SUSY postulates that every particle has a superpartner with the same properties except mass and opposite spin. SUSY proposes particles like the neutralino and the gravitino, moving away from the subject of this thesis. For those, the reader is led to [21] and [22]

The final particle candidate presented in this work is the Weakly Interactive Massive Particle (WIMP). The term WIMP may emerge as more general than a unique particle, as, for example, the *neutralino* can be considered a WIMP particle. Nevertheless, the search for a hypothetical WIMP particle whose mass can range from 1GeV to 10TeV has been of great importance in the last decades and is the main concern of the XENON

experiments, thereby being the main focus of this work. In Section 1.4 a more in depth look into the nature, interactions and detection of this particle is given.

1.4. The WIMP

The presence of a seemingly low density of WIMPs in the current day Universe can be explained by what is called the *freeze out* model, noting that a major requirement is the WIMP being a stable particle or its half-life bigger than the age of the Universe [23]. In the earliest times after the Big Bang, WIMPs and standard matter were at a thermal equilibrium, meaning that the production and annihilation rates were the same in the interactions $\chi\chi \leftrightarrow SM SM$. As the Universe temperature, T , cooled down below the dark matter mass, m_{χ} , annihilation of WIMPs is preferred over creation, leading to a decrease in the number of dark matter particles, proportional to $e^{-m_{\chi}/T}$. Considering only the process described, the number of particles should continue to decrease until no dark matter was left, but, taking also into consideration the Universe's expansion this does not happen. As the Universe keeps getting larger, the remaining dark matter particles can no longer interact with each other and annihilate, reaching a point of constant relic density, as can be observed in Figure 1.3.

The relic density of DM particles after freeze out can be written as [24]:

$$\Omega_{\chi} \sim \frac{x_f T_0^3}{\rho_c M_{Pl}} \langle \sigma_A v \rangle^{-1} \quad (1.2)$$

where the subscripts f and 0 denote the time at the moment of freeze out and at present day, respectively, ρ_c is the critical density, σ_A the WIMP annihilation cross-section, v is the relative velocity of the particles in the interaction and the brackets, $\langle \rangle$, represent the average over the Boltzmann thermal distribution. Through a dimensional analysis, the cross-section can be written as [24]:

$$\sigma_A = k \frac{g_{weak}^4}{16\pi^2 m_{\chi}^2} \quad (1.3)$$

where $g_{weak} \simeq 0.65$ is the weak interaction gauge coupling and k a parameter to quantify deviations from this estimate. When the expected value for the relic density of dark matter (CMB part in Section 1.2) is considered in the above relations, the calculated masses of the WIMP particles are of the order of GeV – TeV, which perfectly

matches the weak-scale particles masses, and vice-versa. This “coincidence” is named *the WIMP miracle* and merges the WIMP problem for many weak-interacting particle models.

Three major detection techniques have been applied to WIMP search: direct detection, indirect detection and production by collision. As it stands, never a WIMP has been experimentally observed and confirmed by any of these.

The latter, production of dark matter by two SM particles at a collider like the Large Hadron Collider (LHC) at CERN focuses on supersymmetric models for DM, tested by the ATLAS [25] and CMS [26] experiments. The measurements performed by these experiments do not look directly for the presence of a WIMP but for a missing energy on the summed energies of the interaction products, result of the escape of a so produced WIMP. Though a positive result from one of these experiments would open up the possibility for a fermion-like and SUSY WIMP, the lifetime of such particle can not be determined by it, which has to be of the order of the age of the Universe to be consistent with DM.

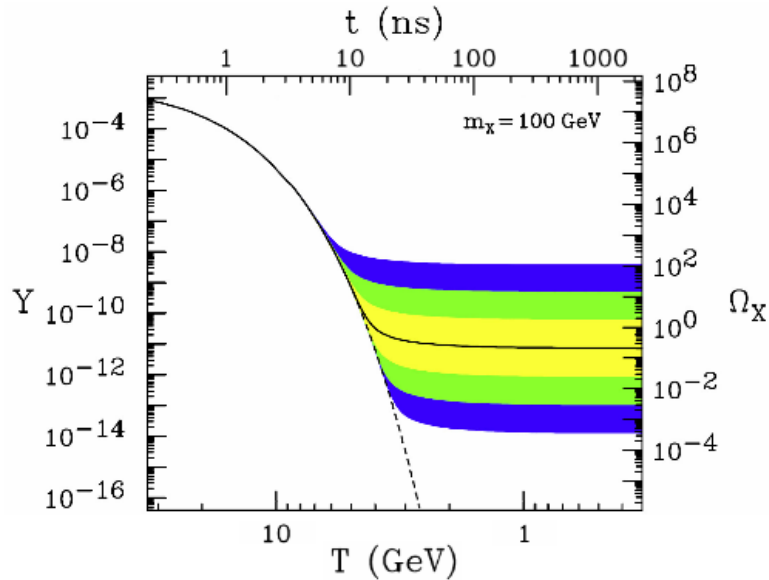


Figure 1.3.: Normalized dark matter density (left axis), and resulting thermal relic density (right axis) given a 100 GeV WIMP particle as function of temperature (bottom) and time (top). The dashed line corresponds to a particle that remains in thermal equilibrium and the solid line is for a frozen out particle with the observed relic density of DM. Shaded region differ from this value by 10 , 10^2 and 10^3

Indirect dark matter detection looks for the products of DM particles annihilation, expected to stay within the SM. DM-DM local interaction rates are surely dependent on DM local density, giving regions with high dark matter density a more suitable environment to annihilate, including galactic centers, white dwarfs or the Sun. Therefore, experimental searches for an excess of SM particles in cosmic rays has been adopted. The nature of the annihilation products, however, is yet to be confirmed as a WIMP-WIMP interaction can theoretically lead to different kind of pairs: $\gamma\gamma$, γZ , γH , $q\bar{q}$, W^-W^+ , ZZ , among other possibilities [27]. Moreover, unstable particles decay into charged particles or other pairs like e^-e^+ from photon interaction with standard matter. All these detection channels must be taken into account as possible indirect measurements of DM in experiments directly in space (FERMI-LAT [28], AMS-02 [29]) or on Earth (Ice-Cube [30], HESS-II [31]).

The remaining detection technique to be discussed in this section is the *direct detection*, which is the one this work focuses in the next chapters. Direct detection of WIMPs looks for their elastic scattering inside a target material, producing nuclear recoils from few keV up to about 100 keV, depending on the scatter medium. A WIMP scatter can be of one out of two ways:

- Spin-Independent (scalar coupling) – The WIMP scatters with a nucleus as a whole with a cross-section simplified as [32]:

$$\frac{d\sigma_{SI}}{dq^2} = \frac{4}{\pi} \mu_\chi^2 [Zf_p + (A - Z)f_n]^2 F^2(q) \quad (1.4)$$

where μ_χ is the interaction reduced mass, f_p and f_n are the coupling constants to protons and neutrons, respectively, Z is the atomic number of the nucleus, A its mass number and $F^2(q)$, being q the recoil momentum, is the nuclear form factor. The latested data published results on SI cross-section limits come from the XENON1T experiment and are pictured in Figure 1.5a.

- Spin-Dependant (axial coupling) – The WIMP scatters either with an unpaired proton or a neutron of the nucleus. The latested data published results on SD neutron coupling and proton coupling cross-section limits come from the LUX experiment and are pictured in Figure 1.5b and Figure 1.5c.

Many techniques can be implemented to a direct search of WIMP particle interactions, as well as many kinds of different detectors. The full discussion of each detection technique is out of the scope of this dissertation but some are mentioned as they are of

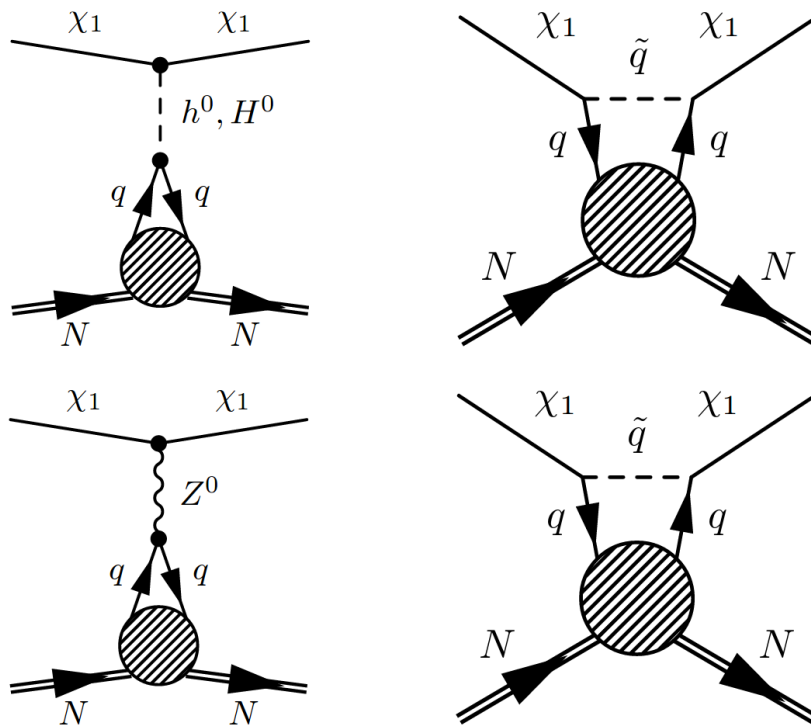


Figure 1.4.: Main Feynman diagrams for Spin-Independent (upper case) and Spin-Dependent (lower case) WIMP-nucleon scattering.

importance to compare results. These are the cases of cryogenic bolometers acting on heat and ionization signals on semiconductors (CDMS [33], EDELWEISS [34] or scintillation signals (CRESST [35]), Argon Time Projection Chambers (TPCs) with one or two phases (DarkSide [36]) and, as a main focus later in this work, Xenon TPCs with one or two phases (LUX and XENON, respectively). All the above mentioned experiments aim to recognize certain events in their detector as a WIMP-like event.

However, a different approach can be taken, considering the Annual Rate Modulation: as the Earth orbits around the Sun, its velocity in relation to the dark matter halo is expected to change over time, therefore changing the rate of WIMP-nucleon interactions measured even if as background inside a target value. This technique has been reason of scrutiny by many experts of the field due to a positive signal for dark matter detection by the DAMA experiment, now upgraded to the DAMA-LIBRA experiment going as far as 12.9σ CL in their latest results [37]. However, other experiments have contradicted this result, observing no events in the Region of Interest. As of the writing of this thesis, this decade long contradictory results still stand as a major challenge in the field.

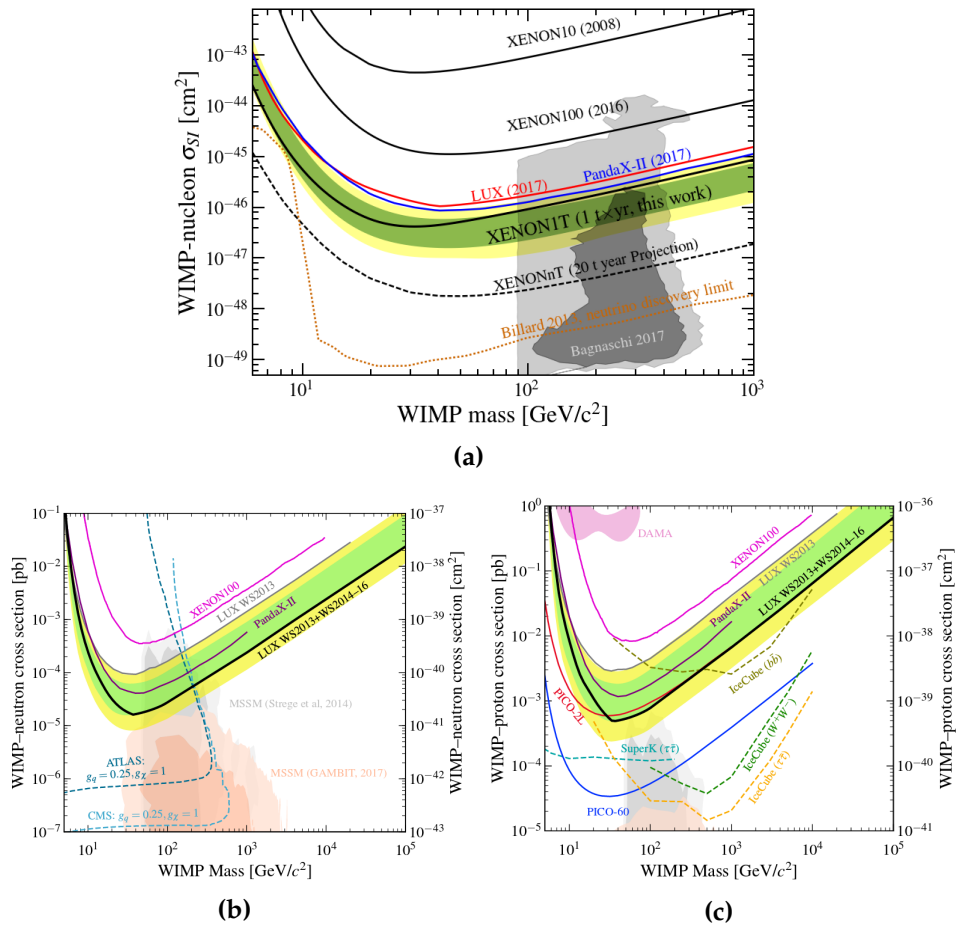


Figure 1.5.: Current limits on (a) SI and SD ((b) neutron and (c) proton) WIMP-nucleon cross sections. Figures from [38] and [39]

In the next chapter, direct search of dark matter with a double-phase Xenon TPC, the XENON1T detector, will be further discussed.

Chapter 2.

The XENON project for direct dark matter search

“It doesn’t matter how beautiful your theory is, it doesn’t matter how smart you are. If it doesn’t agree with experiment, it’s wrong.”

— Richard Feynman, 1918–1988

In the last chapter, different dark matter detection techniques were presented, from indirect measurements to direct recoil analysis (Section 1.4). The XENON project aims to directly identify WIMP signals with double-phase time projection chambers (TPCs) using liquid Xenon (LXe) as the target medium. Due to the expected low recoil energy of WIMP-nucleon interactions in LXe and their very small interaction rate, the detectors must operate within a low-energy threshold and low-background state. In order to accomplish the later, the detectors are located in the caverns of the Gran Sasso Mountain in central Italy, within the facilities of *Laboratorio Nazionale del Gran Sasso* (LNGS). The underground laboratory is under 1300 m of rock (3800 m water equivalent), cutting out most of radio and electromagnetic background abundant at surface level, as well as reducing the muon flux from around 100 to nearly $10^{-4} \text{ m}^{-2} \text{ s}^{-1}$ [40].

In this chapter, an overview of the interactions of radiation with matter is done in Section 2.1, explaining many concepts referenced throughout this dissertation. In Section 2.2 the subject of gaseous detectors and radiation interactions with noble gases and their scintillation and ionization signal responses are presented and discussed, followed by an in depth description of the XENON1T detector and its valencies in Section 2.3.

2.1. Interaction of Radiation with Matter

Radiation can interact with matter in many different ways given different types of incoming radiation as well as the medium where the interaction takes place. Both charged and non-charged particles must be taken into account, giving very different results even for similar energies. Within the charged particles sub-sector the effects vary mainly with their mass, from light β rays to heavy α radiation. In a similar way, non-charged particles effects change from the zero mass photons and the light neutrino to the heavy neutron.

As for the first one, the incident particle loses energy through excitation or ionization of the atoms of the medium. As for the latter, the incident particle is mostly scattered by the intense Coulomb field around the nucleus, usually originating a multiple scattering effect and, due to the accelerated scattered particle, Bremsstrahlung photons. Heavy charge particles deposit their energy mostly in a small range interval, at a determined mean distance from the interface of the medium. On the other hand, light charged particles, like electrons and positrons, begin losing their energy much sooner because the average energy loss per collision is significantly larger. Light particles produce less straight tracks as they are often significantly deflected whenever they collide with nuclei. Moreover, radiative losses (by Bremsstrahlung) are of much greater importance in light particle than heavy particle radiation, supplanting collision losses at the tens of MeVs range.

Many models were developed in the early twentieth century to predict the energy deposition of incoming radiation on a known medium. In the 1930s, Hans Bethe proposed the now called *Bethe's stopping power formula*, which, after considering relativistic corrections for light particles, predicts the energy deposition, $(\frac{dE}{dx})$, of a given radiation in a given medium fairly accurately [41]:

$$-\frac{dE}{dx} = K\rho \frac{Z}{A} \frac{z^2}{\beta^2} \left[\ln \frac{2m_e \gamma^2 c^2 \beta^2 W_{max}}{I^2} - 2\beta^2 - \delta - 2\frac{C}{Z} \right] \quad (2.1)$$

where $K = 2\pi N_a r_e^2 m_e c^2$, ρ is the density of the medium, Z is the atomic number of the target material, A its atomic mass, z is the atomic number of the incident particle, $\beta = \frac{v}{c}$, W_{max} is the maximum energy transferred in a single collision, δ is the relativistic density correction and C is the relativistic shell correction factor.

In Figure 2.1 a sketch plot of the Bragg curves of different radiations is shown for easy visualization. A Bragg curve plots the energy deposition rate versus the distance traveled¹ by the incoming particle. As expected, light particles deposit their energy in broad region along their path, as they interact with different atoms of the target. On the other hand, heavy particles deposit their energy centered around some mean range. Along their path they continuously lose energy and slow down, ionizing the medium and emitting δ -rays (energetic secondary electrons).

Non-charged particles interact very differently as most of the energy of the incoming radiation is deposited in a single event, either being absorbed or largely scattered. Both ways lead to an abrupt change in the radiation path, unlike the ones of charged particles whose energy deposition is much more linear-like throughout the medium.

Photons interact with the detection target via three different processes: the photoelectric effect, Compton scattering and pair production. The probability of either of the above mentioned mechanisms to happen depends on the photon energy and the medium of interaction, as sketched in Figure 2.2a. For low energy gamma radiation (eV-keV) the most probable process is the photoelectric effect: a photon interacts with a bound electron of an atom, transferring all its energy, $h\nu$. The electron, absorbing the energy of the incoming photon, is released with kinetic energy E_{pe} :

$$E_{pe} = h\nu - E_B \quad (2.2)$$

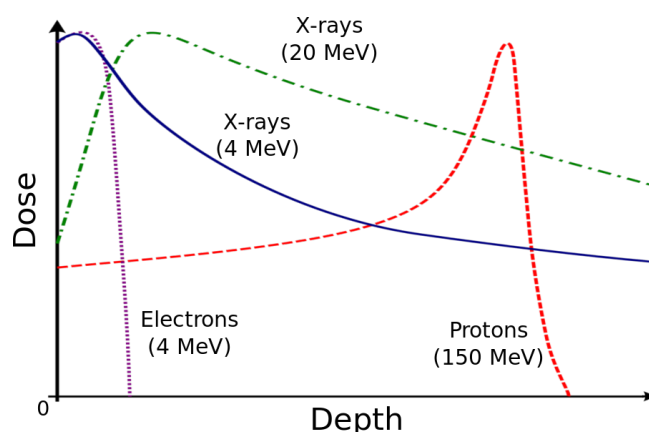


Figure 2.1.: Sketch of the Bragg curves of for different types of radiation.

¹Many remarks must be done regarding how this distance is measured as it can deeply influence the outcome of the Bragg curve. For more information on the subject the reader is directed to [41]

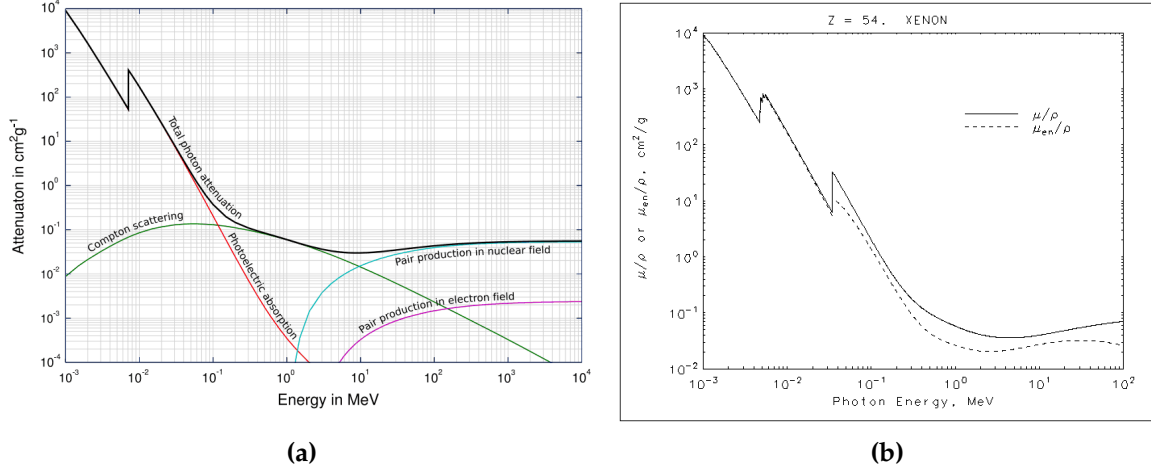


Figure 2.2.: (a) Sketch of the attenuation coefficient for the different photon-matter interaction processes. (b) Attenuation coefficient, μ/ρ , and the mass energy-absorption coefficient, μ_{en}/ρ , as a function of photon energy. Figure from [42]

where E_B is the binding energy of the atomic electron. The emitted electron is usually given the name of *photoelectron* due to its nature. The hole in one of the bound shells of the atom is quickly filled by rearranging the electrons from outer shells or by absorption of a free or bound electron of the medium. In the case of an electron from an atomic orbital, the excess of energy is then used in the production and emission of an X-ray photon with energy $h\nu$ given by²:

$$h\nu = E_B^K - E_B^L \quad (2.3)$$

where E_B^K is the binding energy of a K shell electron and E_B^L is the energy of a L shell electron.

Another possible secondary outcome of a photoelectric interaction is the emission of Auger electrons whenever the emitted X-ray photon interacts with an outer shell electron, depositing its energy and releasing said electron to the medium (Auger electron). The energy of the Auger electrons of an atom are as characteristic as its X-ray photons and their energy given by³:

$$E_{Auger} = (E_B^K - E_B^L) - E_B^L = E_B^K - 2E_B^L \quad (2.4)$$

²For a hole in K shell filled by an electron from the L shell

³For a hole in K shell filled by an electron from the L shell and emission of an Auger electron from the L shell

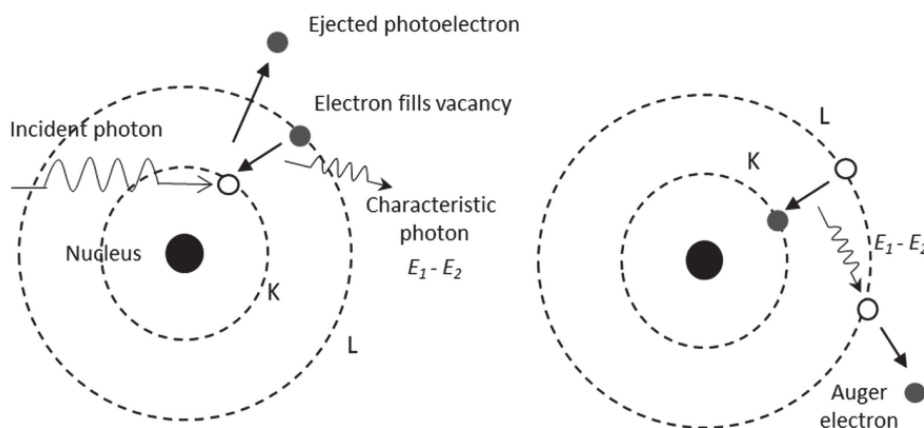


Figure 2.3.: Principle of the photoelectric mechanism, emission of characteristic X-rays (left) and Auger electrons (right). Figure from [43]

In the Compton scattering mechanism, on the other hand, the photon is not absorbed. Instead, it interacts with an outer electron of an atom transferring only part of its initial energy. As long as the energy transferred is greater than the binding energy of the electron, E_B , the electron is extracted from the atom (see figure Figure 2.4. Applying conservation of energy and momentum to the photon-electron system one can find the energy of both the photon and the Compton electron given the angle of scatter [41]

$$E'_\gamma = \frac{E_\gamma}{1 + \frac{E_\gamma}{m_e c^2} (1 - \cos \theta)} T_e = E_\gamma \frac{\frac{E_\gamma}{m_e c^2} (1 - \cos \theta)}{1 + \frac{E_\gamma}{m_e c^2} (1 - \cos \theta)} \quad (2.5)$$

where E_γ and E'_γ are the photon energies before and after the compton scattering process mechanism.

Not all the energy of the original photon is transferred, leading to the occurrence of successive Compton scatterings until all the energy is deposited in the medium (or a scattered photon escapes the medium with a fraction of it). The maximum value of energy transfer occurs for a scattering angle of $\theta = 180$ degree (back scattering):

$$T_{emax} = E_\gamma \frac{\frac{E_\gamma}{m_e c^2} (1 - \cos \theta)}{1 + 2 \frac{E_\gamma}{m_e c^2}} \quad (2.6)$$

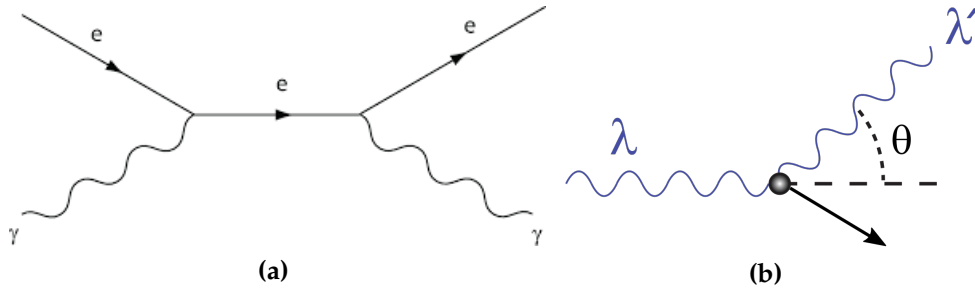


Figure 2.4.: (a) Tree level Feynman diagram of the Compton scattering process. (b) Sketch of the Compton scattering process (see text for detailed description).

The last aforementioned photon-matter interaction is the pair production mechanism, where the reverse of the e^+e^- annihilation process happens: a high energy photon may materialize into an e^+e^- pair, given it has a field to mediate the interaction, in this particular case in the Coulomb atomic electric field. The energy threshold for pair production, considering null the recoil energy of the nucleus, is given by:

$$h\nu_{min} = 2m_e c^2 = 1.22 \text{ MeV} \quad (2.7)$$

Right after the pair production mechanism takes place, the electron and positron thermalize and give origin to a annihilation processes, mostly with the medium, where the particles vanish and two 511 keV photons are emitted in opposite directions. As important as this mechanism is in energies above the MeV scale, in the range of the main γ backgrounds in XENON1T, its probability is negligible (further discussed in Section 2.3.3).

2.2. Gaseous detectors and light signals in noble gases

The main focus of experimental particle physics is to look for the presence and interaction properties of different particles, may they be already known or, as the case of WIMPs, unknown. This general goal can be tackled through many angles: collider physics at the LHC, astronomical and cosmological observations or direct particle detectors. In all of these methods, particle detectors, in many different types and setups, play a major role in the identification and characterization of particles. In the XENON experiments, the detector principle is the double-phase Time Projection Chambers (TPCs), explained in detail in the next section, Section 2.3.1.

2.2.1. Operation principle of gaseous detectors

The basic processes happening in most gaseous and liquid particle detectors are the same, as is their operation principle. A gaseous/liquid detector is composed (at least) by a target volume, electrodes inducing an electric field in the volume and a way to readout a signal, may it be charge-like or light-like. When an interaction happens inside the target volume, processes of excitation and ionization of the medium lead to a deposition of the incident particle energy within the detector, later collected as a signal. A charge-like signal may be read directly from the field-inducing electrodes

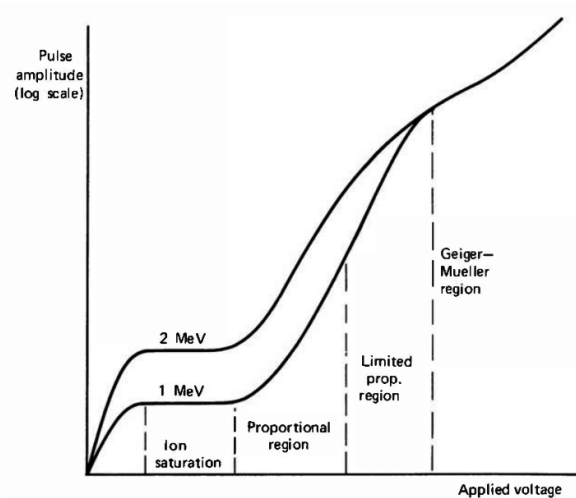


Figure 2.5.: Standard operating regions of gaseous/liquid detectors: recombination, ionization, proportionality, limited proportionality, Geiger-Müller and continuous discharge. For in depth description see text. Figure from [44]

or have a designated read-out electrode. On the other hand, a light signal must have specific equipment like photomultiplier tubes (PMT) or avalanche photomultipliers (APDs) to be collected and measured (converted into current in electronics).

The mode of operation of a gaseous detector is set by the $\frac{E}{p}$ fraction, tuned by the voltage of the electrodes. Six different regions can be individually described:

- Recombination region – given null or very low electric fields, resulting in low electron drift velocities, the electron-ion pairs formed by the deposition of energy tend to recombine before reaching the electrodes.
- Ionization region – in this region, the electric field is responsible for collecting the majority of ion-electron pairs in the electrodes, without any charge multiplication. The output signal can be used to determine the deposited energy but is usually too low to be measured with high precision.
- Proportional region – in this mode of operation, the electric field is high enough that the primary electrons gain energy between collisions to induce more ionizations in the medium, leading to an avalanche phenomenon with multiplication of charge. The gain in charge or gas amplification factor, defined as the ratio between primary ion-pairs formed and collected, is proportional to the voltage applied in the electrodes, allowing for better signal resolution and efficient energy deposition calculation.
- Limited proportionality region – No clean proportionality between charge gain and electrodes voltage is achieved due to distortion in the electric field by positive ions, making it less useful than the proportional region described above and usually avoided.
- Geiger Müller region – in this region, multiple avalanches are produced from a single event, originating a very high amplitude signal. Moreover, the multiplication effect spreads through the whole detector, only ending when the heavy positive ions cancel out the electric field of the electrodes. This mode only serves as a counting device as all kinds of interaction in the target volume saturate the detector.
- Continuous discharge region – in this region, the electric field inside the target volume is higher than the ionization potential of the medium, leading to spontaneous ionizations and continuous discharges. No standard experimental studies are done in this mode of operation.

2.2.2. From interaction to signal

When an interaction occurs in a rare gas target, the deposited energy T_0 is used in forming electron-ion pairs N_i , excited atoms N_{ex} and subexcitation electrons (free electrons with lower energy than the first excited level) [45]:

$$T_0 = N_i E_i + N_{ex} E_{ex} + N_i \bar{\epsilon} \quad (2.8)$$

where, besides the aforementioned quantities, E_i is the average energy expended on electron-ion pairs production, E_{ex} is the average energy expended on exciting atoms and $\bar{\epsilon}$ is the average kinetic energy of subexcitation electrons. From here, Platzman deduced the W value⁴ of rare gases to given as:

$$W = T_0/N_i = E_i + E_{ex} (N_{ex}/N_i) + \bar{\epsilon} \quad (2.9)$$

Except for very low energies, the W value of a given rare gas can be considered constant as it almost does not change with the type and energy of the interacting radiation [46]. The W values for Argon, Krypton and Xenon gases and liquid phases are shown in Table 2.1.

Table 2.1.: W values for liquid and gas Argon, Krypton and Xenon atoms. Values in eV, from [46], Table II.

Phase	Ar	Kr	Xe
Gas	26.4	24.2	22.0
Liquid	23.6	18.4	15.6

Excitation, scintillation and the S1 signal

The excited atoms resulting from a particle interaction within the target volume, N_{ex} in equation 2.8, usually release the absorbed energy through photon emission. This process is called scintillation or luminescence. In LXe the excited atoms do not directly

⁴The W value is defined as the average energy used to produce one electron-ion pair

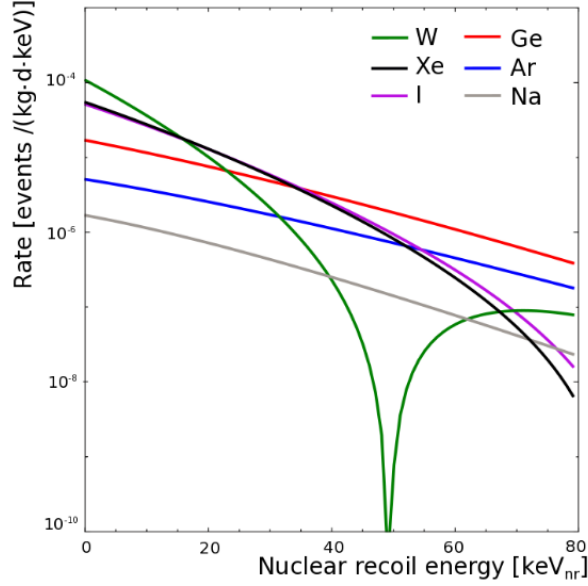


Figure 2.6.: Event rates from different target materials for a SI WIMP-nucleon interaction. Figure from [47]

return to their ground state but form excited dimers:



In the absence of an electric field, or if the field is not strong enough to collect all the ion-electron pairs, a fraction of them will undergo recombination, leading to more scintillation processes from Xenon dimers



These Xe_2^* dimers, when decaying to the ground state (2.11, 2.16), release a photon with wavelength of 178 nm, in the vacuum ultraviolet (VUV) region) [46]. The time signature of such decay has two components due to the single and triplet states of Xe_2^* . Studies on the incident particle can be conducted from the relation between these two

components through Pulse Shape Discrimination (PSD) analysis. Nonetheless, in the case of LXe, even though physically possible, the time separation between the two components – of a few nanoseconds - makes PSD a possible but very difficult task [48]. On the other hand, LAr singlet and triplet components have large time separations (5 and 1950 ns, respectively) making this methods very effective and efficient. For instance, this has been sucessfully accomplished for WIMP search by the Darkside50 experiment at LNGS [36].

The number of photons, n_γ , is in good agreement equal to the number of excited atoms. From all these scintillation photons, only a fraction contributes to the collected light signal, called $S1$. This fraction is mainly controlled by the detector's geometry and the presence of impurities such as oxygen or water molecules whose absorption spectrum overlaps the VUV region. To maximize light collection, detectors like XENON100, LUX or XENON1T use Polytetrafluoroethylene (PTFE) sheets to cover the inner surface of the TPC, reaching as much as a reflectivity of $\geq 97\%$ [49]. Photons that travel larges distances and get multiple times reflected in the walls, are the ones affected by the latter problem, for which an ultrapure medium must be achieved. The fraction of scintillation photons that is collected in the PMT array is called *light collection efficiency* and proves to be highly position dependent. Moreover, when a scintillation photon reaches a PMT it is not granted that a $S1$ signal is measured as not all photons are converted into photoelectrons and not all photoelectrons get accelerated inside the PMT. The quantum efficiency (QE) of these processes is different for each PMT. For the XENON1T detector an average QE of 34.5% and 90% efficiency on producing a signal in the PMT from the photoelectron is achieved [50].

Ionization, recombination and electron drift

A considerable amount of energy deposited by a particle on an event is consumed on forming electron-ion pairs. In the absence of an applied electric field all the ion pairs will recombine into excited atoms and proceed to scintillate (equation 2.16). When an electric field is applied, some of the electrons get drifted through the medium away from the positive ions (which also get drifted in the opposite direction, though much slower) and, therefore, the recombination probability, $r \in [0, 1]$, drops. The number of electrons extracted from the interaction by the electric field is controlled by the

recombination probability through:

$$N_q = (1 - r)N_i \quad (2.17)$$

The fraction of extracted electron is given by $(1 - r)$ and is highly dependent on the ionization track and energy. As mentioned in Section 2.1, lighter particles like gammas and beta rays, interact mainly through multiple site scatters, spread their tracks and featuring small recombination rates. On the other hand, heavy particles such as alphas and neutrons deposit most of their energy in a small region, greatly increasing the recombination probability. Recalling that recombined electron-ion pairs increase the number of scintillating excited atoms, a distinct difference between electronic and nuclear recoils arises. Quantitatively, the ratio between the initially formed excited atoms and the electron-ion pairs, N_{ex}/N_i , yield 0.06 for electronic recoils (strong anti-correlation between charge and light signals) and 1.09 for nuclear recoils (strong correlation between charge and light signals) [51].

Studies conducted by Policarpo [52], later by Anderson and Suzuki, propose increasing the ionization yield by adding dopant molecules with high photosensitivity. As their ionization potential is lower than the energy of scintillation photons, additional electron-ion pairs will be created. Despite the major advantages in charge signal detection, this process is not used in double-phase light based TPCs as for the most part it prevents a measurable or linear S1 response.

In order for the primary electron cloud to drift throughout the detector volume without loss of charge, the medium must be ultra pure to prevent electronegative impurities such as oxygen. The purity can be quantitatively ranked by the *electron lifetime*, and albeit an high field is needed to prevent recombination, the excitation potential of the medium must not be reached to prevent electroluminescent (or secondary ionization) in the drift region.

Secondary scintillation and the S2 signal

In double-phase detectors, further discussed in Section 2.3.1, a second light signal, the S2, comes from the electrons that escaped recombination, drifted through the liquid phase and got extracted into the gas phase. The gas phase serves as a proportional scintillation region, inducing multiple scintillation photon emissions until they are

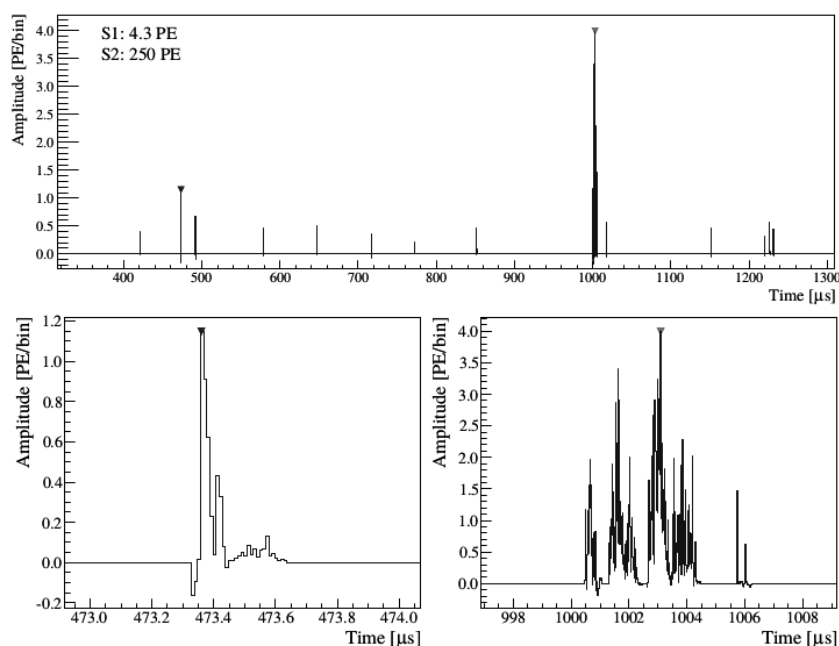


Figure 2.7.: Example waveform from the XENON1T detector for a NR event during a $^{241}\text{AmBe}$ calibration run. The upper part shows the complete time frame of the event, with both the S1 and S2 peaks, shown in detail at the bottom panels. The drift time of $529.7\ \mu\text{s}$ corresponds to a depth of $Z = -75.9\ \text{cm}$. Figure from [50]

collected. Given large enough extraction fields ($10\text{kV}/\text{cm}$, $\frac{E}{p} \approx 5\text{kV}/\text{cm}/\text{atm}$ [53]), the extraction efficiency is close to 100%. Due to the diffusion of the electron cloud within the liquid, the S2 signal is more wide than the corresponding S1 and spreads over a longer time period. The number of photoelectrons product of proportional scintillation created from the extracted electrons, n_e , directly relates to the S2 signal through the S2 gain factor, g_{S2} :

$$S2 = g_{S2} \cdot n_e \quad (2.18)$$

Energy scale

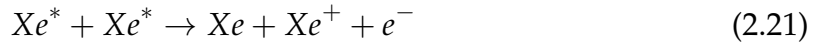
Finally, taking all the above processes and considerations, one can aim to estimate the energy deposited by a particle in the target volume using the measured S1 and S2 signals.

As mentioned in Section 2.2.2, for beta and gamma rays, the S1 and S2 signals are mostly uncorrelated and the deposited energy is well fitted by:

$$E_{ER} = W (n_\gamma + n_e) \quad (2.19)$$

$$= W \left(\frac{S1}{g_1} + \frac{S2}{g_2} \right) \quad (2.20)$$

where W is the average energy needed to produce a quantum, determined to be 13.7 eV/quantum experimentally [54]. The photon detection efficiency, g_{S1} , and the charge amplification factor, g_{S2} , are specific for each experimental setup and must be determined accordingly. Note that equation 2.20 only holds for light charged particles and does not model alpha particles electronic recoils. For nuclear recoils more considerations must be taken. The scintillation yield⁵ is much smaller than for electronic recoils due to nuclear quenching and the increased probability of electron emission in dense tracks by the process of collision between two excitons [55]:



To take these effects into consideration, an effective scintillation function, \mathcal{L}_{eff} is introduced:

$$\mathcal{L}_{eff} = \frac{L_{NR}}{L_{ER,^{57}Co}} \quad (2.22)$$

\mathcal{L}_{eff} is defined as the ratio between the scintillation yield of nuclear recoils and the scintillation yield of electronic recoils from the full absorption peak of the 122 keV gamma line from ^{57}Co

The nuclear recoil energy, E_{NR} , relates to the S1 signal by [56]:

$$E_{NR} = \frac{S1}{\mathcal{L}_{eff} \cdot L_{ER,^{57}Co}} \cdot \frac{S_{ER}}{S_{NR}} \quad (2.23)$$

where S_{ER} and S_{NR} account for the field dependence of electronic and nuclear recoils and \mathcal{L}_{eff} , which is energy dependent, is experimentally determined [56,57]. ON the other hand, the S2 measured signal can be used to determine the nuclear recoil energy

⁵Scintillation yield is commonly defined as the number of free photons per unit energy

without the need for any reference point. The relation is given by [58]:

$$E_{NR} = \frac{S2}{Y \cdot Q_y} \quad (2.24)$$

where Y is the gain of the secondary scintillation from single electrons and Q_y is the charge yield of nuclear recoils. Note that Q_y is greatly energy dependent and is usually derived by matching simulated data to calibration data.

The latest results by XENON1T detector alongside older results for light and charge yield on electronic and nuclear recoils are shown in Figure 2.8.

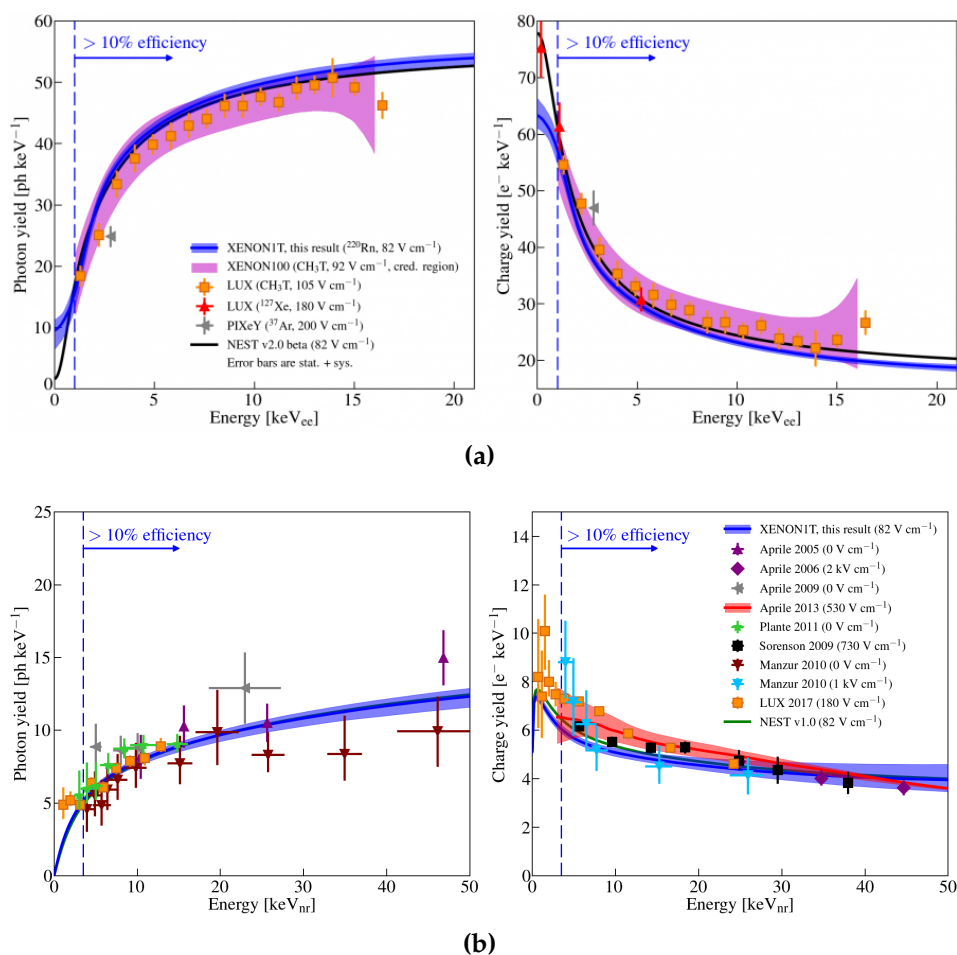


Figure 2.8.: (a) Electronic recoil photon and charge yields from 0-21 keV_{ee}. (b) Nuclear recoil photon and charge yields from 0-80 keV_{nr}.⁶ [59]

⁶The unit *keVnr* relates to the energy deposited by a nuclear recoil. Direct energy calibration is not often possible and therefore the unit *keVee*, or electron equivalent, is used: $E[keVee] = E[keVnr] \times \mathcal{L}_{eff}$

2.3. The XENON1T detector

The XENON1T detector is a two-phase Xenon TPC particle detector located in Hall B of *LNGS*, in Italy, and is one of the few TPC detectors worldwide with tonne-scale target volume. XENON1T is the third detector in the XENON family of detectors, following the work done in XENON10 [60] and XENON100 [61] with 15 (5.4) and 62 (34) kg target (fiducial) mass. In this section, an outlook of the subsystems of the detector will be stated, followed by a study on its major backgrounds and calibration techniques. Apart from where specifically stated, the sources of information for each topic are *The XENON1T dark matter experiment* paper [50] and my own experience, collected over more than a month monitoring the detector on site.

2.3.1. The Double-Phase TPC Principle

All of the XENON detectors are, to this date, double-phase time projection chambers filled with xenon in liquid and gas form. This kind of apparatus, the target medium is the liquid phase, where, upon interaction by a particle, the energy transfer is split between scintillation, ionization and quenching (heat).

Given either an electronic or nuclear recoil, there will be production of scintillation photons and ionization electrons: an excited xenon atom merges with another xenon atom forming a diatomic excited molecule, which then de-excites into two xenon atoms and emits a 178 nm scintillation photon. As the photon is a product of the excimer state, it is not absorbed by the xenon atoms and can, therefore, be detected by the photomultiplier (PMT) arrays, giving origin to a primary scintillation signal or S_1 . On the other hand, electron-ion pairs split due to an existing vertical electric field, E_{drift} , which is also responsible for the drifting of the electron cloud up to the grounded gate and the positive ions to the cathode. There are two sets of PMT arrays, located on the bottom of the TPC, below the cathode, submerged in liquid xenon and on the top of the TPC, above the anode, in the gas phase. A few millimeters beneath the gas-liquid interface there is a grounded gate, separating the drift region from the extraction region.

Upon reaching the gate, the electrons are extracted from the liquid phase to the gas phase due to a much greater applied field, applied between the gate and the anode, $E_{extraction}$. As a result of this second field, a process of proportional scintillation is

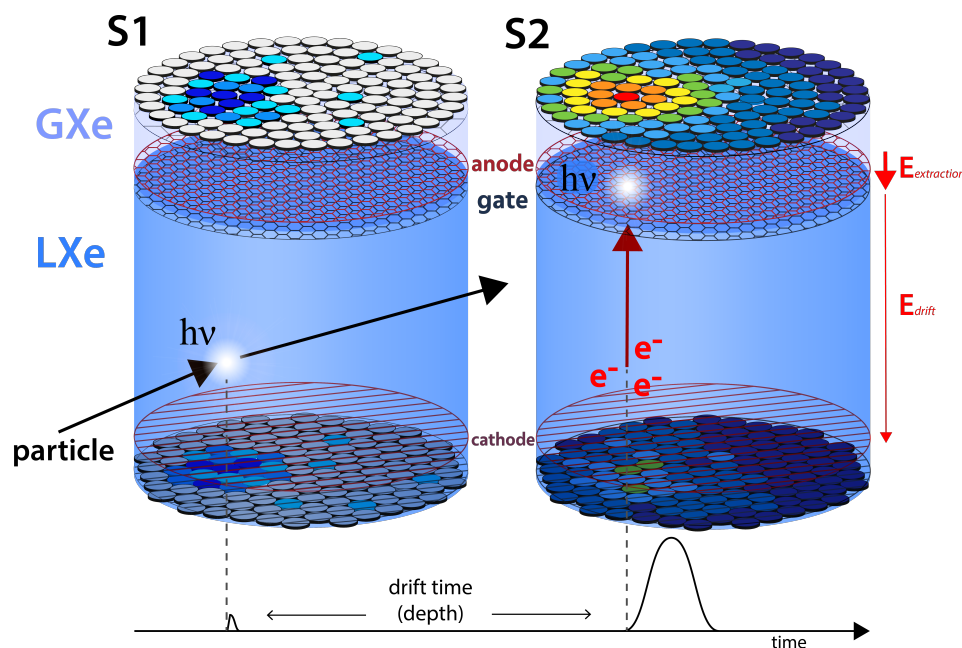


Figure 2.9.: Dual-Phase TPC working principle. A particle hits the target liquid xenon creating a scintillation signal (S1) detected in top and bottom PMT arrays. The interaction also produces electron-ion pairs that drift into the gate and cathode, respectively, given the presence of E_{drift} . The electrons are extracted from the liquid phase by a $E_{extraction}$ and proportionally scintillate, giving origin to the S2 signal, again detected by the top and bottom PMT arrays. See text for more details.

induced, giving origin to the second scintillation signal, charge signal or S2. For a strong enough field (10kV/cm [53]), the charge to light conversion is almost 100%.

In the end, two distinct signals are detected in both top and bottom array of PMT. As scintillation light is almost simultaneously produced and detected, the time difference between the S1 and S2 signals is mainly due to the drift time of the electron cloud through the TPC. Given the electron drift velocity, v_e , which directly depends on the drift field, the Z coordinate of the event can be calculated. This drift velocity is the focus of detailed studies, given its major importance to correctly reconstruct events inside the TPC.

$$Z = v_e \Delta t \quad (2.25)$$

Moreover, the hit pattern made in the PMT arrays can be used to infer the X and Y coordinates of the event, providing a full 3D reconstruction of the event.

A main advantage of this type of detectors is tagging events for their type of interaction. Since the light and charge yields of ER and NR are different, the light

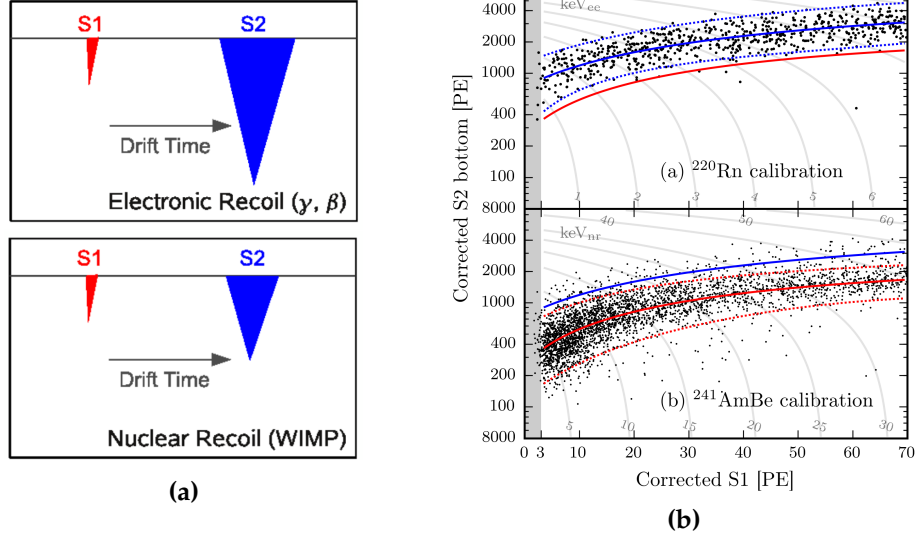


Figure 2.10.: (a) Principle of S2 over S1 discrimination. (b) ER and NR bands in $cS2$ over $cS1$ versus $cS1$ parameter space. Figure from [62].

signals, especially the S2 signals, are different, as well: an ER event is expected to produce a much larger and wider S2 from a similar S1 than an NR event. A plot of the S2 over S1 ratio versus S1 is usually very representative in this regard (see Figure 2.10b). The light signals collected in the PMT arrays are processed and corrected for the charge loss that might have happened during the drift of the electron cloud with information from the electron lifetime, giving origin to the *corrected* variable $cS2$, and for the area of the main interaction with the reconstructed event position and field electric effects, giving origin to the corrected variable $cS1$. PMTs in the top array have large differences in illumination, gaining sensitivity for position reconstruction. However, the hit pattern of the bottom PMT array is spread across the overall area, reducing inaccuracy when calculating the S2 size. This feature is taken into account for ER/NR interaction discrimination and energy spectrum studies where $cS2_{\text{bottom}}$, the corrected S2 signal measured by the bottom PMT array, is preferred over the $cS2$ parameter.

2.3.2. Detector subsystems and TPC

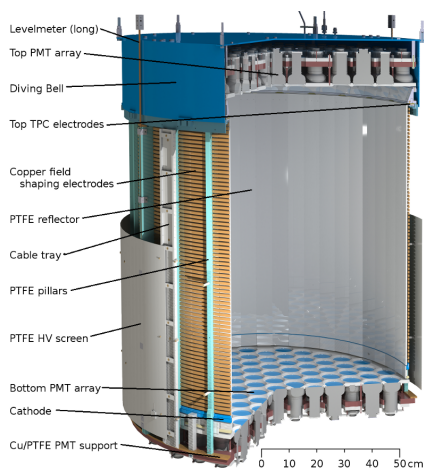
The XENON1T detector is a complex set of systems working and communicating with each other. The dual-phase TPC is placed in the center of a 10.2 metre high, 9.6 metre diameter water tank and all its subsystems in a three-floor building next to it.

The XENON1T detector can be divided into subsystems:

- TPC
- Cryogenics
- Purification
- Water shield and muon veto

TPC

The cylindrical two-phase TPC is the heart of the experiment (Figure 2.9, Figure 2.11). It has a length of 97cm and a diameter of 96 cm holding up to 2 t of LXe. Events happening inside the LXe, as described in the last section, originate a measurable S1 and S2 signal. These light signals are recorded by a total of 248 Hamamatsu R11410-21 [63] PMTs of 76.2 mm diameter, radially distributed to increase radial position reconstruction performance on the top array and packed on an hexagonal pattern to maximize light collection on the bottom array. Before reaching the PMT window, some scintillation photons will be reflected in the side walls of the TPC, within an efficiency of 97%, in 24 tightly interlocking PTFE panels.



(a)



(b)

Figure 2.11.: (a) Sketch of the XENON1T TPC, at scale. Figure from [50]. (b) Picture of the XENON1T TPC in the cleanroom, before assembly in the water tank.

Another key aspect of ensuring a measurable and stable S2 signal response is the electric field inside the TPC. The circular stainless steel anode, biased at +4 kV, sits above the top PMT array, etched in a hexagonal pattern to optimize optical transparency. Dividing the drift and extraction regions, still submerged in LXe, there is a gate mesh connected to the ground voltage, setting the end of around 1 metre of drift field. Below the bottom PMT array stands the negatively biased cathode responsible for setting the drift electric field. The cathode, unlike the anode and gate, is made of parallel wires. Outside of the PTFE panels, surrounding the TPC, there are 74 field shaping rings to ensure field uniformity throughout the entire drift field. The detector electrodes, in particular the latter, will be further discussed in Chapter 4, mostly through electric field electrostatic simulations of the whole TPC.

Cryogenics and purification

The TPC is enclosed in a 1.96 m high and 1.1 m inner diameter stainless-steel cryostat in the center of the water tank. Two pipes connect the inner part of the cryostat with the exterior, one for xenon circulation, PMT cable and slow control sensors and another for the high-voltage feedthrough to the cathode. Three rods attached to the support frame inside the water tank hold the cryostat suspended and are used to precisely lower and tilt the TPC in respect to the liquid level. All the materials used were especially selected for very low radioactivity in order to reduce background contamination in the target volume.

To keep Xenon at liquid temperature, a complex cryogenic system cools down the Xenon gas using Pulse Tube Refrigerators (PTR) [50] outside the cryostat to be again fed to the liquid phase. This is done in line with the storage and purification facilities. The first of these, *ReStoX*, enables the possibility for a fast recovery of Xenon in case of emergency instead of just releasing the noble gas into the laboratory atmosphere, as well as recovering the noble gas for use at XENONnT phase, where the cryostat needs to be opened. As for the latter, in order to achieve high order of purity, a constant flow of LXe is taken out of the bottom of the TPC to go through two independent and redundant purification loops. As an independent system, a Krypton distillation column sits next to *ReStoX*, used to reduce the amount of Kr in commercial Xenon as its natural isotope ^{85}Kr is a major contamination source from its beta decays (see Section 2.3.3 for a more detailed outlook).

Water tank and Muon-veto

Another major improvement from past experiments implemented in XENON1T is the large passive water shield and the active Muon Veto within. The passive deionized water shield significantly decreases the amount of γ rays that reach the TPC, as well as radiogenic neutrons from the walls of the laboratory, enclosed in a tank of 9.6 m diameter and 10.2 m height. The tank has a total of 84 PMT of 20.3 cm in diameter working as a Cherenkov muon veto. An effective muon interaction identification is of great importance not just because of the muon as a background component but specially due to muon-induced neutrons, as radiogenic neutrons and gammas are stopped by the water. As will be later described, neutrons are of major concern in dark matter searches as they, like WIMPs, interact within the target volume through nuclear recoils.

2.3.3. Backgrounds

In a rare event search experiment, a complete and thorough study of backgrounds is a key ingredient for better sensitivity and discovery potential. As explained before in Section 2.3.1, electronic recoils from ionizing particles and nuclear recoils from neutral particles can be distinguished using the S2/S1 ratio. Nonetheless, an overlap region occurs, where statistical leakage is prone to misidentify events. In the worst case scenario an ER event might even mimic a WIMP signal. Therefore, not only efforts to reduce NR contamination must be taken, but studies of the ER backgrounds and their behavior are also vital. A summary of the main sources contributing to the background of XENON1T is shown in Table 2.2, from [50].

Electronic recoils background

Within the total ER background to take note of, two sets are easily distinguishable: extrinsic and intrinsic. Extrinsic backgrounds cover all radioactivity events from the detector materials and surroundings, for instance, the walls of the cavern and muon induced events, while intrinsic backgrounds are due to radioactive sources present in the active volume of the detector, such as ^{222}Rn and ^{85}Kr . The first mentioned type is greatly improved by the fiducialization of the target volume, given the high stopping

Table 2.2.: Summary for the background sources and rates in XENON1T, considering a fiducial volume of 1 t, taken from the Monte Carlo simulation study [64].

Background Source	Type	Rate [(t × y) ⁻¹]	Mitigation Approach
²²² Rn	ER	620	material selected for low Rn-emanation; ER rejection
solar pp- and ⁷ Be- neutrinos	ER	36	ER rejection
⁸⁵ Kr	ER	31	cryogenic distillation; ER rejection
material radioactivity	ER	30	material selected for low Rn-emanation; ER and multiple scatter rejection; fiducialization
2ν2β of ¹³⁶ Xe	ER	9	ER rejection
CNNS	NR	0.6	-
Radiogenic neutrons	NR	0.55	material selection; multiple scatter rejection; fiducialization
Muon-induced neutrons	NR	<0.01	active Cherenkov veto; multiple scatter rejection; fiducialization

power of xenon atoms. A fiducial volume refers to a fraction of the overall target volume in the middle of the latter, where the background (mainly ER) is suppressed.

²²²Rn is, up to this date, the main background of the XENON1T experiment, as seen in Table 2.2 and Figure 2.13b. ²²²Rn is produced in the detector materials as part of the ²³⁸U chain. Due to its half-life of 3.8 days, it ends spreading throughout all of the target volume homogeneously, excluding fiducialization as a viable mitigation approach. Within the ²²²Rn decay chain (Figure 2.12a), the most dangerous contribution comes from the ²¹⁴Pb → ²¹⁴Bi beta channel with an end-point energy of 1019 keV. This is particularly worrying to a dark matter experiment because it stands as an intrinsic non-negligible background. The other β emitter in the chain, ²¹⁴Bi, has its effect removed by correlating the decay signal with the alpha emission from its daughter decay, ²¹⁴Po → ²¹⁰Pb, easily tagged in the detector.

On the other hand, ⁸⁵Kr appears naturally in commercial Xenon at around 1ppm to 10 ppb, undergoing a beta decay with a half-life of 10.76 years and an end point energy of 687 keV. As a prime example of intrinsic backgrounds, the amount of Krypton can only be treated by purifying the active Xenon, aiming to remove the Krypton

concentration. In XENON1T, a distillation column working on-line before and during science runs was adopted to reduce the amount up to (0.36 ± 0.06) ppt, registered after the first science run. Other known contamination of natural Xenon is the isotope ^{136}Xe , with an abundance of 8.9%, which decays through a two-neutrino double beta process with a Q-value of 2458 keV. This background, due to its intrinsic nature becomes much more relevant as the target volume increases. For XENON1T, however, ^{222}Rn still is the dominant background (see Figure 2.13b).

Nuclear recoils background

Neutral particles such as neutrons and neutrinos can produce nuclear recoil events via elastic scattering off xenon nuclei, producing interactions indistinguishable from a WIMP-nucleon interaction. Therefore, this dangerous background must be greatly minimized and thoroughly characterized. Radiogenic neutrons in the MeV range are present in the detector through spontaneous fission of isotopes of the primordial decay chains of ^{238}U , ^{235}U and ^{232}Th and (α, n) reactions in the materials used. These are mostly reduced when carefully selecting the detector materials and through multiple scatter identification - due to the low interaction rate of WIMPs, it is expected a single scatter signature from these particles, while for neutrons a major part of the energy deposition inside the target volume is done over multiple scattering events. Additional

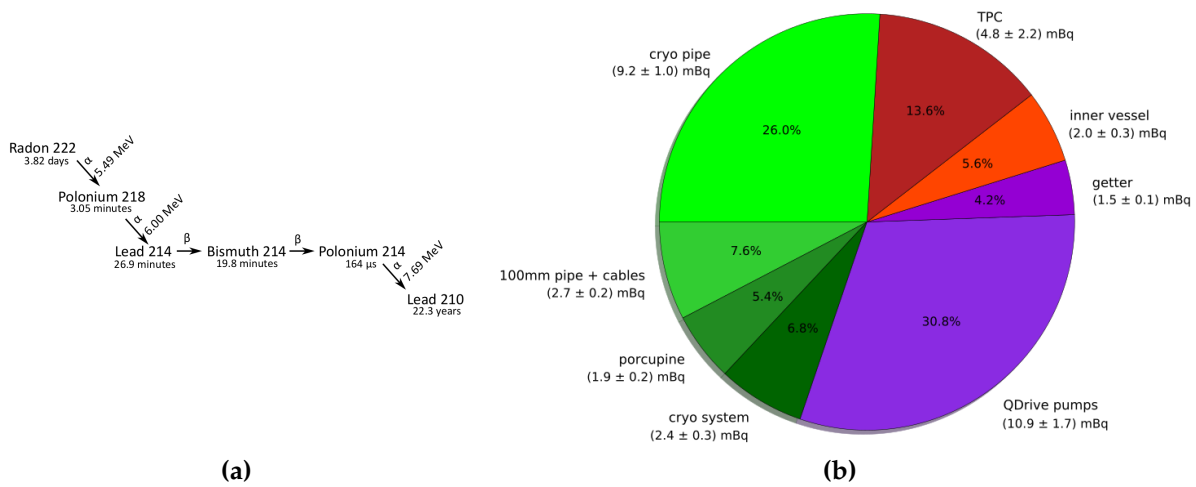


Figure 2.12.: (a) Decay chain of ^{222}Rn until the long lived daughter ^{210}Pb . (b) Radon emanation budget from the different components of the XENON1T experiment; Purple correspond to the purification system, red to the TPC and cryostat and green to cryogenics and pipes [65].

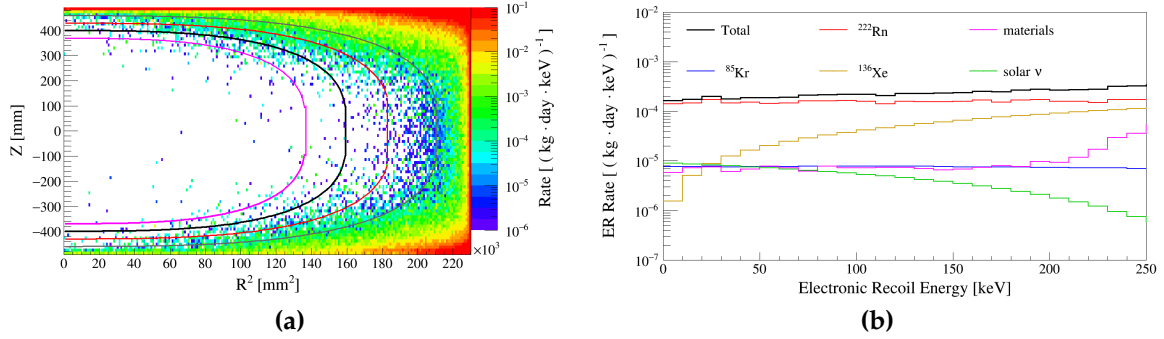


Figure 2.13.: (a) Spatial distribution of the ER background events from the detector materials in the (1, 12) keV energy range. The colored lines represent different fiducial volumes of 800, 1000, 1250 and 1530 kg, respectively. White regions indicate a background rate smaller than $10^{-6} \text{ kg}^{-1} \cdot \text{d}^{-1} \cdot \text{eV}^{-1}$. (b) Low energy spectrum of the total ER background rate in 1 tonne fiducial volume. Figures from [64]

neutrons are introduced by muon interactions with the rock along their path, these being identified by the active Cherenkov veto with a very high efficiency [50](see Section 2.3.2). Neutrinos produced in the Sun, diffuse supernova and in the atmosphere also contribute to the NR backgrounds through coherent neutrino-nucleus scattering (CNNS) [64].

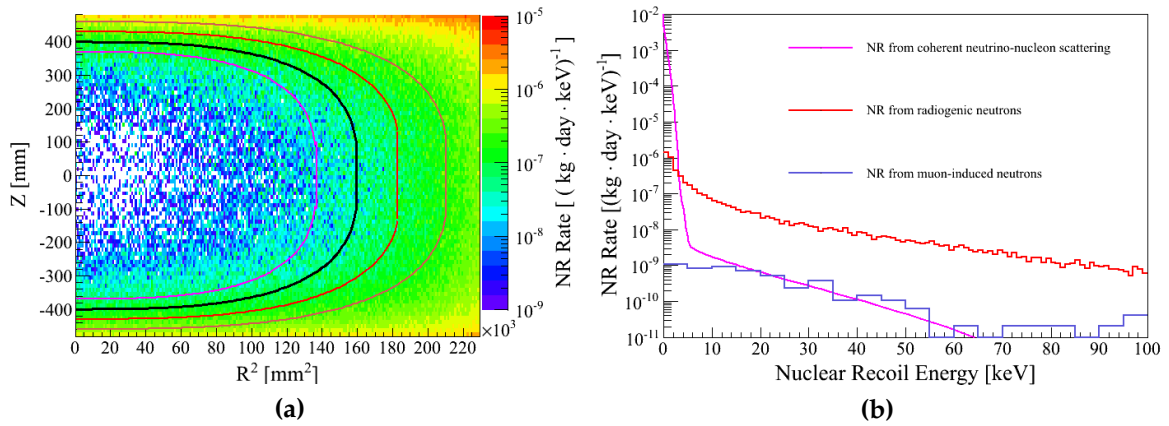


Figure 2.14.: (a) Spatial distribution of the NR background events from the detector materials in the (4, 50) keV energy range. The colored lines represent different fiducial volumes of 800, 1000, 1250 and 1530 kg, respectively. White regions indicate a background rate smaller than $10^{-9} \text{ kg}^{-1} \cdot \text{d}^{-1} \cdot \text{eV}^{-1}$. (b) Low energy spectrum of NR backgrounds rate in 1 tonne fiducial volume. Figures from [64]

Chapter 3.

Simulation and analysis of nuclear recoil calibration with a neutron generator in the XENON1T detector

“To achieve great things, two things are needed: a plan and not quite enough time.”

— Leonard Bernstein, 1918–1990

Calibrations are an important step in any experiment focusing on discriminating events. As a complex detector with great physics search potential, XENON1T needs to be deeply studied in respect to energy and position response and discrimination. Focusing on dark matter search, one needs to accurately distinguish between a gamma background electronic recoil, neutron background nuclear recoil or potential wimp interaction. With this task in mind, various campaigns to acquire calibration data were conducted before, during and after science data runs. In this chapter, the topic of nuclear recoil band calibration is addressed, focusing on calibration data from a Neutron Generator (NG). First, in Section 3.1 an introduction on the XENON1T NR calibrations and neutron generator runs is presented. Later on, in Section 3.2, the efforts done in simulating a neutron generator calibration campaign are discussed, from the XENON1T *Geant4* model up to the simulation outputs and results. Section 3.3 is divided in three parts: details on the NG data acquired during SR1 and a loose explanation of the analysis cuts used (Section 3.3.1), followed by a in-depth study of the matching between MC and real data through the acceptance of the different

cuts employed (Section 3.3.2) and, as the last topic covered, the post-SR1 NG data is studied through event selection and used to fit the NR band, as well as compare it to previous results.

3.1. Nuclear Recoil band calibrations in XENON1T

The XENON1T science-search campaign is, up to now, divided into two major runs: Science-Run 0 (SR0), from November 22nd 2016, to January 18th 2017, when a 5.7 magnitude earthquake interrupted detector operations, and Science-Run 1 (SR1) from February 2nd 2017 to February 8th 2018, resulting in 32.1 days and 246.7 days of live blinded data, respectively. Numerous calibration campaigns with internal and external radioactive sources were employed during and between science-runs: to monitor major detector parameters $^{83\text{m}}\text{Kr}$ data was collected every 2.5 weeks; 17.1 days of data with an internal ^{220}Rn source for low-energy ER calibration; 30.0 days of data with an $^{241}\text{AmBe}$ source and 1.9 days of data with a D-D neutron generator for NR calibration [38].

These calibrations focus on calibrating the detector for WIMP-like interaction, which are expected to induce low-energy NR events, much alike neutron NR events.

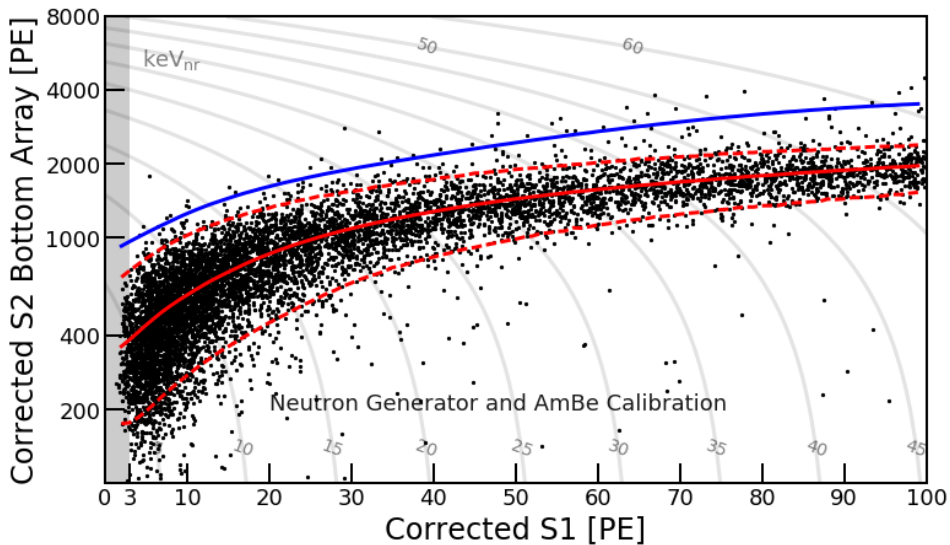


Figure 3.1.: Events of SR0 and SR1 used for NR calibration, from AmBe and NG data taken during SR1. The NR band edges and median are shown in solid red and the ER median in solid blue.

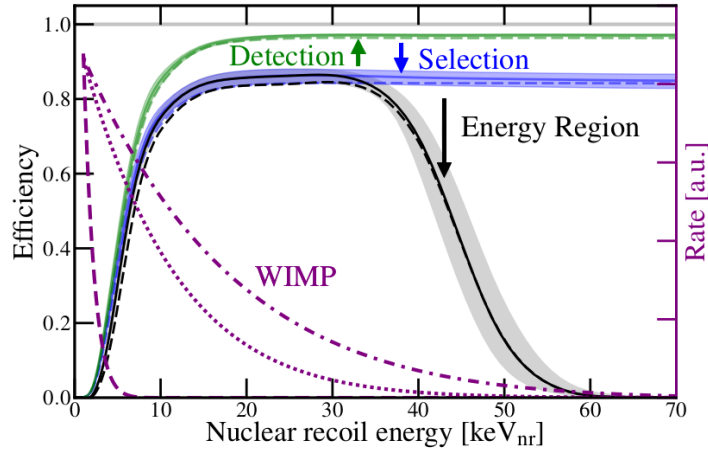


Figure 3.2.: Best-fit total efficiencies (black) for SR0 (dashed) and SR1 (solid) as a function of true NR energy (keV_{nr}). The efficiency of S1 detection and of S1 detection and selection are shown in green and blue, respectively. For reference, the expected spectral shapes of 10 GeV/c2 (dashed), 50 GeV/c2 (dotted), and 200 GeV/c2 (dashed dotted) WIMPs are overlaid. Figure from [38]

The detector efficiency is computed with a Monte Carlo code that realistically reproduces the shapes of S1s and S2s, taking into account interaction physics, light propagation and detector electronics. During analysis, an open-source developed processor, PAX, reconstructs the events in the detector and selection criteria on S1-S2 matching are used to reject possible multiple-scatters or spurious events. The computed efficiency versus NR energy for SR0 and SR1 combined is shown in Figure 3.2.

3.1.1. Use of a neutron generator in XENON1T

Using a neutron generator is a convenient way to acquire a large amount of NR calibration data. Neutron generators are commercially available, widely used in science and engineering, with the benefit of low long term contamination of the overall detector and almost no safety concerns when turned off, opposite to radiogenic neutron sources. A flux of 10^6 n/s to 10^{10} n/s range can be achieved with most neutron generator setups.

The NG used to calibrate XENON1T NR response was a model 35-DD-W-S deuterium-deuterium plasma fusion neutron generator manufactured by NSD/Gradel-Fusion

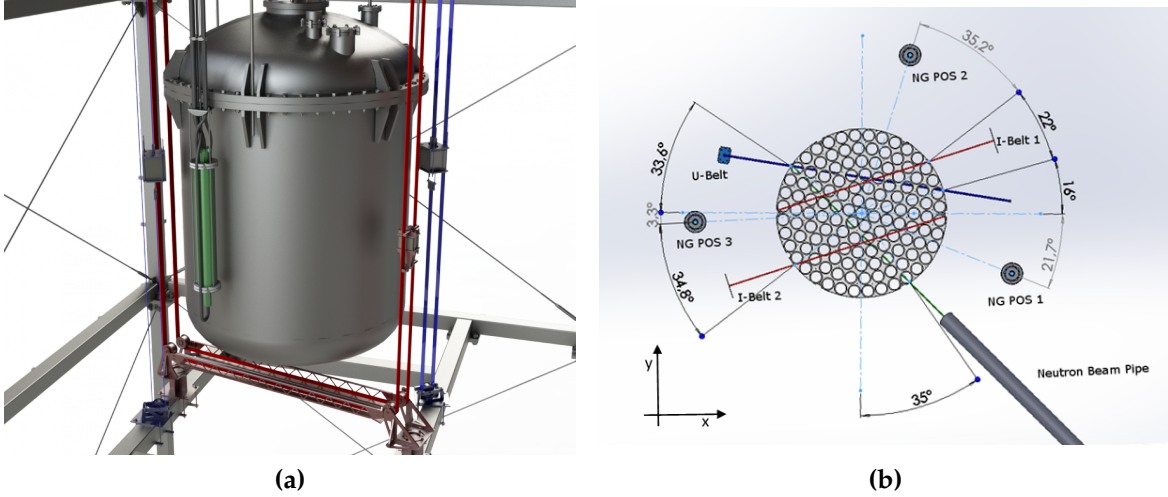
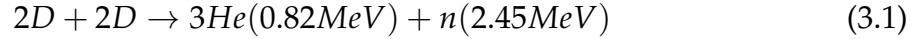


Figure 3.3.: (a) CAD drawing of the neutron generator in operation condition, inside the water tank. (b) Sketch of the three possible position for NG operation around the cryostat

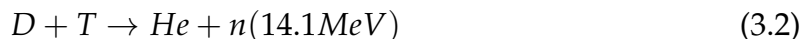
[50], which operates based on the fusion of deuterium:



The 2.45 MeV neutron flux can be tuned by setting the generator voltage and current through a dedicated computer and slow control software during operation. Even though this model can achieve a flux of 10^7 n/s, for this particular application, it was modified to achieve a flux as low as 10 n/s, isotropically, in order to prevent pile up of events [66]. The 94 cm length and 13.8 cm diameter cylindrical shape NG can be placed inside the water tank on three different positions around the cryostat, aiming for a uniform illumination of the whole TPC. The working principle of such NG is based on inertial electrostatic confinement (IEC), using plasma fusion of ions in the presence of a high voltage potential. The fusion chamber of the NG is filled with deuterium gas that when in low pressure can be ignited into a plasma state by glow discharge (Paschen's law¹). Then, the deuterium gas inside the chamber is ionized and the resulting ions accelerate toward the cathode. Confined in a field cage with set voltage, when the conditions are proper, fusion occurs through the aforementioned reaction (equation 3.1) and mono-energetic 2.45 MeV neutrons are emitted. A secondary reaction involving deuterium and tritium also takes place and is

¹Paschen's law calculates the voltage required to start a discharge between two electrodes in a gas as function of pressure and distance between electrodes.

responsible for the emission of some 14.1 MeV neutrons:



3.2. Simulation of a neutron generator run

3.2.1. The XENON1T Geant4 model

An accurate Monte Carlo model of the XENON1T detector was developed by the collaboration using the GEANT4 toolkit [67] for broad use. This model was used to simulate many outputs needed for calibration, position-reconstruction of events, photon collection efficiency, spacial dependencies and background modeling, alongside testing different geometries and materials of components in the design phase. The final model geometry was built according to the CAD construction drawings, as seen in Figure 3.4, and features every major component and known background source in the detector.

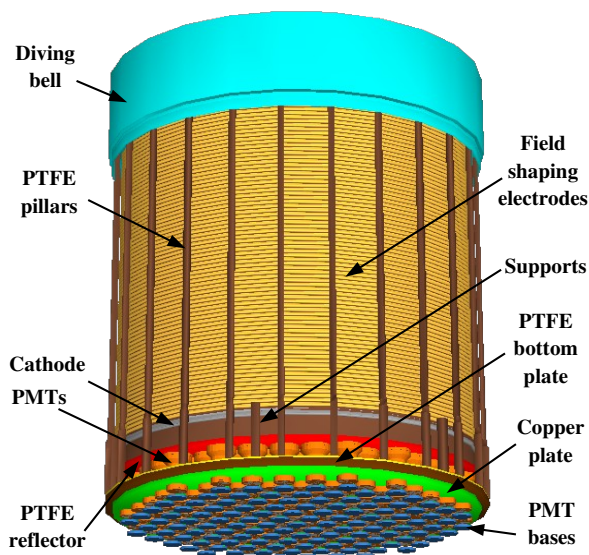


Figure 3.4.: Rendering of the external part of the TPC modelled in GEANT4. From top to bottom, the diving bell (cyan), PTFE pillars and support parts (brown), field shaping electrodes (yellow), PTFE reflector among the PMTs (red), PMTs in the bottom array (orange), copper plate (green), PMT bases (blue). Picture from [64].

As in the real detector, a vacuum-insulated double-wall cryostat made of 5 mm low radioactivity stainless steel (SS), internally covered by 24 interlocking PTFE panels with a radius of 48 cm, that shrink about 1.5% when cooled to the detector operation temperature. At the bottom of the TPC, immersed in LXe, a compact hexagonal structure holds 121 PMTs and at the top of the TPC, in the gas phase, 127 more PMTs, placed in concentric rings to improve the radial position reconstruction, observe the target volume. Every major component from the PMT structure is reproduced in the G4 model: a cobalt-free body made of Kovar, a quartz window and a ceramic stem. The model does not include the dynodes and the getter inside the PMT. The electrodes, made out of SS, divide the different electric regions of the detector. The model also features the 74 field shaping rings made of oxygen-free high thermal conductivity (OFHC) copper surrounding the PTFE panels, responsible for keeping the electric field uniformity inside the target volume.

The implementation of the neutron generator is done as a separate class alongside the main `Xenon1tDetectorConstruction` file, following the technical drawings provided by NSD/Gradel-Fusion [66,68]. The Physics List for NG simulations is the same used for every MC study, using version 9.5-patch01 of the G4 toolkit with `G4RadioactiveDecay` processes for α , β^+ and β^- decay and electron capture and `HighPrecision` for low energy neutrons (< 20 MeV), which accurately describes cross-sections down to thermal energies. Furthermore, the emission spectrum of the NG was characterized in [66], reaching the below stated conclusions:

- The energy spectrum is **not** strictly monoenergetic, containing two major peaks, at 2.22 MeV and 2.72 MeV, as well a measurable contamination of 14.1 MeV neutrons from D-T fusion (Figure 3.5);
- The neutron flux can be controlled during operation, given the characterized dependence from applied voltage and current;
- the angular distribution of neutron flux is approximately **isotropic**;

Following this extensive characterization and the developed MC model, the behavior of the NG can be predicted and became an important tool as a NR calibration source.

A complete description of the Monte Carlo model, physics list and important applications such as background modeling (see Figure 2.13b and Figure 2.14b), Light Collection Efficiency (LCE) maps and conversion from energy deposition to simulated

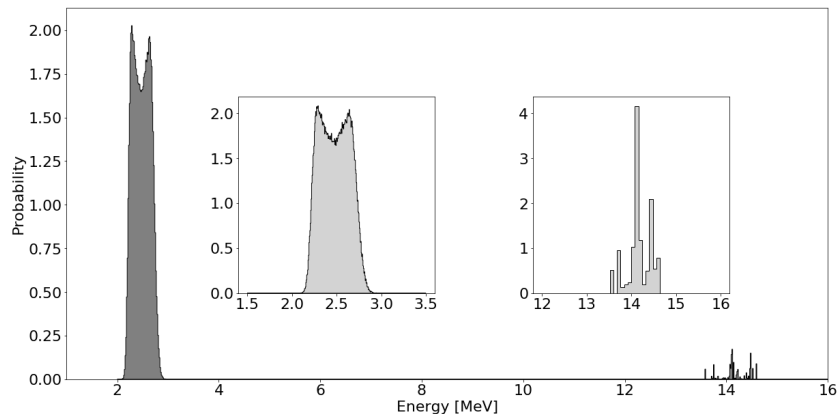


Figure 3.5.: Simulated energy spectrum of the Neutron Generator, used as input for primary energy spectrum in the MC simulations [69].

S1 and S2 signals, can be found in reference [64] and the references within, as it extends beyond the scope of this work.

3.2.2. Simulation results

Using the G4 model described in the last section, various simulations of a neutron generator calibration campaign were computed, covering all three possible positions of the NG in the water tank. These simulations were done as part of the Monte Carlo productions and analysis leading up to NR band calibrations and classification of background events for SR1 results paper, now published by PRL [38]. These simulations were done using resources provided by the Open Science Grid [70] and the University of Chicago Research Computing Center. The efforts put into analysis of simulation outputs focus on those of *Position 2* (pos2) shown in Figure 3.3b since this was the only position used to take data with the detector for SR1, from May 24th to May 30th 2017. The statistics of a 10 million primary events simulation are shown below, in Table 3.1:

Table 3.1.: Statistics of a 10 million primary event NG simulation. See below text for comments.

Interactions within the TPC	1486537	14.9%
NR Scatters	174327	1.74%
NR Single Scatters	55987	0.56%
NR Double Scatters	36248	0.36%

where *NR Scatter* are particles whose first scatter within the TPC is a NR, *NR Single Scatters* are particles which deposit all their energy in a NR scatter and *NR Double Scatters* are particles which deposit all their energy in precisely two NR scatters. As shown, only around 15% of the primary particles (neutrons) reach the TPC and interact within.

This fraction is to be expected due to a couple of reasons. The production of neutrons (both in the real NG as in the G4 simulation) is isotropic, therefore a major part of the produced particles are not sent in the direction of the TPC, getting lost in the water tank. For instance, for pos2, considering a 2D approach², the efficient range for the angle of emission is 89° , resulting in only 20% of the overall 2π emission range. From those 20% who aim for the TPC, about a quarter lose their remaining energy traveling through 27.4 cm of water, the outer and inner cryostat stainless-steel walls and a 10 cm layer of LXe in between. Because of all these processes, the energy spectrum of neutrons that interact within the detector is very different from the primary spectrum of emission from the NG (Figure 3.6), featuring much lower energy particles than the ones emitted, as well as photopeaks from scatters in the detector materials:

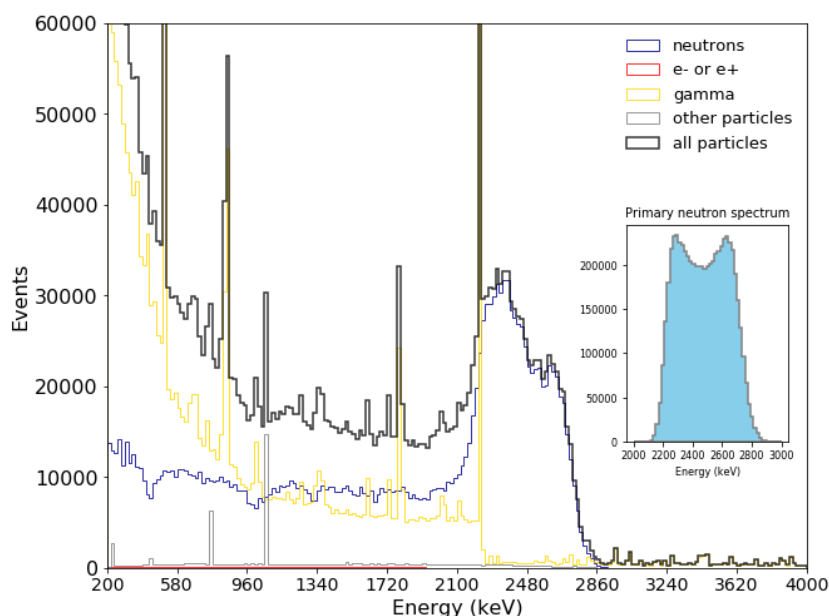


Figure 3.6.: Energy spectrum of simulated particles that reach the cryostat. Of these, only a small fraction gets transported into the target volume and interacts within.

²Since the NG is positioned at a depth coincident with the middle of the detector, the 2D approximation is reasonable, excluding only the neutrons that travel above and below the TPC and did not get absorbed by the water.

the huge 2224 keV peak comes from emitted gammas after an electron capture process in ${}^2\text{H}$, or water in this instance; the 1778 keV peak appears from activated aluminum of the cryostat [71]; the 847 keV peak originates in activated copper [72]; the 511 keV comes from electron-positron pairs annihilation. Pair production is expected to happen due to the high energy gammas from neutron capture in water making the last process noticeable.

The input spectrum, that is, the energy spectrum of the neutrons emitted by the NG, is shown as an inset plot on the right side and features the D-D neutron distribution from Figure 3.5. Due to the interactions happening between the emission site and the target volume, different particles appear, namely electrons, positrons, gamma rays, neutrinos, anti-neutrinos and ions (${}^{125}\text{I}$ and ${}^{135}\text{Cs}$ from detector materials). The majority of these “contaminating” particles will give origin to electronic recoil (ER) interactions, considering they are charged or gamma particles and can, therefore, be distinguished from neutron NR interactions (as explained in Section 2.3.1).

The spacial distribution of the first scatters for each simulated particle that reaches the target volume is shown in Figure 3.7, as well as the spectrum of the deposited energy from both ER and NR scatters is studied. The low-energy NR single scatters (0-70 keV), similar to the expected WIMP-like NR energies, are the main calibration events responsible for the computation of light and charge yields for NR interaction in the detector, ultimately one of the major goals for this calibration. As for the spacial distribution of events in the TPC volume, it is worth noting that there are progressively less events moving away from the NG and, due to the stopping power of LXe, there is an excess of ER scatters near the walls, not noticed for NR scatters. These events will later on get excluded by the fiducial volume cut, reducing the number of ER events considerably.

3.3. Calibration data analysis and data-mc matching study

3.3.1. Neutron generator data taken during SR1 and analysis cuts

As mentioned above, before the end of SR1, the TPC was only irradiated from pos2, acquiring 0.73 days of NG data, with enough events for statistical analysis. Because of

the time loss in mounting and moving the generator, adding up to the time needed for the activated radioactive isotopes from neutron interactions to fully decay ($^{131\text{m}}\text{Xe}$ 163.9 keV, 11.93 days half-life decay [73] or $^{129\text{m}}\text{Xe}$ 236.2 keV, 8.88 days half-life decay [74] and others), only after the end of SR1 more NG data was taken. From March 13th to 31st 2018, the TPC was irradiated from all three predetermined positions (pos1, pos2 and pos3 in Figure 3.3b), in order to fully cover the TPC area and acquire more NR calibration data for other science-related searches.

Table 3.2.: Coordinates of the NG positions in the water tank. The coordinate system is the same for simulation and analysis: x points to the closest wall of Hall B from the detector, with $x=0$ at the middle of the TPC, y to the water tank door, with $y=0$ at the middle of the TPC and z pointing downwards with $z=0$ at the grounded mesh.

Position	x (cm)	y (cm)	z (cm)	r (cm)
pos1	83.5	-39.0	-50.0	92.16
pos2	31.6	86.8	-50.0	92.37
pos3	-92.4	0	-50.0	92.4

Even though the computation of light and charge yields (Figure 2.8) is not covered in this work, this section studies the event selection of real data and how it

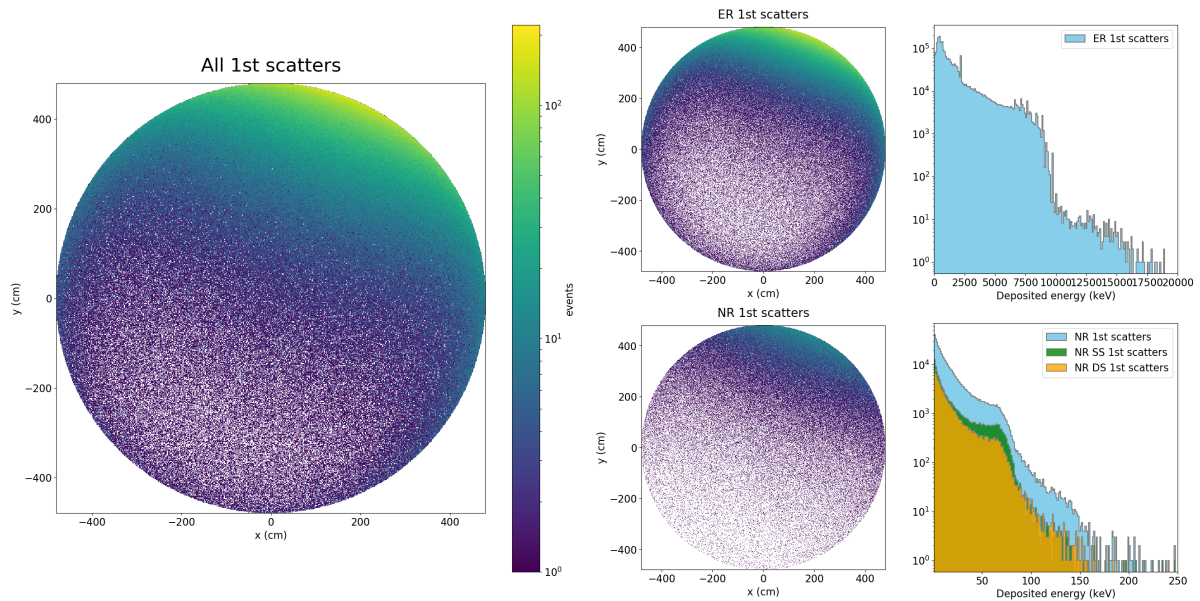


Figure 3.7.: From left to right, top to bottom: spatial distribution of all the first scatter of each particle track that reach the active volume, just the scatters corresponding to an ER and NR, respectively. On the right side, a spectrum of the deposited energy of each first scatter is shown for ER and NR events, as well as for pure single and double scatter NR events. See above text for discussion.

compares to simulated data. The simulated data is processed similarly to real data with the extra step of converting the deposited energy in each interaction, given by GEANT4, to S1 and S2 signals. This is accomplished with a python script, taking into account the known detector parameters, and FAX (*Fake XENON Experiment*), which simulates a real waveform from S1 and S2 simulated signals. The output of FAX is then treated as any other raw data from the real detector, getting processed by PAX (*Processor for Analyzing Xenon*, both the software and documentation are open-source at github.com/XENON1T/pax). PAX identifies S1 and S2 pulses and relates pairs that can correspond to an event (given compatible size and drift time), clusters and reconstructs the event and computes actual analysis-friendly information of such events like the S1 and S2 width, size, area and hit pattern on the PMT arrays or reconstructed position of interaction.

From then on, the analysis diverges into different topics and end-goals, focusing more on the study of low or high energy, ER ou NR both for the main Spin-Independent Dark Matter search as well as other physics channels. Nonetheless, a rigorous selection of events is always of great importance. In order to select events, given a set of conditions, a *cut* is applied. Cuts are used on different stages of any analysis, from checking if there was no coincident trigger in the muon-veto to selecting a particular type of event, like a single scatter NR or a decay from a Radon daughter. In the next paragraphs, the major cuts applied to NG real and full-chain simulated data and used in the analysis of SR1 will be loosely described below.

Data quality cuts

A first set of cuts assures that data was taken in proper conditions on the Data Acquisition System (DAQ) and triggers, as well as an almost 100% acceptance check if the identified main S1 and S2 peaks are the biggest in each waveform, as one expects. Moreover, all throughout the detector operation there were strange very intense light signals, registered just by some of the PMTs arround a focus point. These *flashes* are not yet completely understood but are expected to come from light emitting discharges happening inside of some PMTs. These signals, and some time after them, are also excluded from analysis with a proper cut. The last condition required for data quality is that the active muon veto was on and no signals were detected. Given that these cuts are equivalent to not take data during certain periods, they contribute to a reduction of livetime instead of lowering the acceptance of science data for DM search.

Event characterization and consistency cuts

From the huge amount of identified waveforms by PAX, some may not correspond to a real event in the target volume and must be removed from analysis. A few examples of these types of events are accidental coincidences (AC), where a light signal similar to a S2 is mistakenly matched with one or more S1 signals, events from the gas phase or below the cathode or even scintillation on the photocathode of a PMT. Both for the S1 and S2 of a waveform, the width and area of the signals along with the hit pattern on the PMT arrays are of great use to cut events. As the width of the S2 signal is energy dependent and increases with the depth of the interaction, cross checking the calculated z position from drift time measurements with this quantity identifies AC, gas phase or physically impossible events (updated version of the width consistency cut from [75]). The area of the S2 signals (measured on the top PMT array) is used alongside the S2 width to remove gas events. Both cuts target the same type of anomalous events and complete each other in their task (98% acceptance for DM SR1 data)

As mentioned in Section 2.3.3, some ER events might have lower S2/S1 ratio and leak into the NR band. This anomalous leakage events usually pass all mentioned cuts and can be present in the fiducial volume (explained below), therefore standing as a background in the region of interest (ROI). To remove these events, models of both S1 and S2 single-scatter hit patterns are simulated and each event is then tested with respect to the model. An energy dependent cut threshold is set to how far from the model an event can be (calculated with Log Likelihood test statistic methods), rejecting mostly poorly reconstructed and leakage events (>99% acceptance for S1 and 98% acceptance for S2 for DM SR1 data)

Fiducial Volume Cuts

Fiducialization is an important step into background reduction in LXe experiments. As explained in Section 2.3.3 of the last chapter, LXe has a high stopping power and can, therefore, be used as self-shielding. Choosing the right fiducial volume is no easy task because it greatly reduces the detector exposure. It should be the biggest region where the energy response and position reconstruction are well know and understood, while minimizing the number of background ER events (and other backgrounds) within and taking into account the energy region where the highest WIMP sensitivity is found.

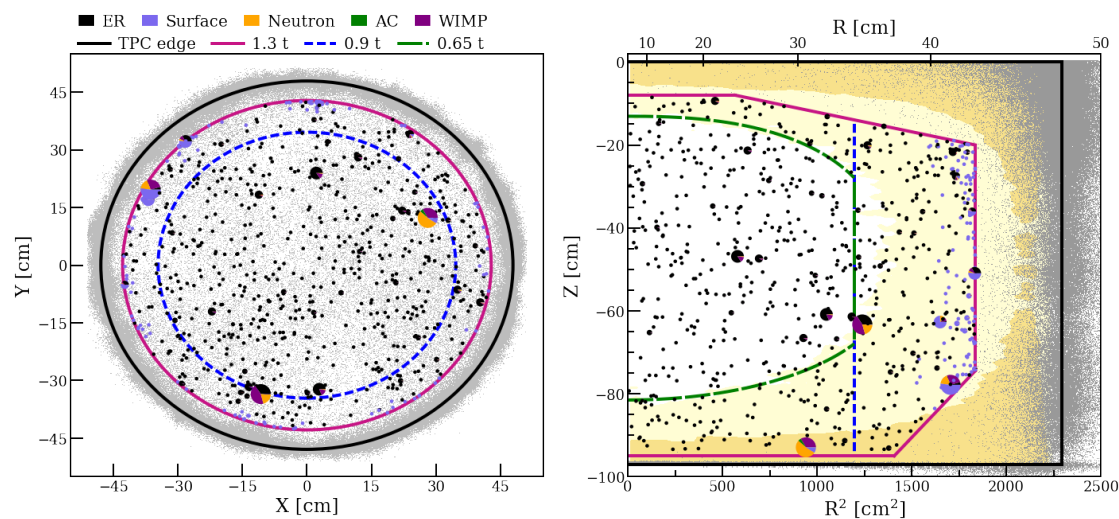


Figure 3.8.: Spatial distributions of DM search data during combined run SR0+SR1. The piecharts represent events that pass all selection cuts and are within the fiducial mass, each color representing the relative probabilities of the background and signal components under the best-fit model applied to a $200 \text{ GeV}/c^2$. Figure from [38].

In the end of SR1 analysis, the fiducial volume was set to be a carved rectangle (see Figure 3.8) with a maximum radius of 42.8387 cm , corresponding to a fiducial mass of 1315.9 kg .

Single Scatter Cuts

WIMP-nucleon interaction has a very low cross-section making the probability of a double scatter within the target volume negligible. For this reason, cuts to select single scatter events are crucial to DM search, as they are the only ones capable of removing neutron backgrounds, which are capable of multiple NR scatters inside the detection volume. The S1 signals from a double scatter are similar to the ones from a single scatter because even though the two interactions take place in the detector, given their time difference, the peaks get merged and are seen as only one signal. However, if each scatter is done at a different depth (z coordinate), multiple S2 peaks will be present in the waveform given their different drift times. They can then be identified and rejected. As for S1 single scatter analysis, a cut checks for secondary S1 signals that could produce valid interactions with the primary S2 using the aforementioned S2 width information. If the event passes this condition and, therefore, a valid interaction is

possible, the event is rejected. Both S1 and S2 single scatter cuts have >99% acceptance in SR1 DM data.

Blinding cuts

To ensure an unbiased tuning of cuts to select certain events, all events of the signal region of interest are removed from analysis until all cuts, fiducial mass boundaries and calculation procedures are settled and all background data taken. This is called a *Blinding Cut* and is applied to every background or low-rate calibration run. Since it only covers the signal ROI, around 99% of ERs stay available, as well as calibration data, in order to tune the analysis. This approach is the only way to prevent human bias and is set as a standard for all analyses to protect the integrity of the results obtained.

Furthermore, another adopted technique to remove human bias in analysis is *salt*ing the data, meaning that some events that might (or not) simulate a signal are put (or not) in the overall data for analysis. The salted events are only removed after the unblinding of data, its discussion and preliminary limit setting has taken place. With this approach, one is discouraged to active seek to remove a given potential signal event because it can be just a salted one.

More cuts not mentioned in this section were developed until the freezing of analysis for SR1 data unbinding, covering more variables and perfecting the selection criteria. As they get away from this work, more information can be found at references [75], [76], [38] and in a future dedicated paper on the analysis of XENON1T by Aprile, et al (XENON Collaboration).

3.3.2. Data-MC matching and cut acceptance comparison

As mentioned in the last section, simulated data from G4 can be arranged to be processed like real data, getting to use the same analysis tools and cuts. During the tuning of event selection cuts, this has a great potential to check for errors and bugs related with certain variables in cut definitions and compare the expected acceptance from simulation with the one registered in real data. This type of MC-Data cross check is done below for the neutron generator runs of SR1.

During SR1, 1.51 days of recorded data were taken with the neutron generator at position 2 (see Table 3.2 on the week of 24th to 31st of May 2017).

Table 3.3.: Number of events of both simulated (MC) and taken neutron generator data. The percentages are calculated in respect to the total number of events (without $cs1 < 100$ pe pre-selection)

	total events	events with $cs1 < 200$ pe	events after all cuts
MC	322511	24372 (7.56%)	2212 (0.68%)
Real data	4476708	144150 (3.22%)	7415 (0.16%)

Figure 3.9, Figure 3.10 and Figure 3.11 are an important first step to look into similarities and major differences between simulated and real data. The same set of cuts was applied to both datasets for a proper comparison. At first sight it stands out that a fraction of the events appear to happen outside of the TPC, which is a contradiction. The problem lies in the reconstruction of events by PAX, which given certain hit patterns in the PMT arrays tends to reconstruct events in the wall of the TPC or near it. As these events are reconstructed outside the fiducial volume, they do not stand a major concern directly but only as feature to improve in the processor. The fiducial volume cut considered for this analysis, *NGFiducial*, is defined as the 1 tonne volume cylinder in the center of the TPC, standard for XENON1T, imposing a maximum distance between the reconstructed position and the neutron source. Considering the distance to the neutron source in the cut definition reduces the amount of ER events that are not from inelastic scattering of neutrons:

Listing 3.1: Definition of the NGFiducial cut

```

1 source_position = (31.6, 86.8, -50)
2 df.loc[:, 'distance_to_source'] = ((source_position[0] - df['x'])**2 +
3                                     (source_position[1] - df['y'])**2 +
4                                     (source_position[2] - df['z'])**2)**0.5)
5 cut = (distance_to_source < 111.5) & (-92.9 < z) & (z < -9) & (sqrt(x*x +
   y*y) < 42.00)

```

On the other hand, Figure 3.11 makes emphasis on the energy and characterization cuts efficiency. On both simulated and real data, the complete set of events cover mostly the NR band but not solely, showing contamination events from ER and spurious origins (AC, wall leakage, gas). As expected, even with a very complete model, the real data shows a considerable increase in the topology of events in $cs2/cs1$ space. For instance, the events below the NR band, not present in the simulation, are

mostly likely to come from interactions where the measured S2 is smaller than the one expected from its S1 counterpart. This is a known feature of the detector for events near the TPC wall from which drifting electrons get stuck in the PTFE walls and do not reach the gas phase, originating small size S2s. In the end, the set of cuts applied identify and remove the majority of unwanted events and the resulting spectra are alike.

Individual cut acceptance

In order to compare how each cut affects the final selection of events, as well as how this selection compares from simulation to real data, a study of each cut acceptance was developed. Different approaches could be taken to measure the acceptance of each cut and how it behaves. Taking into account that this work does not focus on tuning each individual cut but instead look into the similarities between real and monte carlo data, the N-1 procedure was chosen. This approach applies every cut except the cut whose acceptance is being calculated and takes the resulting dataset as input for the intended cut to be applied on. This method is preferable to applying the cut of interest directly to the whole dataset since it reflects which events are selected by it and no other. For this same reason, cuts that might be correlated must be avoided or not applied when studying each other, which is not the case for the set of cuts studied here.

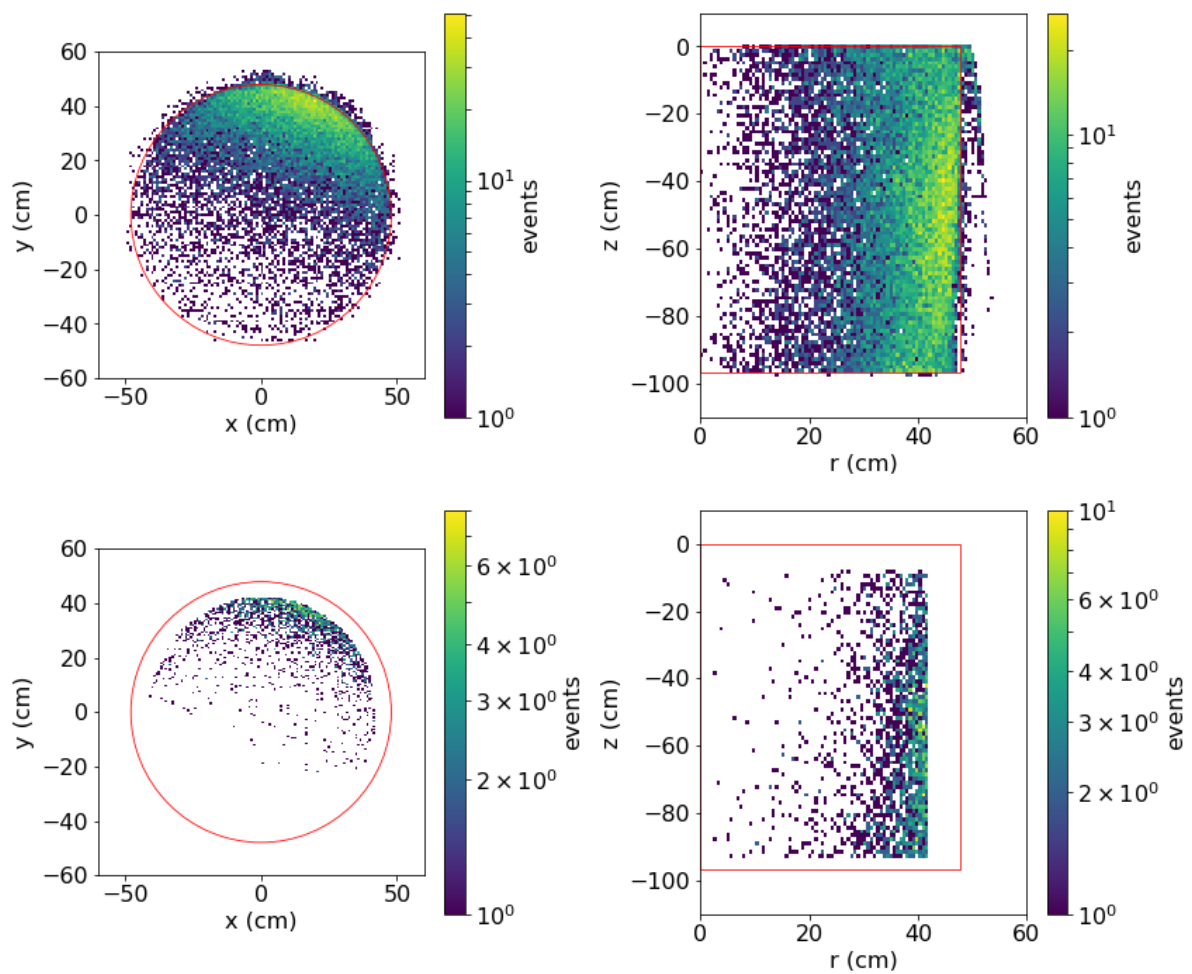


Figure 3.9.: Spacial distribution on the x vs y and z vs r planes of full-chain simulated events from a neutron generator run . The whole set of events is shown in the top plots of each figure and the selected events after cuts in hte bottom plots of each figure. The TPC boundary is shown in red for reference. The fiducial volume is set with the cut defined in listing 3.1.

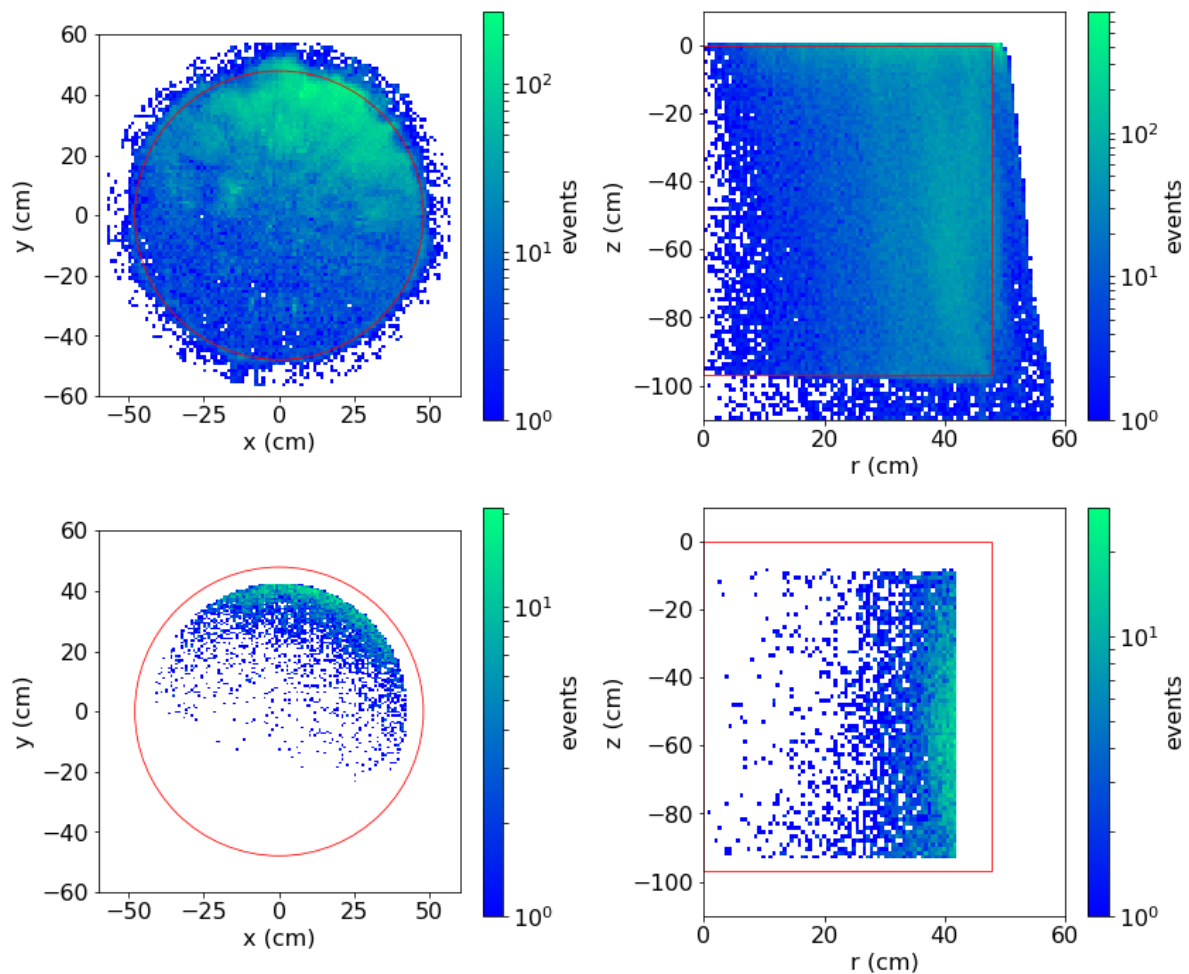


Figure 3.10.: Spatial distribution on the x vs y and z vs r planes of real events from a neutron generator run. The whole set of events is shown in the top plots of each figure and the selected events after cuts in the bottom plots of each figure. The TPC boundary is shown in red for reference. The fiducial volume is set with the cut defined in listing 3.1.

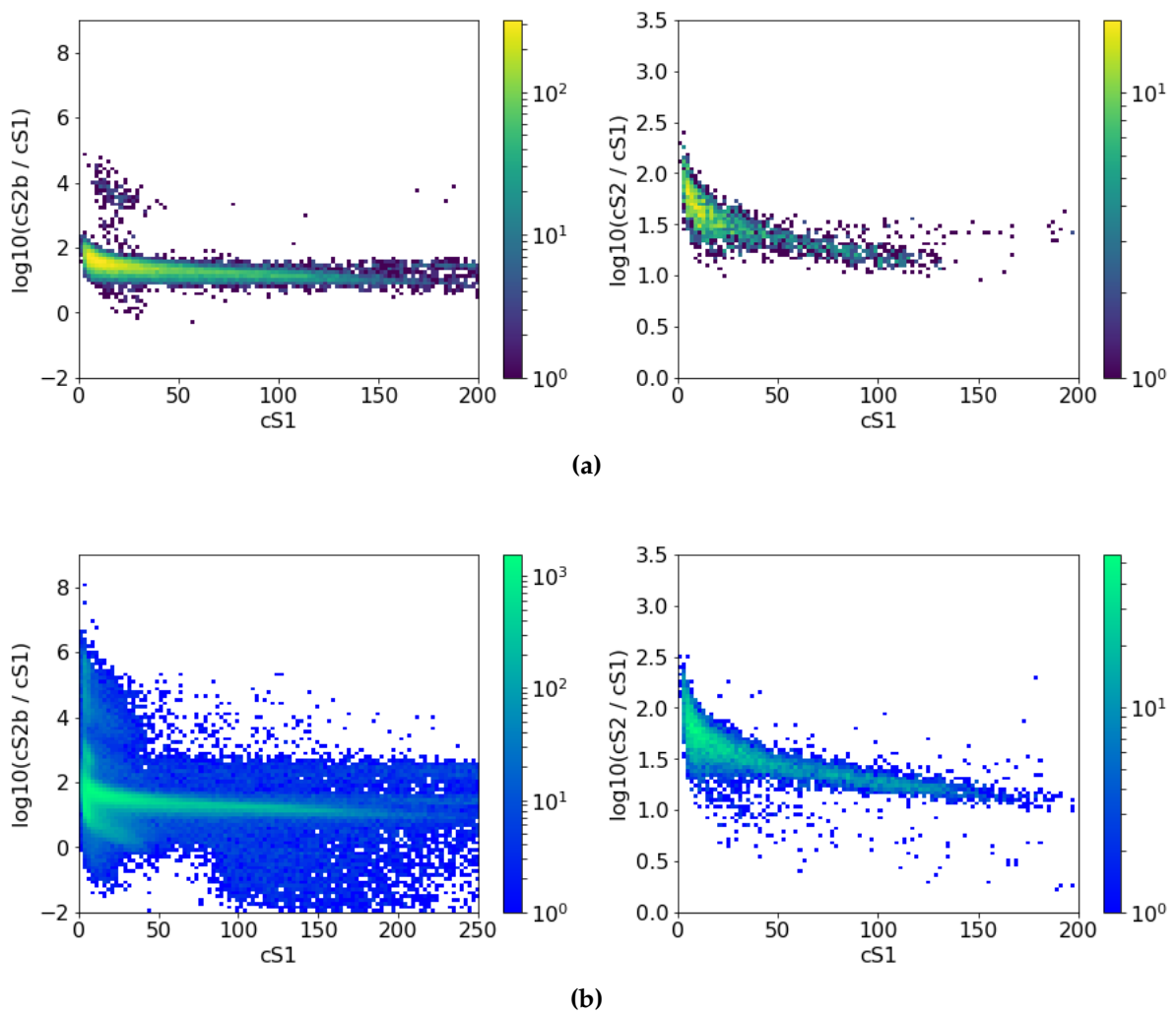
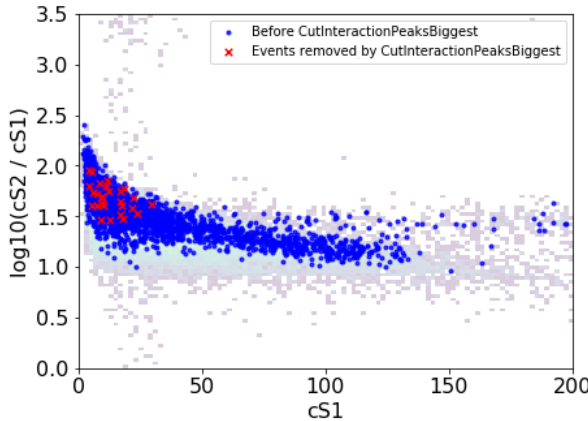
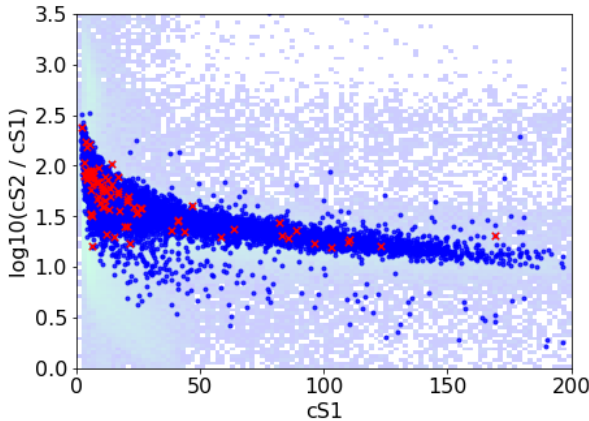
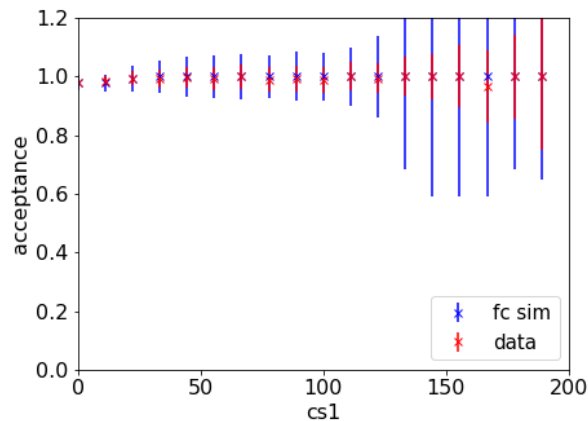
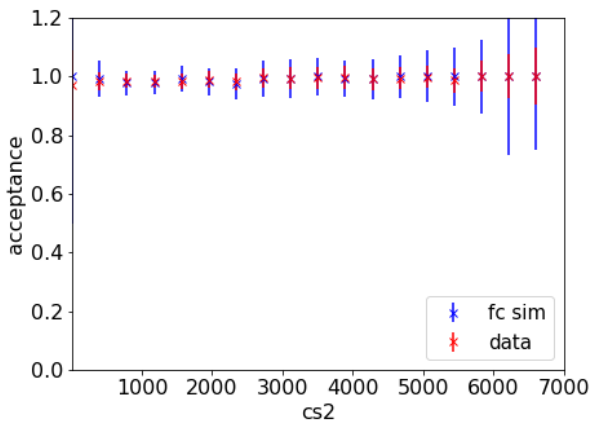


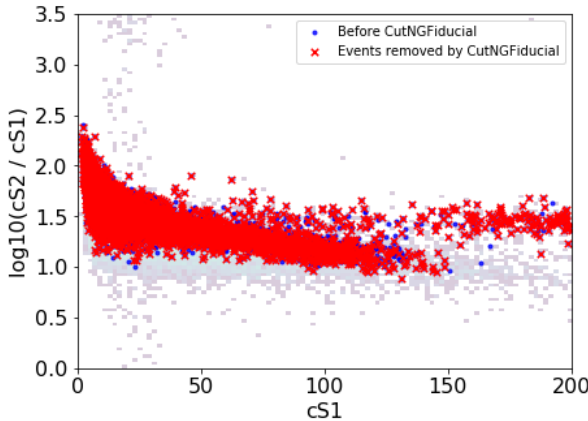
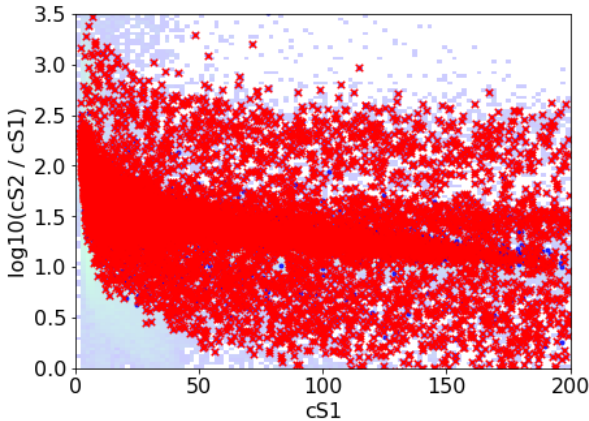
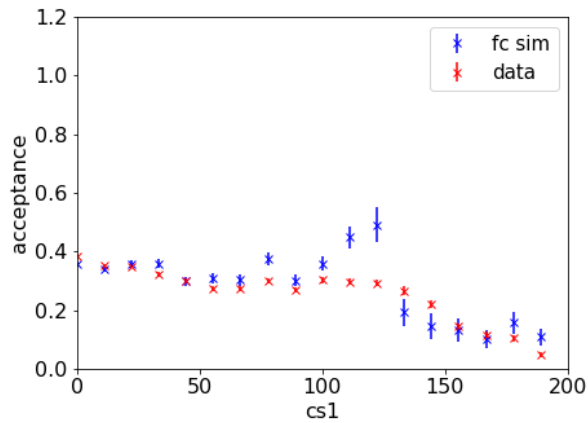
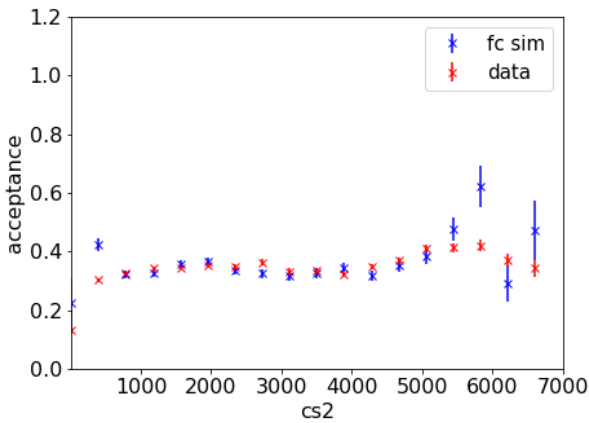
Figure 3.11.: $cS2/cS1$ versus $cS1$ spectrum of simulated (a) and real (b) events from a neutron generator run. Plots on the left side show data without cuts and on the right side data with all the cuts applied (more details in text).

Table 3.4.: Statistics and spectrum of CutInteractionPeaksBiggest

CutInteractionPeaksBiggest	
Motivation	
Ensures that the S1 and S2 of the main interaction are the largest ones on the waveform [77]	
Monte Carlo	Real data taken
Acceptance as 1st cut	
97.53%	86.60%
Acceptance as Nth cut	
98.79%	98.91%
cS2/cS1 spectrum	
	
Acceptance	
	
Comments	

The CutInteractionPeaksBiggest is important due to its ability to loosely select single scatter events, correlating with CutS2SingleScatter up to a certain extent. As of later iterations of PAX (after this data was processed) the amount of wrong classifications of main S1s and S2s is almost negligible and its scatter characterization capabilities get surpassed by S1 and S2 Single Scatter cuts.

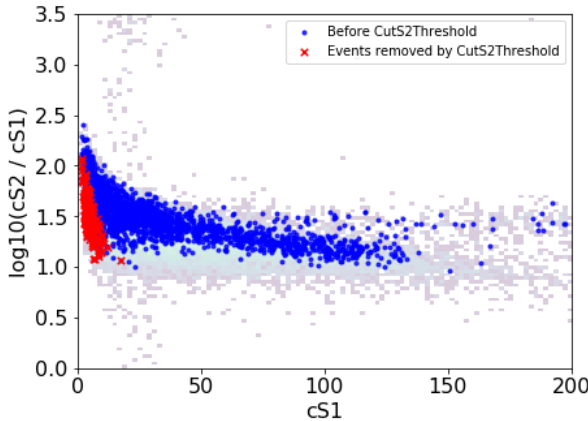
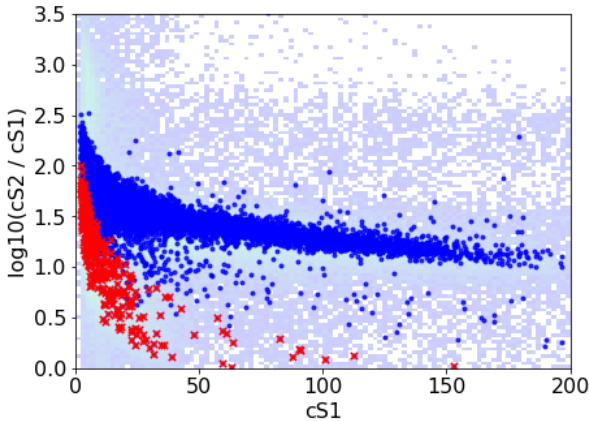
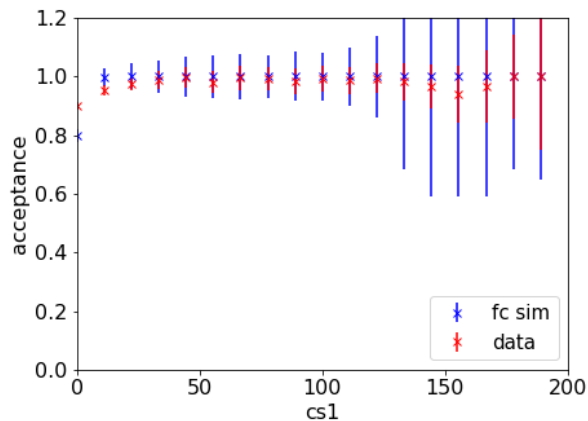
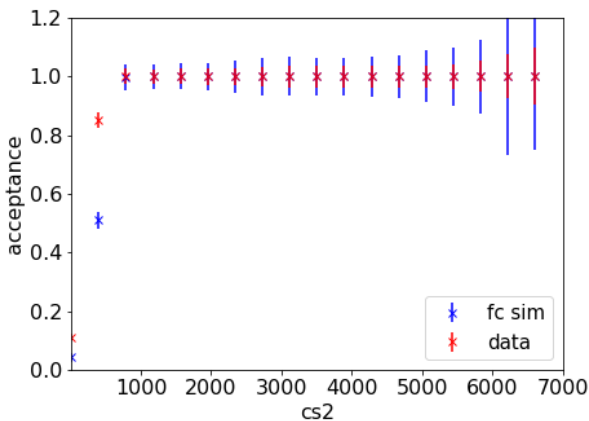
Table 3.5.: Statistics and spectrum of CutNGFiducial

CutNGFiducial	
Motivation	
Removes events outside of a defined fiducial volume, mainly ER background	
Monte Carlo	Real data taken
Acceptance as 1st cut	
50.54%	46.21%
Acceptance as Nth cut	
33.95%	32.08%
cS2/cS1 spectrum	
	
Acceptance	
	

Comments

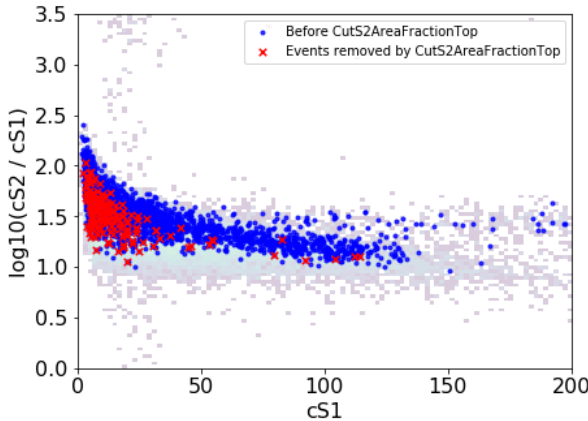
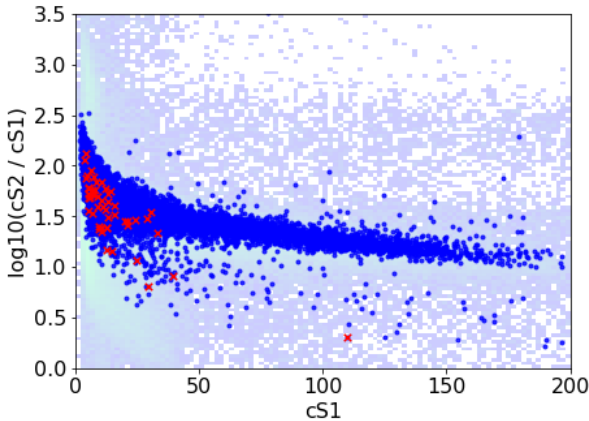
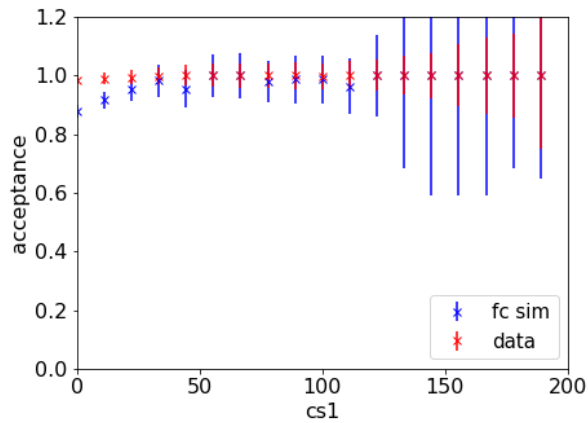
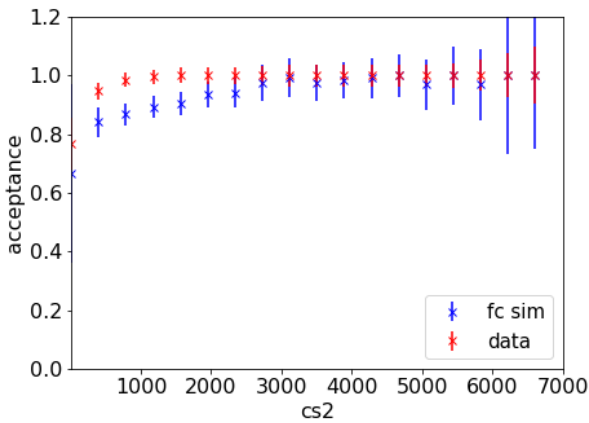
The fiducial cut applied, detailed in 3.1, has a large effect on the ER events, as expected. Its acceptance is as low as less than 35% for both MC and real data. Not only does it target the ER band but also removes a large amount of leakage events, as seen in the above spectrum.

Table 3.6.: Statistics and spectrum of CutS2Threshold

CutS2Threshold	
Motivation	
Removes events for which the trigger is not perfectly efficient [78]	
Monte Carlo	Real data taken
Acceptance as 1st cut	
95.97%	84.79%
Acceptance as Nth cut	
93.10%	95.52%
cS2/cS1 spectrum	
	
Acceptance	
	
Comments	

This cut ensures all events registered are properly processed, selecting only events with $S2 > 200$. The trigger and processing efficiency was increased in later versions of PAX, decreasing the limit of this cut and raising acceptance for small S1 and S2 interactions.

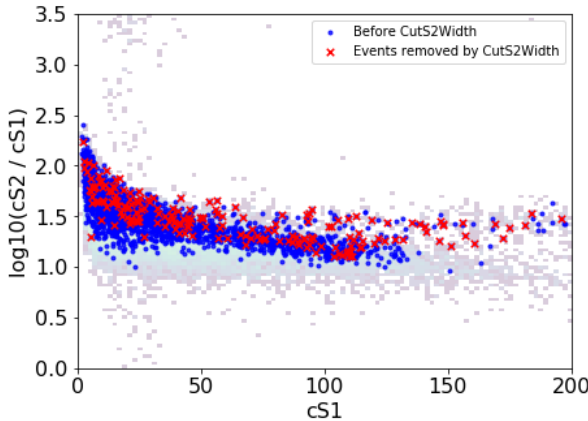
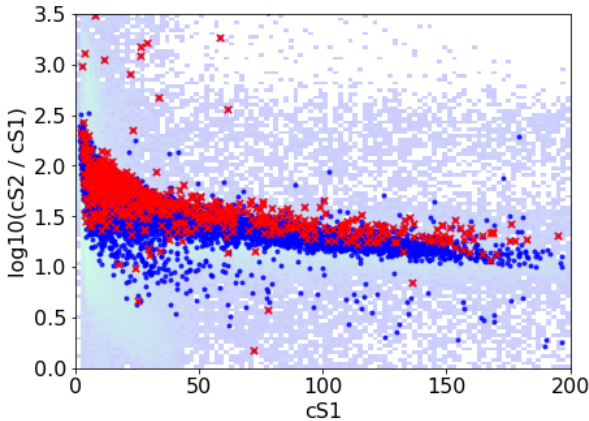
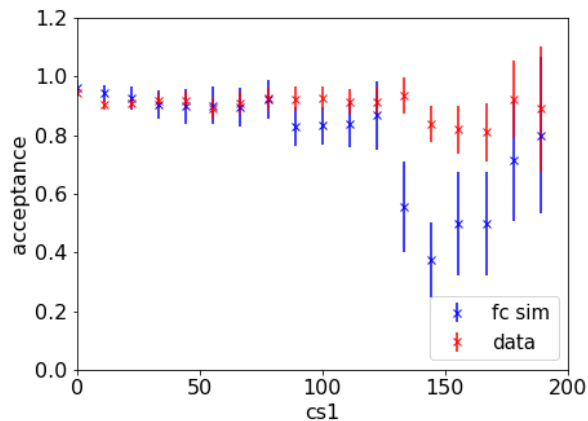
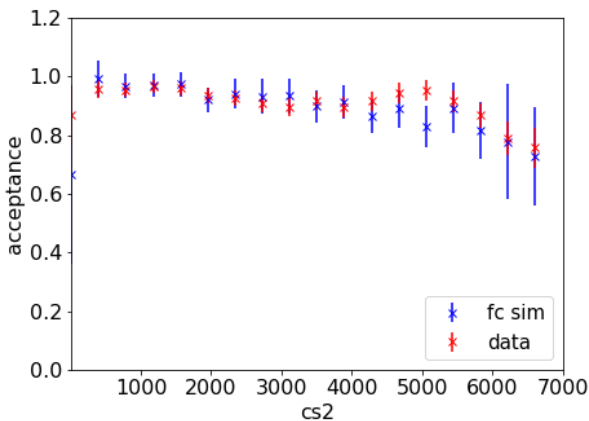
Table 3.7.: Statistics and spectrum of CutS2AreaFractionTop

CutS2AreaFractionTop	
Motivation	
Aims to remove gas events and other strange events [79]	
Monte Carlo	Real data taken
Acceptance as 1st cut	
92.85%	89.36%
Acceptance as Nth cut	
93.10%	99.32%
cS2/cS1 spectrum	
	
Acceptance	
	

Comments

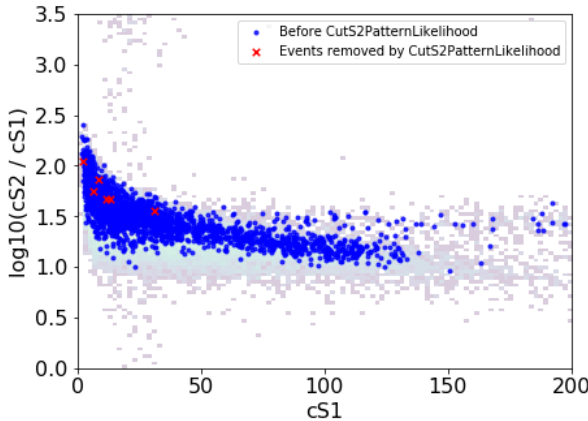
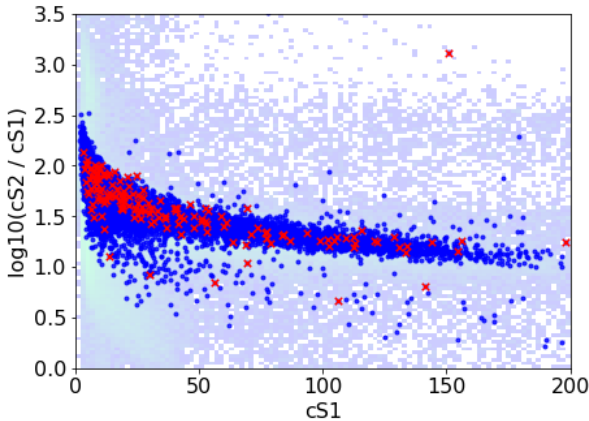
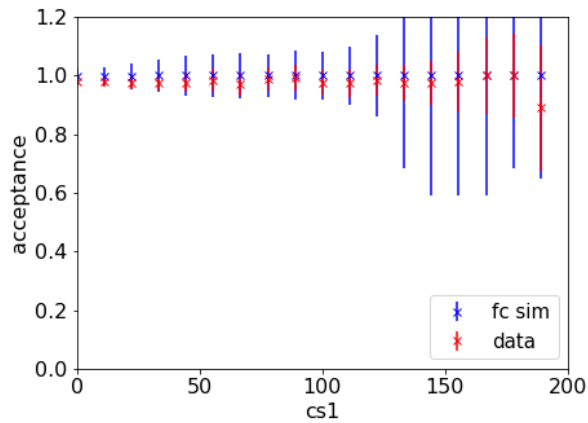
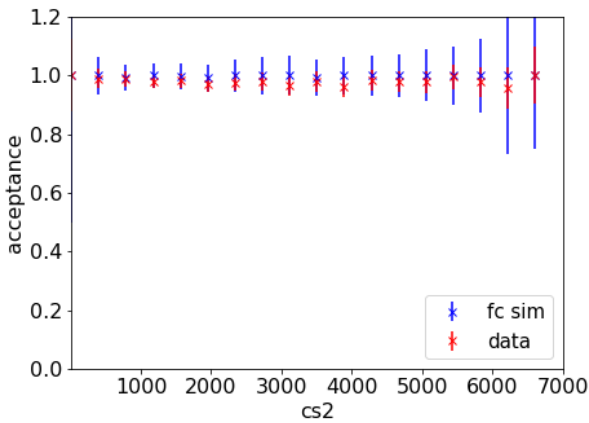
The CutS2AreaFractionTop set limits on the area of an s2 on the top PMT array. Cuts a major part of gas events, which display a particularly large S2 area on top array, as well as other strange events with low s2 area. The next cut shown, CutS2Width, also removes this type of events, however neither is perfectly efficient and therefore both are complementary.

Table 3.8.: Statistics and spectrum of CutS2Width

CutS2Width	
Motivation	
Remove gas events and events with un-physical drift time [80]	
Monte Carlo	Real data taken
Acceptance as 1st cut	
89.14%	71.95%
Acceptance as Nth cut	
91.78%	91.82%
cS2/cS1 spectrum	
	
Acceptance	
	
Comments	

As explained in the text early in this chapter, one can correlate the depth of the interaction with the width of the S2 signal, given a tuned drift and diffusion model and the single electron width. Using this cut, a large amount of leakage events contained in the NR band are removed, as one notices in the above plots. In conjunction with CutS2AreaFractionTop, the majority of gas events and accidental coincidences are removed

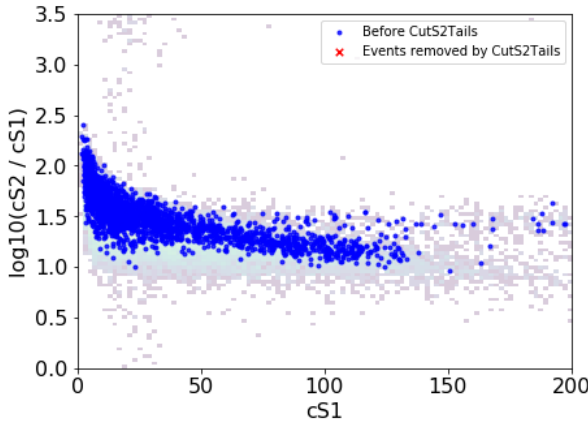
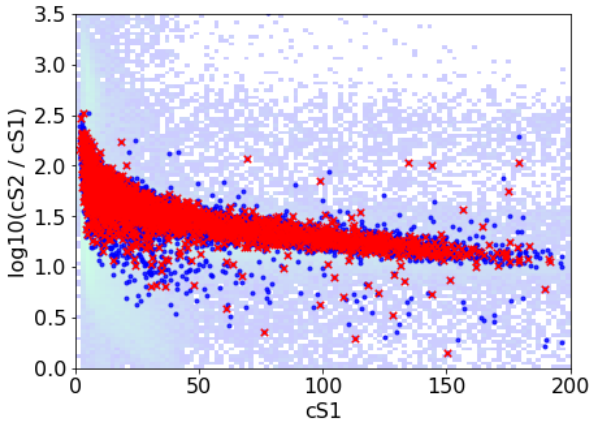
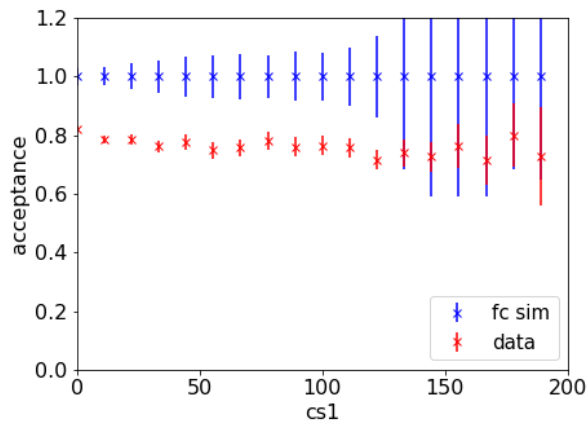
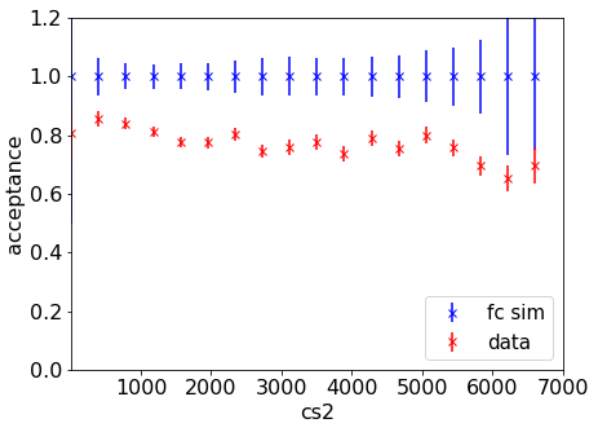
Table 3.9.: Statistics and spectrum of CutS2PatternLikelihood

CutS2PatternLikelihood	
Motivation	
Remove badly reconstructed S2s and multiple scatters [81]	
Monte Carlo	Real data taken
Acceptance as 1st cut	
98.65%	79.36%
Acceptance as Nth cut	
99.73%	97.86%
cS2/cS1 spectrum	
	
Acceptance	
	

Comments

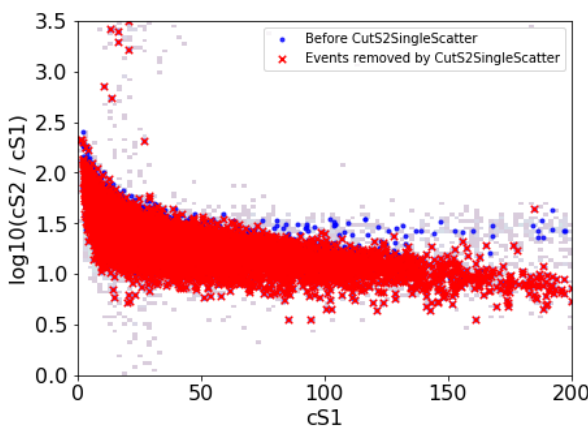
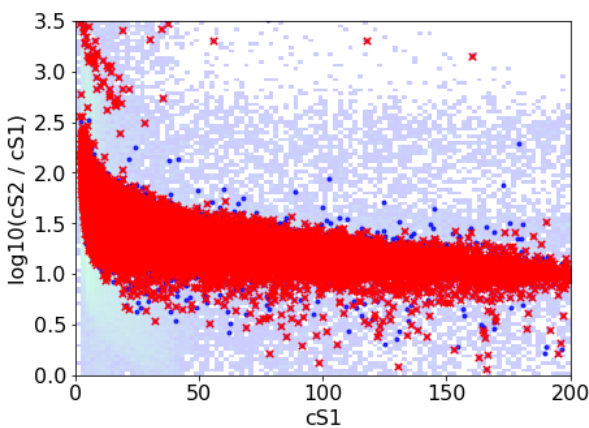
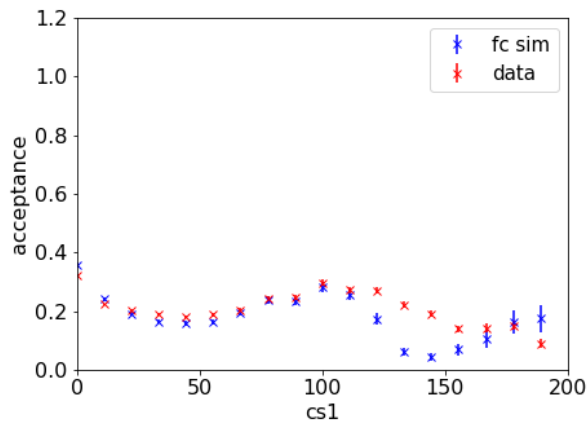
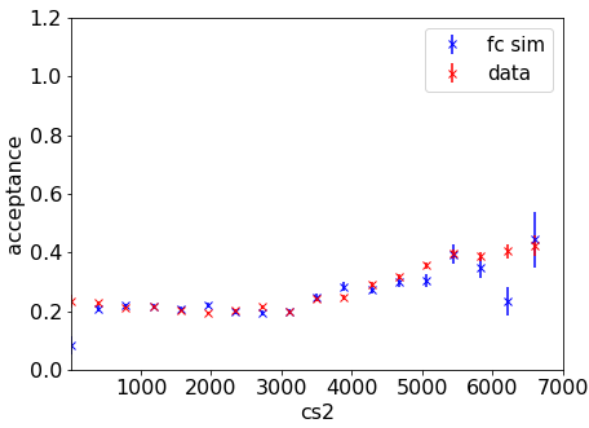
When selecting single scatters the expected S2 hit-pattern (the pattern of light hits in the top PMT array) must contain only one maximum. Hit-patterns which show more than one maximum are likely multiple scatters, merged interactions or badly reconstructed events. A goodness of fit of the hit-pattern is quantified by its p-value and constrained by this cut

Table 3.10.: Statistics and spectrum of CutS2Tails

CutS2Tails	
Motivation	
Removes events in a tail of a previous S2 [82]	
Monte Carlo	Real data taken
Acceptance as 1st cut	
100.00%	66.79%
Acceptance as Nth cut	
100.00%	78.23%
cS2/cS1 spectrum	
	
Acceptance	
	
Comments	

Big S2s signals usually leave a decreasing in time tail. To reduce the contribution of accidental coincidence events, any event with a S2 within this period is dismissed. Since this cut removes events based only on other events and not itself, it can be taken as a lifetime reduction without bias.

Table 3.11.: Statistics and spectrum of CutS2SingleScatter

CutS2SingleScatter	
Motivation	
Selecting single scatter events [83]	
Monte Carlo	Real data taken
Acceptance as 1st cut	
34.07%	30.25%
Acceptance as Nth cut	
23.00%	23.27%
cS2/cS1 spectrum	
	
Acceptance	
	
Comments	

The single scatter cuts aim to remove multiple scatter events and is crucial for discriminating neutron background (which can be multiple scatters) from WIMP-like signals (exclusively single scatters). The CutS2SingleScatter removes events that feature at least one secondary S2 signal above a certain energy dependent threshold. As seen in the above plots, the cut has a very low acceptance for neutron events, as one would expect from double scatter rich interactions

3.3.3. Post-SR1 NG data analysis

Data taken

After SR1 data taking ended, more calibration data was acquired in order to pursue the detailed study of the XENON1T detector and ensure enough calibration data for other science-related searches. In line with these efforts, around two more weeks of neutron generator operation were scheduled, from the 13th to the 31st of March 2018. Contrary to SR1 NG data, all three predetermined positions of the Neutron Generator were used (see Figure 3.3b), also performing as a tool to deeply study the detector's reconstruction spacial dependence. The study conducted in this work does not aim to get a final NR calibration result on light or charge yields but focus on applying SR1 cuts, the resulting spacial distribution and signal spectrum as well as an empirically fitted NR band [84].

The data was taken through four different runs, one for each position with the neutron generator on the middle of the TPC and one run in Pos1 with the NG below the cathode. This later mentioned run was not considered for analysis in this work because of the increased number of unwanted and poor spacially spread events over the active volume.

Table 3.12.: General statistics of neutron generator runs after SR1. Run 2 is not considered for the *Total* row, as its data is not used in this analysis. The *Number of events* column refer to all the interactions that triggered the DAQ system and got registered.

Run number	NG position	Data ac- quired (days)	Number of events	Event rate (Hz)
Run 1	Pos1	2.75	6210186	26.1
Run 2	Pos1, 20 cm below cathode	2.42	4337810	20.76
Run 3	Pos2	2.34	4587549	22.73
Run 4	Pos3	1.75	3355639	22.17
Total	Pos1-3, z=-50	6.84	14153374	23.94

Cuts applied to data

In total, 6.84 days of data (before dead time and data quality checks) were taken with the NG in the middle height of the TPC ($z=-50$). Notice that from all the triggered events registered, shown in Table 3.12, after processing, only a fraction of those will converge into waveforms. Then, pre-selection of $cs1 < 200$ pe is applied to focus on low energy events, lowering the number of useful events for analysis to 443586. The distribution of such events is shown in Figure 3.12 in x vs y , r vs z and $cs2/cs1$ vs $cs1$ parameters space, as well as the selected events after applying a wide range of cuts. Overall, no major difference between positions was detected in cut acceptance, fluctuating less than 3% for almost every cut.

Table 3.13.: Cuts applied to NG data taken post-SR1 and their acceptance. The fraction of events passed is determined with a iterative method, each cut applied after the one above and the number of removed events as the difference between these two sets.

Cut	Fraction of events passed (iteratively)		
	Pos1	Pos2	Pos3
InteractionExists	100%	100%	100%
InteractionPeaksBiggest [77]	90.70%	89.58%	88.68%
DAQVeto [85]	90.94%	92.89%	93.02%
S2Threshold [78]	95.14%	94.10%	92.64%
S2AreaFractionTop [79]	95.47%	95.02%	94.03%
S2Width [80]	84.11%	81.39%	76.66%
S1AreaFractionTop [86]	98.38%	98.14%	97.78%
S2PatternLikelihood [81]	93.53%	93.53%	91.96%
SingleElectronS2s [87]	97.91%	97.91%	97.66%
S2Tails [82]	76.85%	76.85%	91.00%
S1MaxPMT [88]	97.07%	97.07%	97.24%
S1SingleScatter [89]	98.55%	98.55%	98.24%
S2SingleScatter [83]	36.39%	36.39%	34.94%
FiducialCylinder1T	9.38%	8.91%	8.62%
All cuts	1.42%	1.46%	1.27%

After all the cuts mentioned of Table 3.13, considering the sum of all three positions, the total number of events has come **from 443586 to 6224**, meaning an average of 1.4%

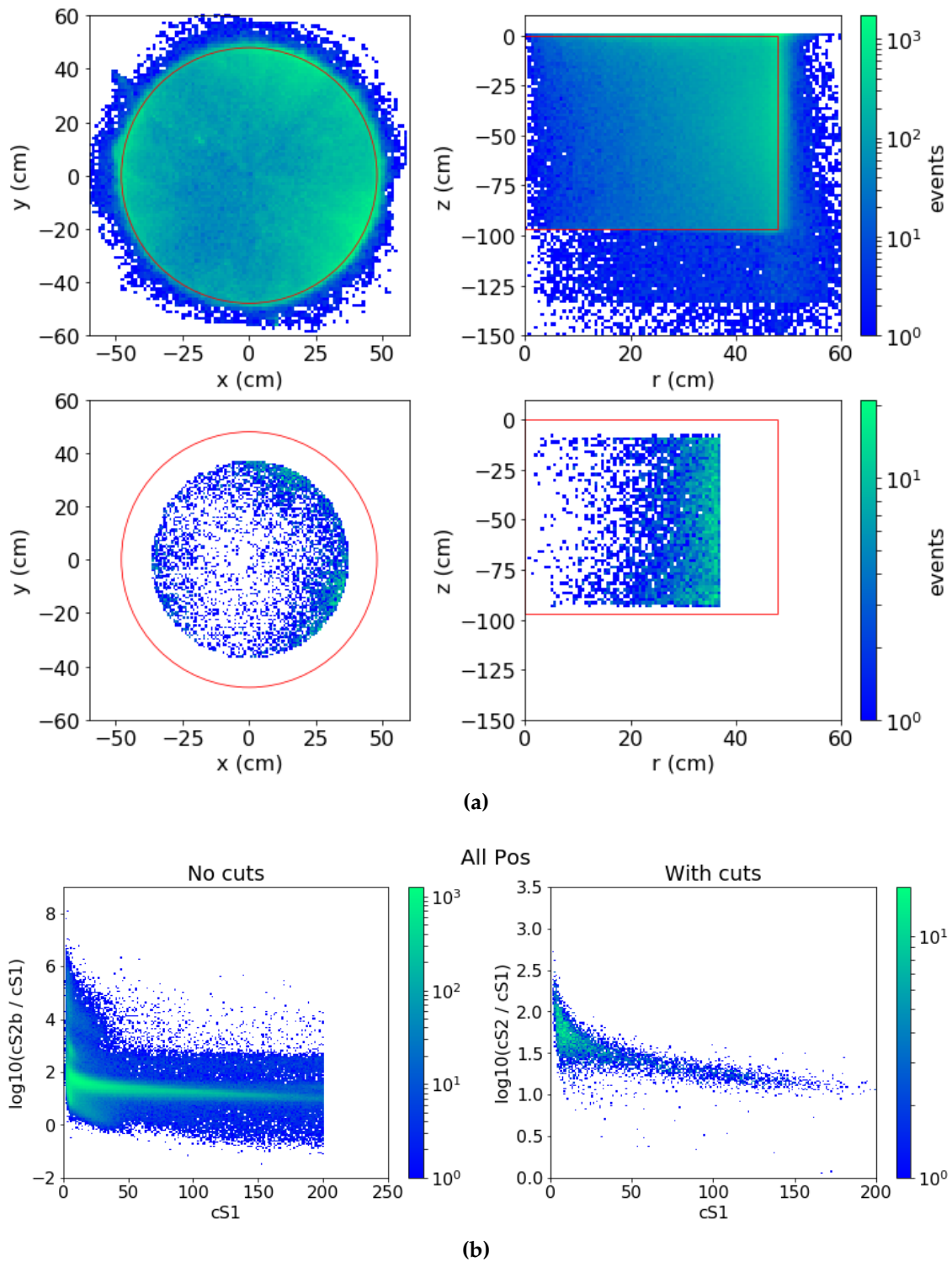


Figure 3.12.: Spatial distribution (a) and $cs2/cs1$ spectrum (b) of post-SR1 NG runs before and after the cuts mentioned in Table 3.13 applied.

total acceptance. Position 3 stands out as the lowest acceptance fraction of all three positions mainly due to the low acceptance on S2Width cut.

There is no trivial answer to this behavior as the distance from the neutron source to the TPC is the same in all positions. A possible cause of this effect is not related to the calibration data itself but to the presence of an unknown origin *hotspot* around $x = -20, y = 15$. The *hotspot* was present during the calibration runs presented here, and can be noticed in Figure 3.12a, upper-left corner plot. It features major light emission, captured mostly by PMT 87 on the top array. Although it is an operation problem and pushes the DAQ and trigger systems to levels out of the norm, it does not stand a problem for analysis as all the signals from it get removed. Since position 3 is the closest to the *hotspot*, the number of mismatching S1s-S2s or merged peaks, causing the S2Width cut to trigger, might be higher due to the continuous large amount of light triggering the detector.

Despite this feature, the data quality and thorough selection after every cut applied remains good and displays the expected NR band events, as seen in Figure 3.12b. However, some low *cS2 leakage events* are noticeable below the main NR band that can be identified considering:

$$1.1 < \frac{cS2_b}{cS1} < 3 \quad (3.3)$$

In an effort to reduce the amount of these leakage events in a non-biased approach, a threshold was set on the distance between the reconstructed interaction site and the source position. The tuning of this distance aims to maximize the volume considered while minimizing the number of leakage events. The cut threshold was set to 83 cm based on the plots in Figure 3.13.

Table 3.14.: Statistics of the *distance to source* cut applied to the data taken

Source position	Events removed	Fraction passed	Events left	Fraction passed all cuts
Pos1	593	78.68%	2188	1.12%
Pos2	465	79.10%	1760	1.16%
Pos3	348	71.43%	870	0.90%
Total	1406	77.41%	4818	1.09%

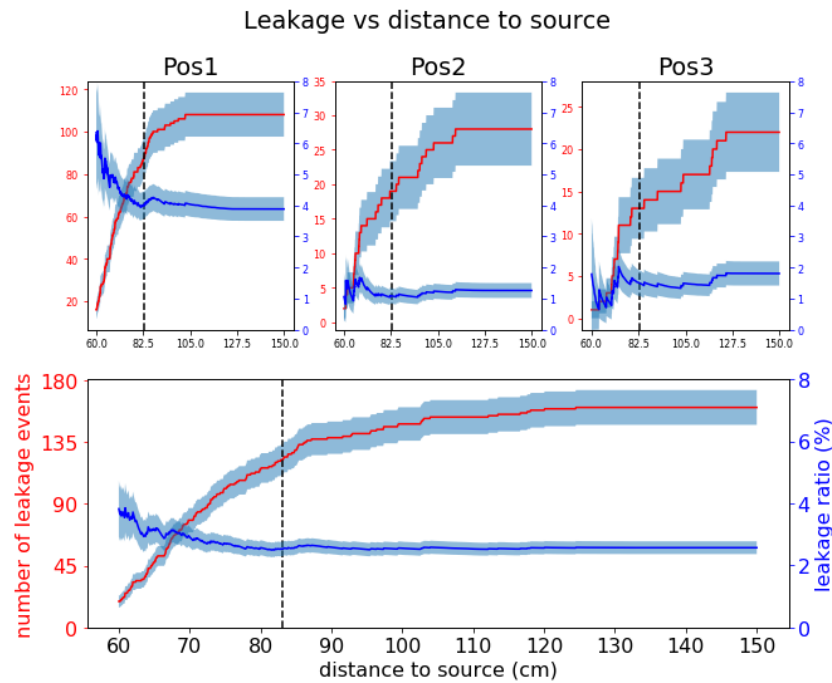


Figure 3.13.: Plots of the ratio of leakage events over the total events (blue) and the absolute number of surviving leakage events as a function of the distance between the positions of interaction and neutron source. The cut parameter was set to 83 cm considering an effort to maximize fiducial volume while minimizing the number of leakage events.

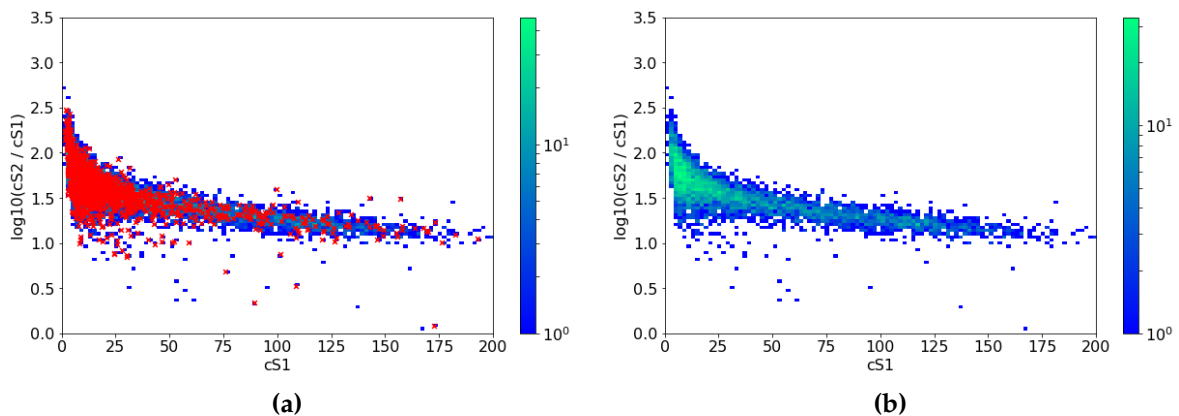


Figure 3.14.: cs_2/cs_1 vs cs_1 spectra before (a) and after (b) the *distance to source* cut application. In (a), the events that do not pass the cut are marker with a red cross. Although a considerable number of leakage events get selected, the majority does not get removed.

After applying the described *distance to source* cut, from a total of 160 events identified as leakage, 38 (23.75%) were removed. Since considering only leakage

region on cs_2 , cs_1 would be largely biased, many other events were cut due to their high distance to the source. The results of this procedure are shown in Table 3.14 and in Figure 3.14, where it is clear that, although reduced, the majority of leakage events are still present (around 76%). Different approaches could be taken in order to remove these spurious events, studying what is their nature and which parameter space would be correct to tune a cut, while remaining unbiased in cs_2/cs_1 vs cs_1 space. Nonetheless, the number of such events has been reduced to a manageable level where they do not greatly interfere with setting a reference band for the main distribution.

NR band fitting

In the previous pages, a careful selection of events was implemented to get as close as possible to clean NR single-scatter events from a neutron generator calibration. Finally, one can aim at one of the main objectives of such calibrations: getting fitting parameters for the NR band. Describing the expected single scatter NR spectrum band is of great importance as it defines the region of interest for WIMP-like events and therefore the boundaries of the blind region and the potential candidates after unblinding.

In this work, from selected NG data in cs_2/cs_1 vs cs_1 parameter space, the median, 5th and 95th percentiles were calculated independently for $1 < cs_1 < 150$ with 60 bins for each individual NG position as reference and 100 bins for the summed dataset.

The percentile points were fitted using the `scipy.optimize.curve_fit` module [90] for Python 3 [91] to the empirical function:

$$f(cs_1) = a \times e^{-\frac{cs_1}{b}} + c - d \times cs_1 \quad (3.4)$$

where a , b , c and d are the fitting parameters. The initial guess set for the parameters was the same for all of the three fits:

$$\begin{aligned} a_0 &= 28.12 & c_0 &= 1.38 \\ b_0 &= 0.687 & d_0 &= 0.0021 \end{aligned}$$

All the fits converged, resulting in the parameters shown in Table 3.15 and resulting plots in Figure 3.16a.

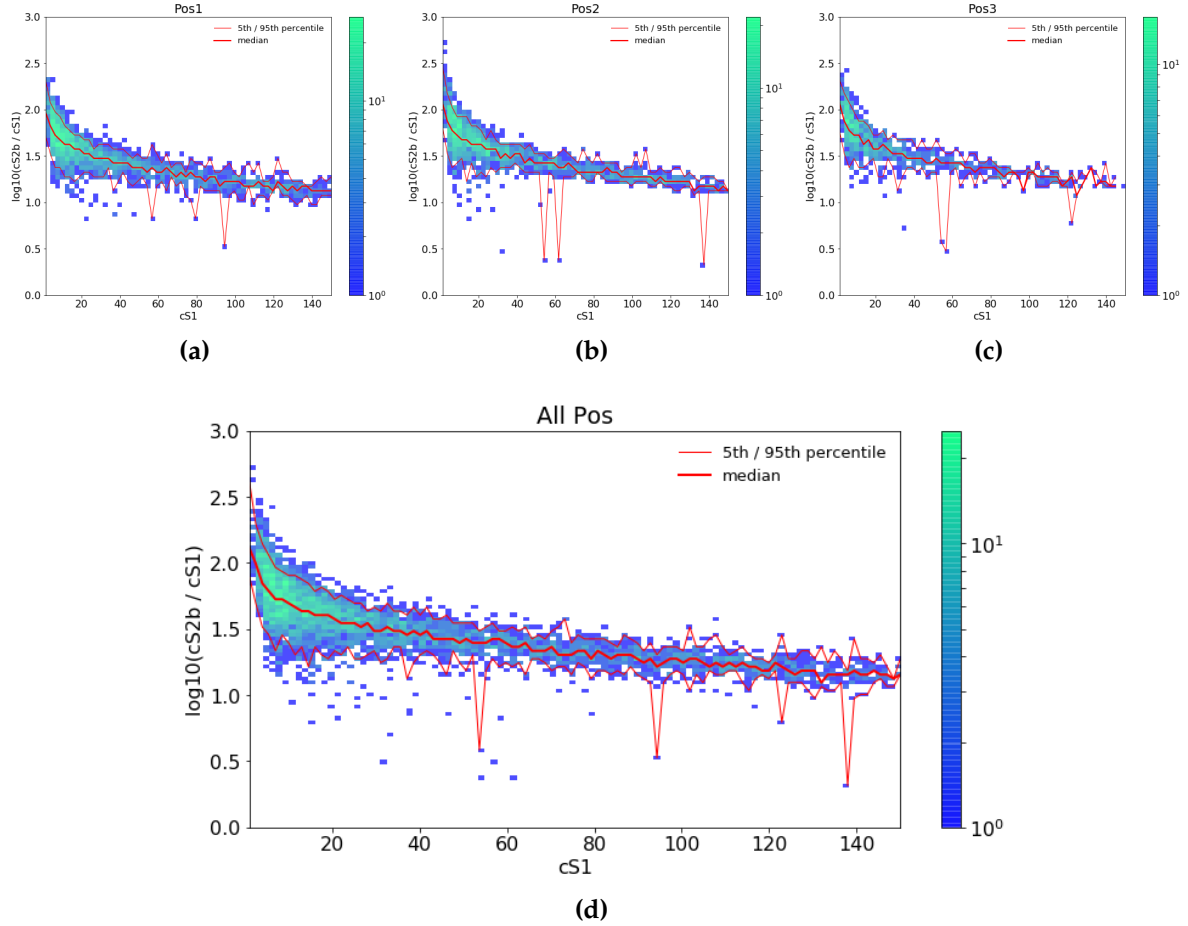


Figure 3.15.: Subfigures (a), (b) and (c) show the respective $cS2/cS1$ vs $cS1$ spectra overlaid with the calculated 5th and 95th percentiles and median. 60 bins from $cS1 = 1$ to $cS1 = 150$ are considered for these plots. Subfigure (d) shows the same quantities calculated for the summed dataset of all three positions. 100 bins from $cS1 = 1$ to $cS1 = 150$ are considered for this plot.

Table 3.15.: Parameters of the 5th, 50th and 95th percentiles fitted to the empirical function from Equation 3.4. The weight of all fit points is the same (no y uncertainty).

Fit parameter	5 th percentile	median	95 th percentile
a	0.58 ± 0.13	0.50 ± 0.02	0.77 ± 0.04
b	2.82 ± 1.22	8.21 ± 0.65	7.56 ± 0.79
c	1.35 ± 0.03	1.56 ± 0.01	1.72 ± 0.02
d	-0.0024 ± 0.0003	-0.0030 ± 0.0001	-0.0034 ± 0.0002

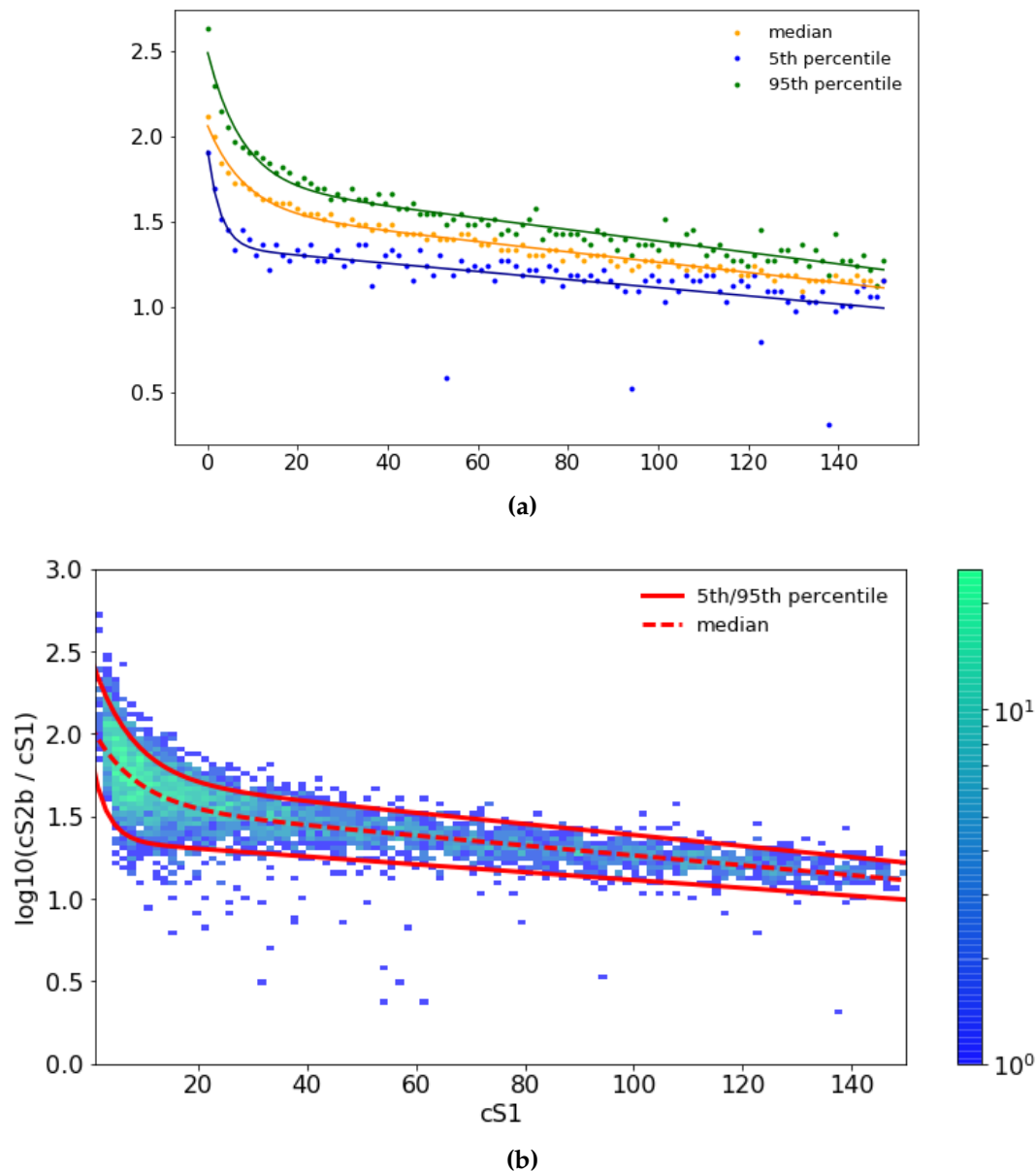


Figure 3.16.: Plots of the empirical function in equation 3.4 with the parameters in Table 3.15 for all three fits. In (a), the percentile points calculated in Figure 3.15d are shown with the fit function. In (b), the fitted function is plotted overlaying the data spectrum from Figure 3.14b.

The results shown in Table 3.15 and Figure 3.16 are the main objective of the present section. After further testing and consideration, the contribution of the remaining leakage events in the NR band fitting is negligible, even when their presence forces some 5th percentile bins to fall out of the main band. Like mentioned above, a more in depth study of these events, likely to be surface events from ²²²Rn in the PTFE walls, is of interest as they become background in the WIMP region of interest. On the main

analysis of XENON1T, leading up to a spin independent WIMP cross-section limit, surface background was deeply studied and modeled in order to be considered in the best-fit signal computation (Figure 4 in [38]).

Throughout XENON1T lifetime, during SR0 and SR1, many different NR calibrations and band fitting were done, similar to the one developed in this work. For each science run, the fitted band gets updated and corrected, hence a comparison of the different results obtained is worth studying. In Figure 3.17 a plot of the NR medians obtained during SR0 (just AmBe data), SR1 (AmBe and NG data) and pos-SR1 (just NG data, this work) is shown. Although different, as expected, the results are compatible within a 5% difference up to a $cs1$ value of 140 pe for SR0 and over 150 pe for SR1 results. Moreover, this result stands below 3% relative difference with the SR1 results up to a $cs1$ value of 130 pe.

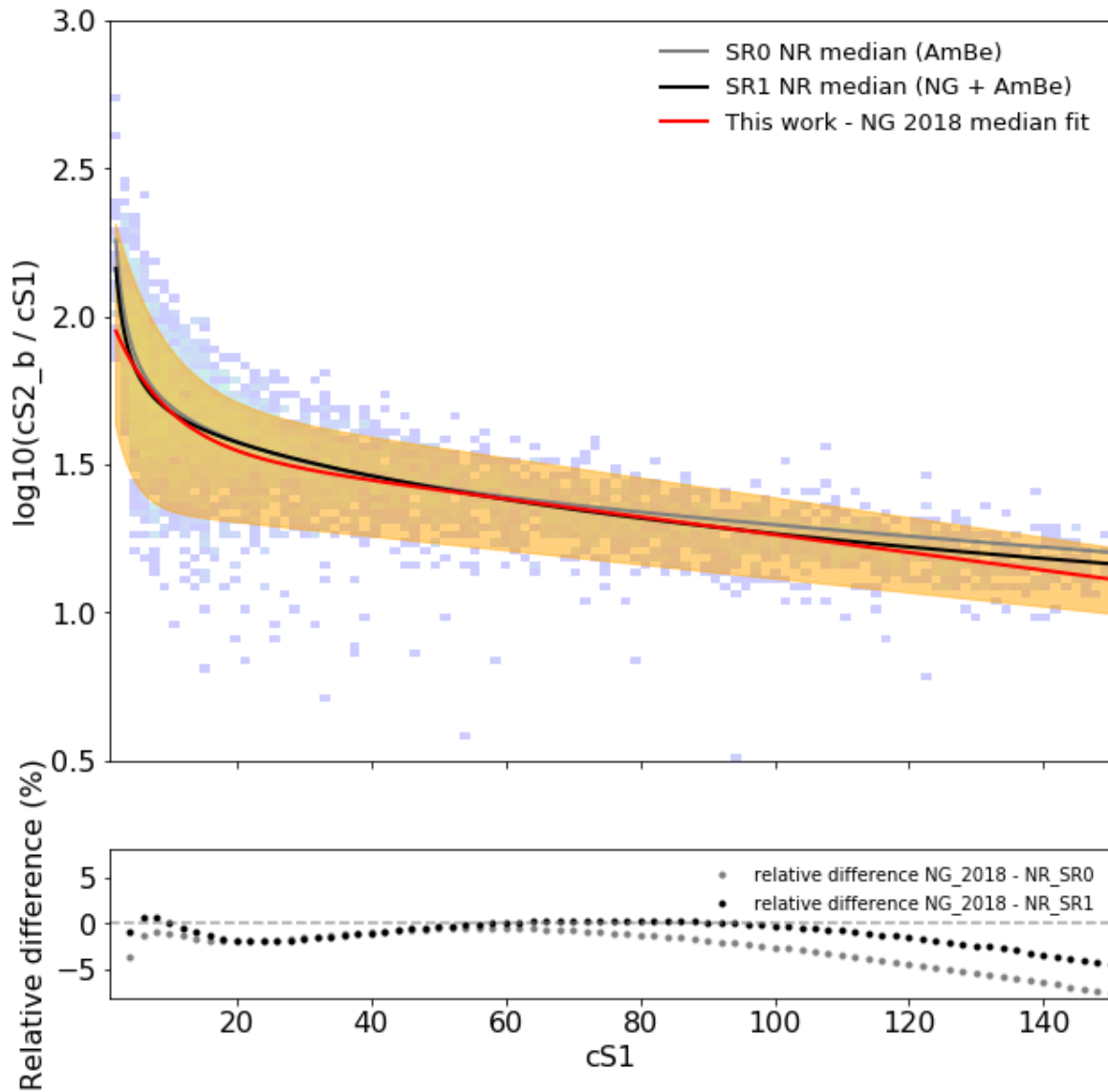


Figure 3.17.: On the upper part, a comparison between SR0, SR1 [92] and post-SR1 NR medians in $cs2/cs1$ vs $cs1$ space, overlaying the computed NR band (Figure 3.16b) and the distribution of events used to its calculation. The relative difference between both SR0 and SR1 results, respectively, is shown in the lower axis (more in text)

Chapter 4.

Electric field simulations for XENONnT

“You will be upgraded!”

— Mondasian cyberman, aboard a Mondasian colonizing ship in the verge of a black hole horizon, unknown date

For more than a decade, the direct search of dark matter has not yet succeeded on claiming a discovery. The efforts are many and come from various reputable international collaborations that keep improving the effectiveness of their search and the constrains of WIMP's cross-section in their results. Particularly, from XENON10 to XENON1T not only the mass of the active target increased, but also the technology and analysis techniques employed are more capable and efficient. XENONnT is the next step for DM search and the most advanced detector within the XENON family. Using most parts of the infrastructure of XENON1T, it is planned to be of rapid and cost-effective commissioning. In this chapter, the XENONnT detector is introduced in Section 4.1, alongside the main changes in each subsystem from XENON1T. In Section 4.2 the underwent studies on electrostatic field finite element simulations are presented with the goal to optimize the field shaping rings (FSR) of the field cage just outside the TPC PTFE walls.

4.1. Upgrading the search equipment

During XENON1T designing phase, a call was made to build its infrastructures capable of withstanding a new inner detector, much larger than the first, using the same water shield, buildings and major systems. In this paradigm, the upgrade of the system as a whole becomes much more quick and cost-effective than would be expected for a multi-tonne facility. The most noticeable upgrade is in the volume of target mass, going from 3.2 t (2 t) to 8 t (6 t) total mass (active mass), but it is not the only one.

Despite the lack of a discovery claim, liquid xenon time projection chambers seem to be the best technology to probe the last remaining expected parameter space for massive WIMPS, proven by the rapid success and always more stringent limits of the different experiments who pursue it. The reasons behind the use of LXe and how a LXe double-phase TPC functions were already covered in Chapter 2: 3D reconstruction of events, self-shielding, scalability of an homogeneous target. For bigger, tonne-scale detectors even neutrons are distinguishable from a WIMP-like signal from their multiplicity.

4.1.1. Physics reach

XENONnT, expected to start its first operation run mid-2019, given its high sensitivity, has a high chance to be the first DM experiment to detect coherent neutrino-nucleous scattering, expected as a nuclear-recoil interaction. However, this potential background only proves significant for very low WIMP masses and does not deter XENONnT to explore the most relevant WIMP-mass range. More than itself a rewarding achievement, it foresees the new physics reach of LXe TPCs, with lower background rate than ever.

The dominant background comes from ^{85}Kr and ^{222}Rn as internal sources. For the required level of background of XENONnT, both contaminations must become ten times smaller than in XENON1T, reach levels of $1\ \mu\text{Bq}/\text{kg}$ of ^{222}Rn and 0.02 ppt of $^{\text{nat}}\text{Kr}/\text{Xe}$ [93]. Techniques aimed at accomplishing these levels are already planned and further detailed below in 4.1.3.

With such a sensitive detector, different physics channels besides SI WIMP-nucleon cross-section become of interest. Other rare events searches, namely neutrino-less

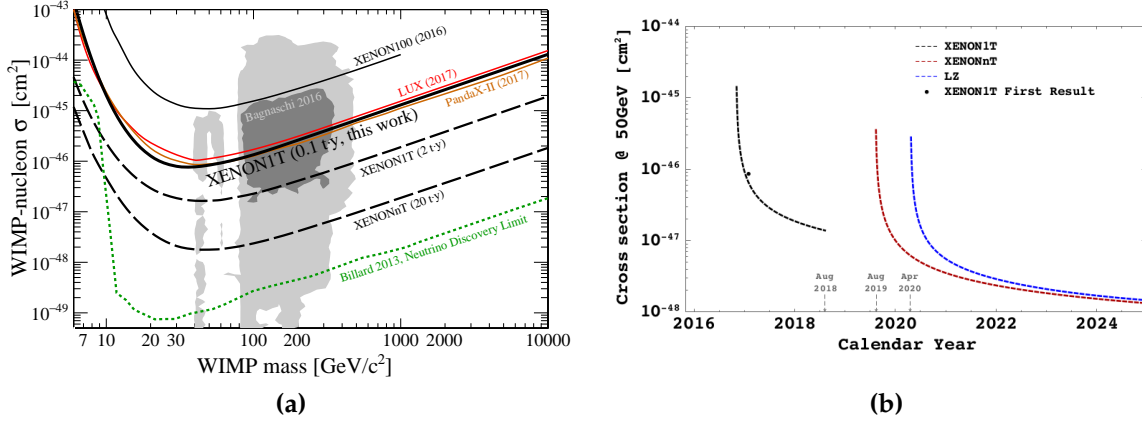


Figure 4.1.: (a) Expected sensitivity of XENONnT for spin-independent WIMP-nucleon interaction cross-section as function of WIMP mass (a) and calendar year, for a 50 GeV/c² WIMP (b). Figures from [94] with data from [62] and [95]

double beta decay, double electron capture and solar neutrino detection are expected to have increased interest in the analysis of XENONnT data.

4.1.2. TPC and cryostat

The major change from XENON1T to XENONnT is the size of the TPC in height and diameter, increasing both the drift length of electron clouds and, on a analysis perspective, the fiducial volume and therefore sensitivity on any physics search. The outer vessel is the same of XENON1T, designed to handle the upgrade without need for any change, while the inner vessel is augmented in order to hold a total xenon mass of 8 t. The TPC is set to measure 1.62 m height and 1.46 m diameter, a similar size ratio to XENON1T.

Light signals will be collected by 467 R11410-21 Hamamatsu 3" photomultipliers, the same model as in the last iteration, divided between top (223) and bottom (253) arrays, from which 260 units come from the previous detector, where 90% of PMT worked without problems. The design of the PMT arrays resembles the one used in XENON1T as it proved successful for position and energy reconstruction of events: bottom array in a hexagonal pattern, maximizing the number of PMTs and top array in a circular pattern, maximizing the area covered and the number of PMTs near the outer edge.

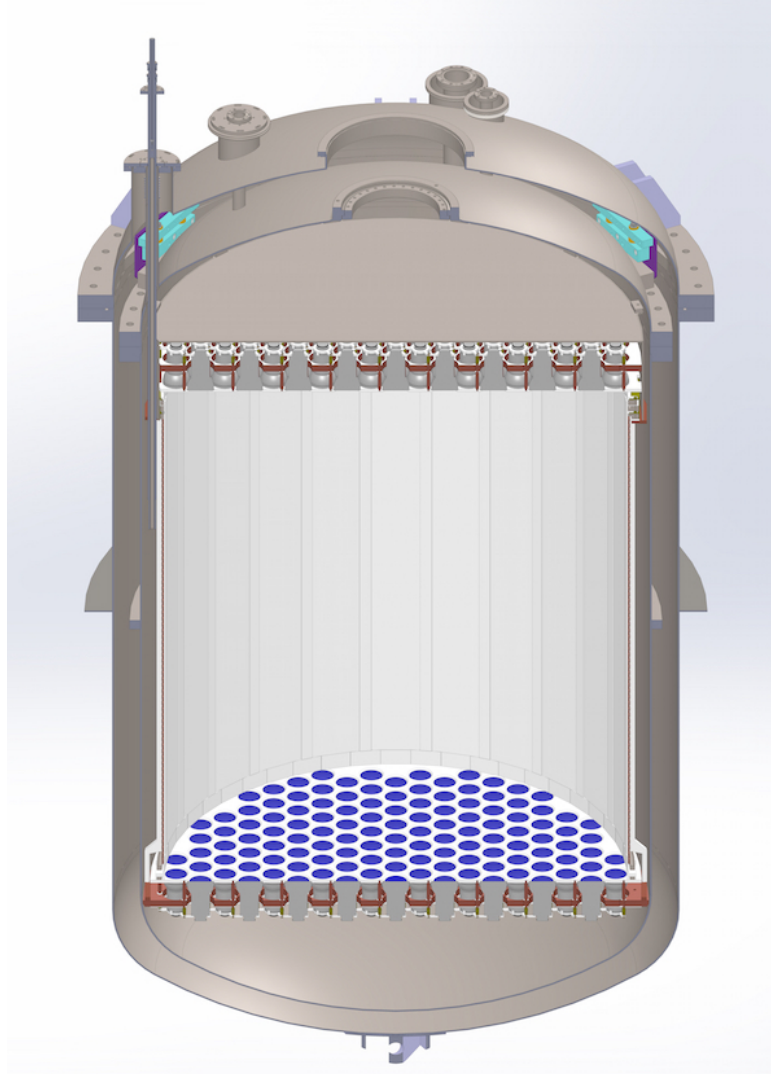


Figure 4.2.: Drawing of the XENONnT detector TPC. Model by Prof. Luca Grandi, LNGS-INFN.

The drift region is limited between the cathode grid and the gate mesh, both from built with stainless steel (SS) wires with $200\ \mu\text{m}$ and $100\ \mu\text{m}$ diameter, respectively. The extraction region, where electrons are extracted from the liquid phase to the gas phase is set between the gate mesh and the anode grid (also both $200\ \mu\text{m}$ SS wires), $5\ \text{mm}$ apart from each other with the liquid-gas interface at the middle point. Between the anode and the grounded mesh a voltage of $+5\ \text{kV}$ is imposed in order to guarantee full electron extraction. As for the drift electric field, a value of $200\ \text{V/cm}$ is set by the cathode electrode at $-30\ \text{kV}$.

Laterally, the active volume is defined by the PTFE wall, made from interlocked panels to form a $1330\ \text{mm}$ diameter 24-gon polygon resembling a perfect cylinder.

On the outside of the PTFE walls, a series of copper rings, connected through tuned resistors, make a resistor chain in order to shape the electric field inside the detector, aiming for an uniform vertical electric field in the drift region. A study on the geometry options for the field cage is conducted in Section 4.2.2.

As of the writing of this work, the TPC, cryostat, electrodes and most of the components of XENONnT are constantly being updated from on-going studies carried out by various groups within the XENON Collaboration and may, therefore, change until the final detector design.

4.1.3. Purification and storage

Due to the large volume of LXe in XENONnT, the time it takes to remove impurities and reach the desired levels of purity would be too large if no upgrades to the equipment were taken into account. Therefore, two major changes in the purification systems will take place: higher gas flow with proper circulation pumps and pipes and the installation of a liquid purification system, alongside the current gas one.

One of the main Radon background sources in XENON1T are the QDrive pumps, responsible for the gas circulation through the system (see Figure 2.12b). For the new detector, new magnetic pumps, based on the design used in the EXO-200 experiment [96] are being installed and tested, leading to very promising results in both pressure flow, purification speed and radon purity. Other methods for Radon reduction are also scheduled to be employed based on the experience acquired with the XENON1T detector, such as careful selection, cleaning and handling of every component of the cryostat and TPC until the final sealing, online distillation through a distillation column and liquid based cryogenic distillation system. The liquid purification system, more than the afore mentioned distillation phase, also features two custom-made redundant filters to handle the electronegative impurities of the medium.

Yet another upgrade will target the storage and circulation of Xenon in the detector with the addition of ReStoX2, the *big brother* of ReStoX, proven to work very well during XENON1T operation. With the remarkable capacity of 10 t, ReStoX2 will complement the existing storage vessel, capable of keeping the whole xenon inventory safe even in room temperature. Moreover, with the intended design of the overall cryogenic system, which connects purification, ReStoX, ReStoX2 and cryostat, circulation of

LXe through the distillation columns can overpass the cryostat and go back and forth through ReStoX and ReStoX2. Due to this capacity, purification of the whole xenon inventory may start much sooner than when commissioning of the cryostat and TPC end.

4.1.4. Calibration

Most of the calibration system will be re-used from XENON1T. For nuclear recoil calibration a deuterium-deuterium neutron generator and an AmBe source will be used. Detector uniformity and energy calibration is provided by $^{83\text{m}}\text{Kr}$ and electronic recoil calibration by a ^{220}Rn source. Moreover, more types of calibrations and sources are being studied as potential additions. On one hand, for low energy NR, the implementation of YBe and, on the hand, ^{37}Ar for very low energy ER and energy scale. In order to probe the fiducialization limit, external ER calibration are also being considered with low activity ^{137}Cs and ^{228}Th sources. As an upgraded to the current NG, a LUX-like setup is being developed, making use of a pulsed DD-NG with an air sealed collimator up to the cryostat wall. This setup allows for a significant reduction of backgrounds and systematics during NR calibration as well as double scatters to be used as energy calibration [57], without increased safety concerns.

4.1.5. DAQ and computing

The major difference in the DAQ system will be the extra channels needed for the new PMTs. These will be integrated in the current system, making use of the already in use voltage suppliers and amplifiers. The machine running the trigger and event builder machines will also get properly updated to handle the large amount of data expected from XENONnT. This large amount of data, reaching 1300 TB/year in some scenarios, requires new transferring, processing and storage tools and protocols. As an extended effort, a integrated system from raw data to analysis-friendly data, through proper transferring and processing, is being developed by the computing team in the Collaboration. The *younger sibling* of PAX will make analyzing the data from XENONnT a much more easy task on the analyst, specially for *thinking outside of the box* type of campaigns, where non-trivial quantities from events are looked at and that, up to this point, would require massive reprocessing of data.

4.2. Electric field simulations of the TPC and field shaping rings optimization

Electrostatic field simulations are an important step for choosing the design of such a large detector as XENONnT. At first sight, the concept of the double-phase TPC is straightforward (see Chapter 2), with well defined electric fields controlled by the main electrodes (cathode, gate and anode). However, every little detail counts and, in reality, getting a perfectly uniform field between anode and cathode with zero charge loss and easy to infer drift time is an utopian goal. Even in concept, only with infinite area electrodes the field would be perfectly uniform everywhere in the detector drift and extraction region. Through simulation, one can study the effect of every component of the detector, as well as optimize the electrodes, both geometry and voltage wise, to give the desired shape and magnitude to the electric fields therein. [97]

The simulations are computed using COMSOL Multiphysics[®] [98], based on finite element algorithms applied throughout a mesh optimized for the model geometry. Both 2D and 3D simulations can be performed. In this work, a 2D axial-symmetric model of the XENONnT TPC is developed in order to study the electric field inside it. Focusing on optimizing the uniformity of the field, a study of different Field Shaping Rings (FSR) geometries and voltages is conducted.

4.2.1. Geometry model of the XENONnT TPC

The COMSOL geometry and material model closely follows the designed detector, in order to accurately describe it. Two types of models were developed: 2D axial-symmetric, where a profile slice of the cylindrical detector is modeled and the behavior of the system is supposed phi non-dependent, and a full 3D simulation. Due to the available computational resources, for the study of the electric field here at end, only a 2D axial-symmetric simulation was performed.

82 4.2. Electric field simulations of the TPC and field shaping rings optimization

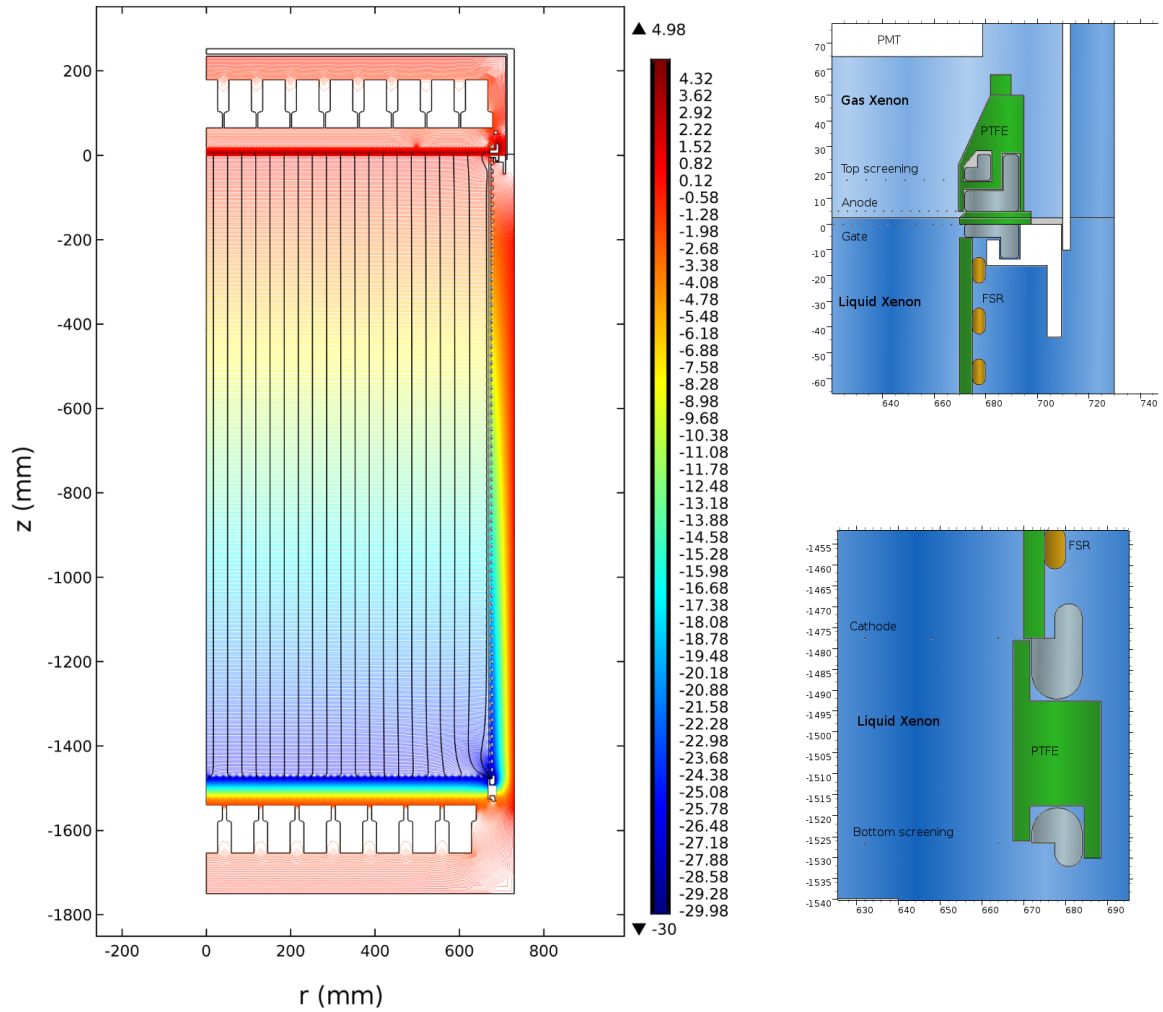


Figure 4.3.: Geometry of the XENONnT TPC. color map in kV. On the left side, the overall geometry with the voltages presented on Table 4.1 is shown. The FSRs follow the geometry and configuration of the XENON1T model. On the right side of the figure, the top and bottom electrodes geometry are shown in detail with the following color map: light and dark blue for gaseous and liquid Xenon, green for PTFE, silver for the stainless steel electrodes and in brown the copper FSRs. In white are shown the PMTs and support structures.

In a first iteration of the XENONnT geometry, it stands as an extension of the XENON1T geometry, both radially and height wise. Furthermore, the projected drift field is of around 200 V/cm, which, given the 1.5 m drift length, sets the cathode voltage to -30 kV. The extraction region and field stay the same, changing the ground mesh from a solid perforated plane to parallel wires, following the design of the other electrodes due to its size (1.5 m diameter).

Table 4.1.: Geometries and voltages of the electrodes of the XENONnT TPC model.

Electrode	Voltage (kV)	Wire diameter (μm)	Spacing mm)
Top screening	-1.5	200	5
Anode	+5	200	5
Gate	0	100	5
Cathode	-30	200	7.5
Bottom screening	-2.5	200	7.5

Table 4.2.: Distances between electrodes of the XENONnT TPC model. The distances between the top screening mesh and the anode, the gate and the cathode and the cathode and the bottom screening mesh must yet be multiplied by the shrinkage fraction of the PTFE (1.5%)

Electrodes	Distance (mm)
Top PMT to Top Screening mesh	48
Top screening mesh to anode	12.18
Anode to gate	5
Gate to cathode	1500
Cathode to bottom screening	49.7

4.2.2. Study of field shaping rings

To keep the field as uniform and vertical as possible, a field cage stands just outside the PTFE walls. In XENON1T, this field cage was composed of 74 horizontal copper rings with 10 mm height, 5 mm width and spaced by 10 mm from each other. The voltage of each FSR is given by:

$$V_i = V_{i-1} + \frac{V_{gate} - V_{cathode}}{N_{FSR}} \quad (4.1)$$

84 4.2. Electric field simulations of the TPC and field shaping rings optimization

where V_i is the voltage of the i shaping rings (number 1 near the cathode, number 74 near the gate), V_{gate} and $V_{cathode}$ are the voltages of the gate and cathode electrodes, respectively, and N_{FSR} is the total number of shaping rings. The voltages of each FSR are set by a resistive chain connecting all 74 copper rings. Fine tuning of the first and last few rings voltage may be done to counteract effects near the corners of the TPC that can impact the whole volume [99] (see Figure 4.4 and Figure 4.5).

For XENONnT, as afore mentioned, the first iteration consists of expanding the TPC width and height wise. As for the FSRs, they remained as a ring shape (10 mm height, 5 mm width) but adjacent (touching) to the PTFE wall.

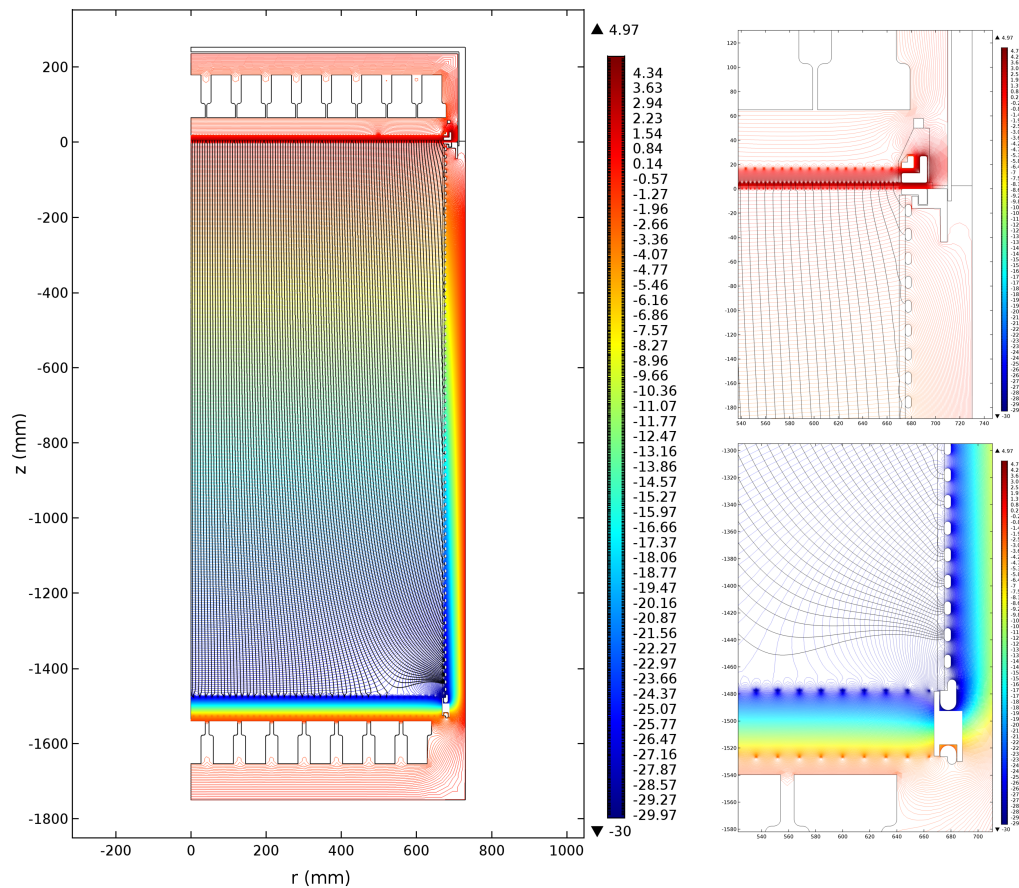


Figure 4.4.: Simulated electric field of the XENONnT detector using FSRs similar to the ones from the XENON1T detector, before fine tuning. The figure is divided in three parts: left – whole TPC; top right – top part of the TPC, near electrodes; bottom right – bottom part of the TPC, near electrodes.

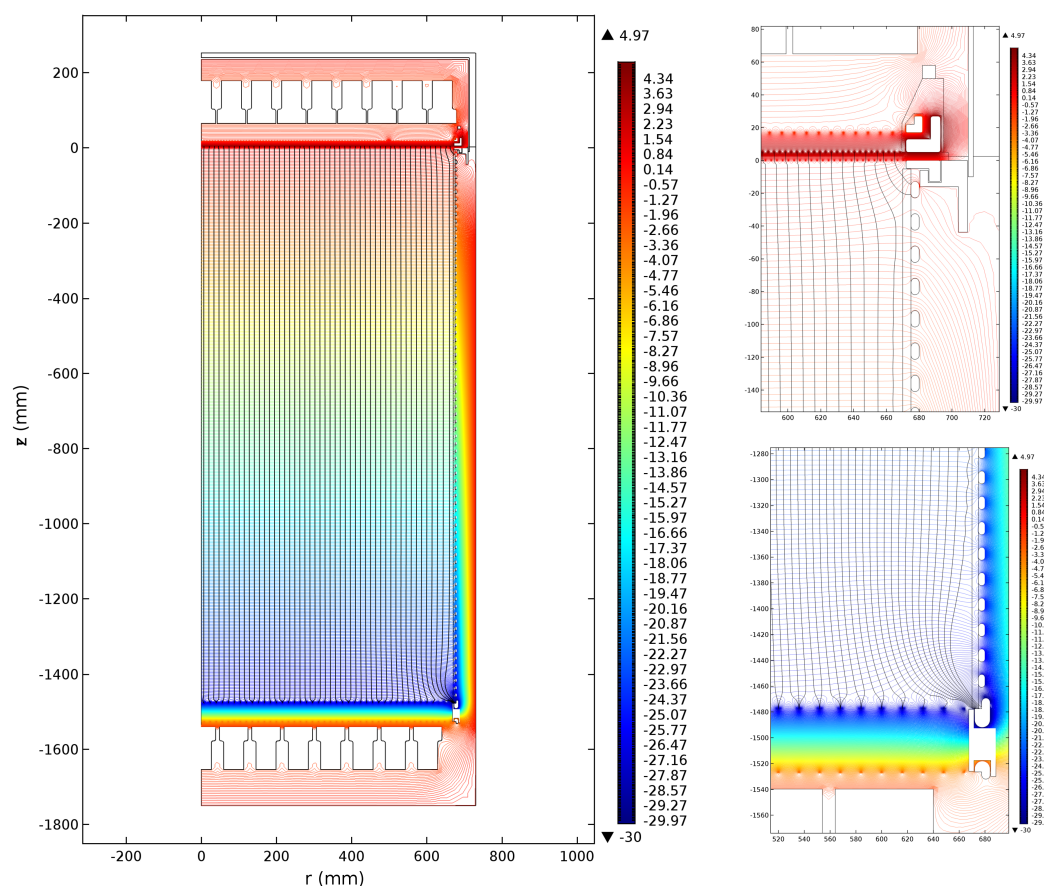


Figure 4.5.: Simulated electric field of the XENONnT detector using FSRs similar to the ones from the XENON1T detector, after fine tuning.

The main objectives when optimizing the FSRs geometry and voltages are:

- Shape the electric field inside the TPC as close to as uniform as possible, especially inside the fiducial volume;
- Prevent charge loss in the PTFE walls, expected when field streamlines cross the wall border.

The last appointed item is the main improvement to be handled for XENONnT as during XENON1T operation charge loss was a major inconvenience. When an electron cloud drifts near the wall, some electrons may get stuck in the PTFE, which is an isolator material. Due to this charge lost, the S2 signal of the given interaction is much smaller than expected - or even absent - leading to a miss-classified, lone S1 or *leakage event* (bellow the respective band). This later is of extreme importance because, in an extreme case, an ER event might be tagged as inside the NR band and, if reconstructed inwards, within the fiducial volume, rising as a potential false-positive for a WIMP-like

86 4.2. Electric field simulations of the TPC and field shaping rings optimization

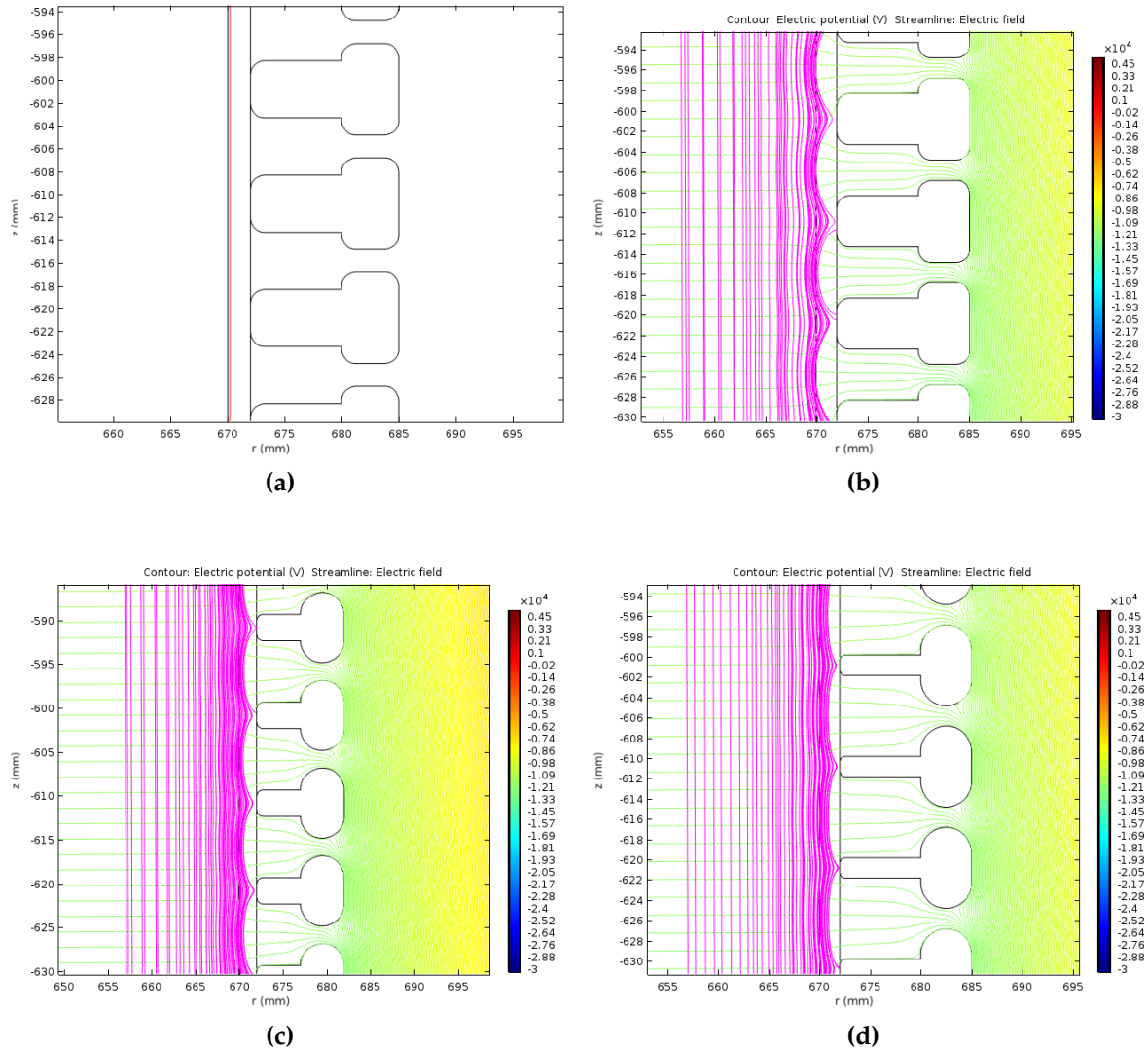


Figure 4.6.: Different FSR T-shape geometries simulations: **(a)** Geometry of a T-shape FSR. The height and width of the bulk part stays at 10mm height, 5mm width. The red line, placed 0.2 mm inside the PTFE, is the cut line through which every streamline that crosses it, gets plotted, adding to the one inside the TPC; **(b)** Nose geometry: 5 mm height, 8 mm width; **(c)** Nose geometry: 3 mm height, 3 mm width; **(d)** Nose geometry: 2 mm height, 8 mm width;

event. These events were deeply studied and modeled during XENON1T analysis, leading to the automatic classification of some events in the ROI during unblinding as *wall* events (see Figure 3.8 and reference [38]).

The first step to look into preventing charge loss was making the FSRs touch the PTFE walls, ala XENON100. Although promising, the results were not yet satisfactory because the field still remained very *wavy* near the wall. To reduce the contact of the

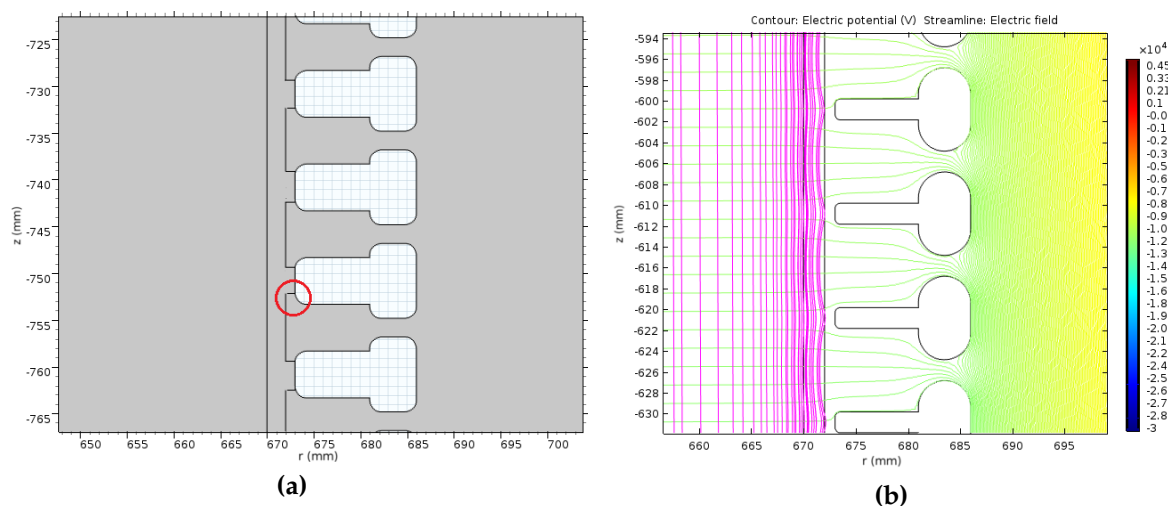


Figure 4.7.: Different FSR T-shape geometries with bump simulations: **(a)** Geometry of a T-shape FSR touching the PTFE bumps. The height and width of the bulk part stays at 10mmx5mm; **(b)** Nose geometry: 2 mm height, 8 mm width. The 1 mm width PTFE piece between the main wall and the FSR is not rendered for simplicity.

rings to the PTFE, while keeping contact, a T-shape geometry was designed, adding two parameters to the table: the *nose* width (measured in r) and height (measured in z). The results of several geometry attempts are shown in Figure 4.6. A case was also made for rings touching *bumps* on the PTFE instead of the main wall but it was shortly discontinued as it did not improve significantly the uniformity near the wall while having its own charge build up problems on the outside of the wall (red circle in Figure 4.7a).

From Figure 4.6 and Figure 4.7, one can reach some useful conclusions by a qualitative approach:

- Streamlines behave better (waves dissipate faster) when the height of the *nose* decreases (gets thinner);
- Streamlines behave better when the width of the *nose* increases (gets longer);
- Distancing the FSR from the main PTFE (with a piece in between) gets better results but might cause charge accumulation between extended PTFE piece and main wall.

With these points in mind, three different geometries were chosen for a qualitative comparison: simple 1T-like ring, long T-shape (15mmx3mm) and small yet in more

88 4.2. Electric field simulations of the TPC and field shaping rings optimization

number T-shape (5mmx3mm). The added parameter of “number of FSRs”, although not studied in this work before, is expected to improve the behavior of the field from the results of other studies [100].

Table 4.3.: Details of the most representative FSRs models studied: 1T-like simple ring, T-shaped with a *long nose* and T-shaped with smaller body and more rings.

Shape	number of FSRs	Height (mm)	Width (mm)	Spacing (mm)	Nose height	Nose width
simple ring	74	10	5	20	-	-
long T	74	10	5	20	3	15
small T	145	8	5	10	3	5

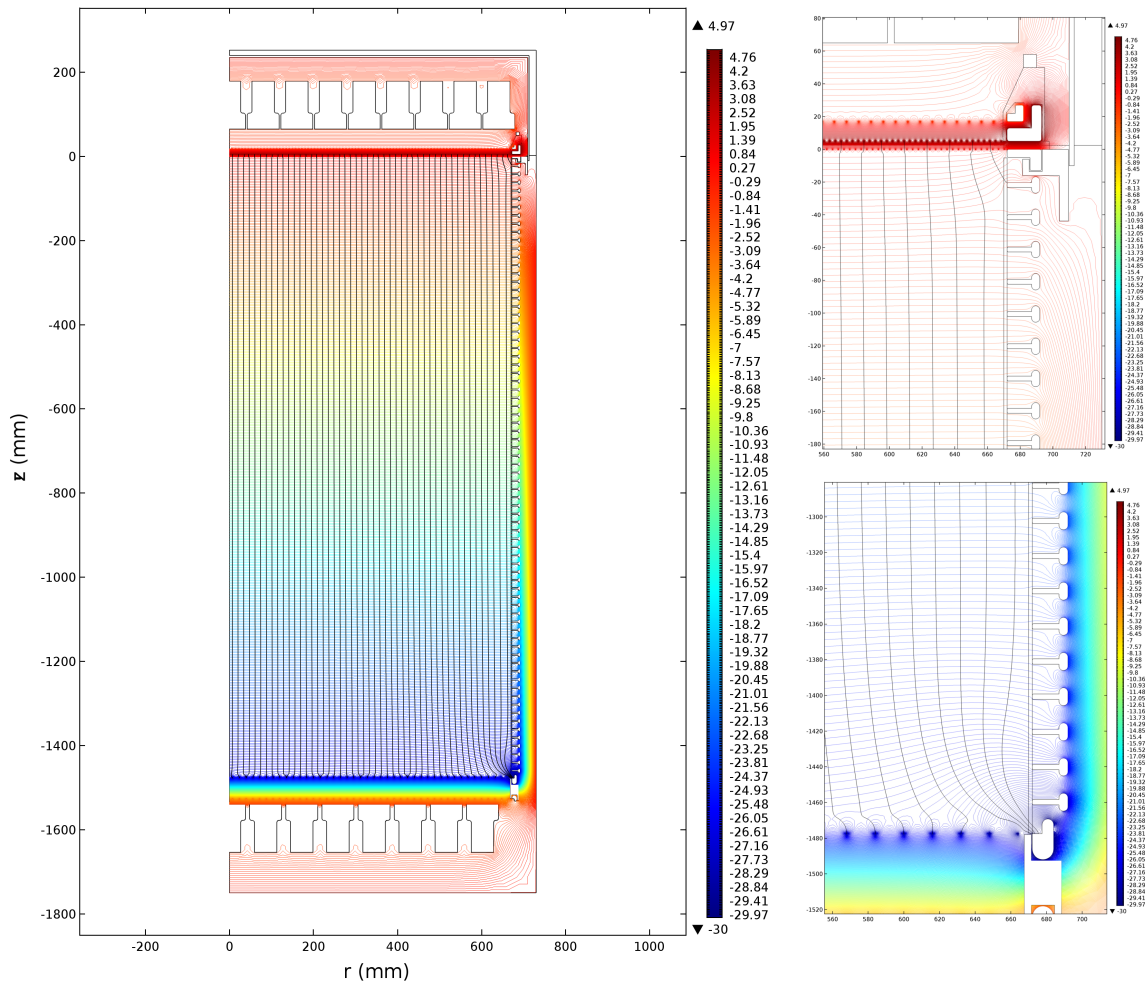


Figure 4.8.: Simulated electric field of the XENONnT detector using 74 T-shape FSRs with a *long nose*.

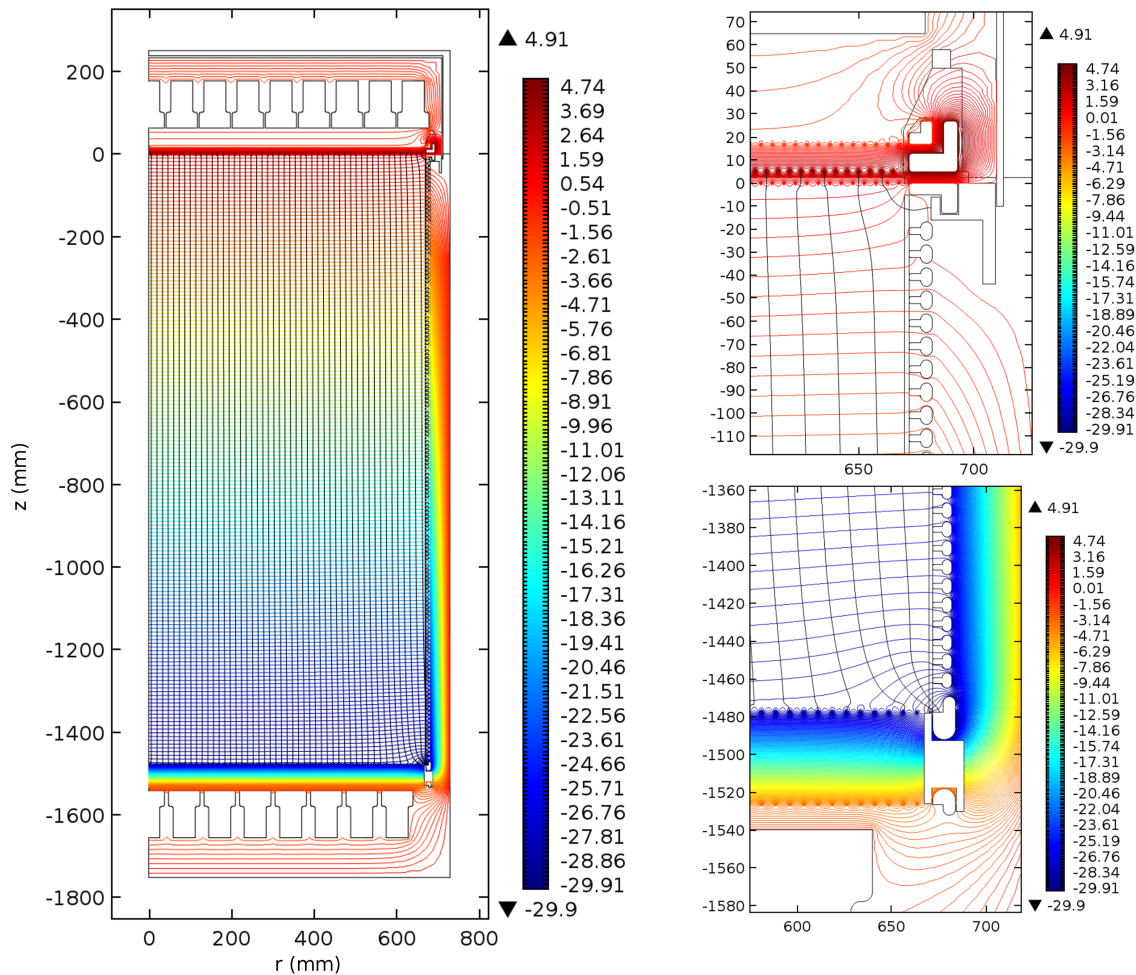


Figure 4.9.: Simulated electric field of the XENONnT detector using 145 small T-shape FSRs.

In order to quantify the improvements of each model, the angle of the electric field in respect to the vertical position (z parallel) is plotted as function of the radius of the TPC. Larger angles are expected near the wall. How large can give an indication of how good a model behaves: no wave-like behavior leads to no big angles found.

From Figure 4.10, the improvements from simple 1T-like rings to T-shaped ones are undeniable. In all three cases the result is similar for z dependence: near the gate (z close to zero) the field is uniform until larger radii and gets progressively worse near the cathode (z close to -1500 mm). Figure 4.10b indicates that a T-shape has smaller wave-like pattern close to the walls of the TPC than the simple 1T FSR (Figure 4.10a).

Given the small angle values it reaches and the larger radius it needs to start having large discrepancies, the small T-shape FSR seem the best of the three, proving that the

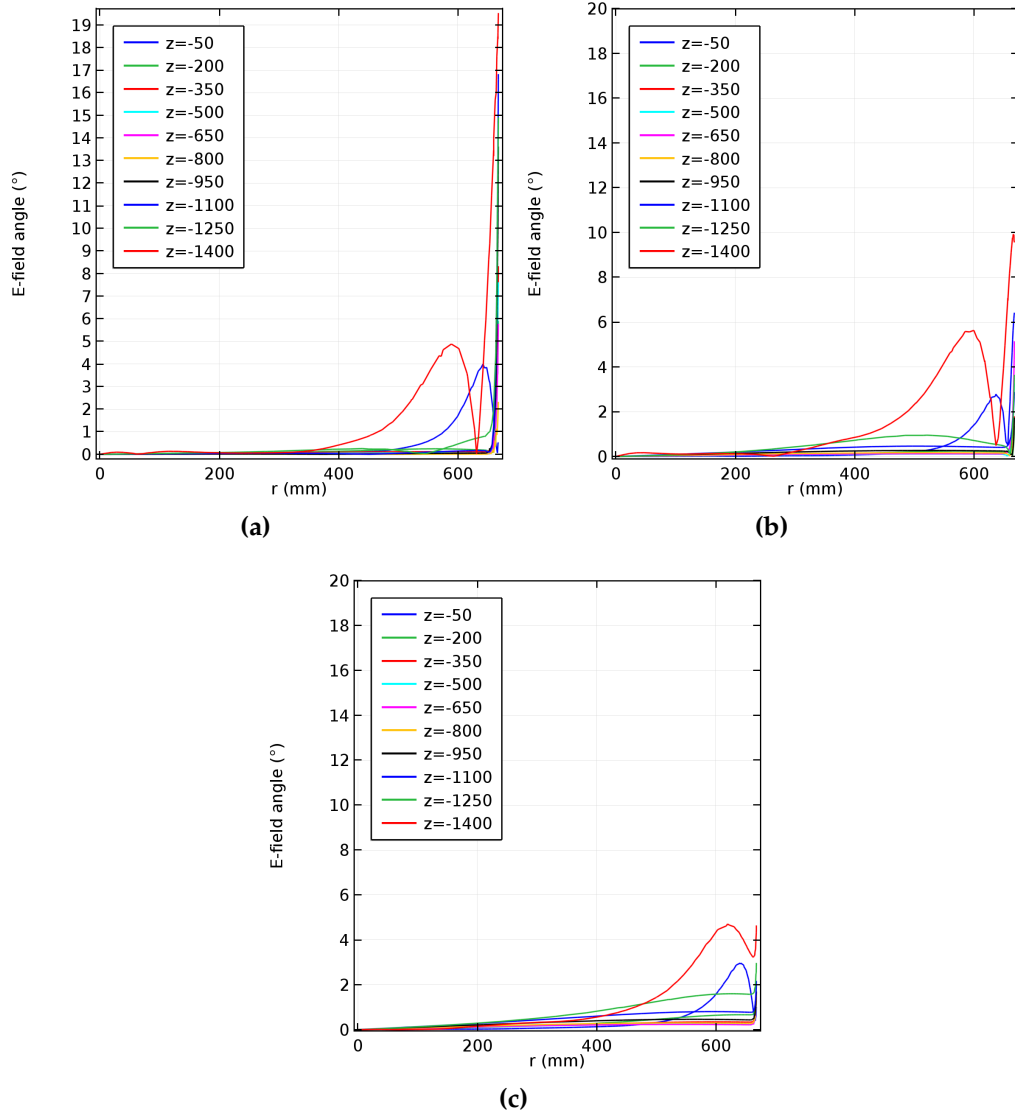


Figure 4.10.: Plots of the angle of the electric field inside the TPC (up to 2 mm to the PTFE wall) in relation with the vertical (z direction) versus the radius. Different colors represent different z positions of the study, as labeled in the top left corner of each plot. Discussion on text.

amount of shaping rings (and their spacing), is an important parameter contributing to field uniformity.

As a concluding remark, one has to look at the study done in this work as only a developing step into the optimization of the FSRs geometry. Neither it is or tries to be a final design. Like every aspect of the XENONnT detector, the TPC and all its electrodes design is a collaborative effort from the XENON collaboration and therefore,

even a not polished and finished study like the one presented here is important, as others can (and will) learn and improve from it.

Chapter 5.

Final Remarks

5.1. Conclusion

The latest detector from the XENON Collaboration has once again proven the capabilities of double-phase TPCs in the search for Spin-Independent WIMP-nucleon interaction with the first multi-tonne target mass liquid Xenon DM detector, XENON1T. The challenges associated with this endeavor have been systematically overcome reaching the rank of most sensitive DM detector at the time of writing this dissertation.

In this dissertation, two major topics of the XENON detectors were studied: simulation and analysis of the XENON1T detector response to nuclear recoils calibration sources and electric field optimization of the XENONnT detector. Chapter 1 and Chapter 2 cover the basics of direct Dark Matter detection, detection principle and processes in a double-phase TPC, as well as an outlook of the XENON1T detector.

The third chapter describes the contributions made during the last year on simulation and analysis of a neutron generator calibration run of the XENON1T detector. A *Geant4* simulation was produced and its results presented and discussed here range from pure statistics, on Table 3.1, to a study of the energy spectrum of the emitted neutrons when reaching the TPC, on Figure 3.6 and text. The broadening and low energy neutrons observed are correlated with moderation between the source and the detector, as well as the γ peaks to known reactions in the detector materials.

Alongside the previous simulation, a full-chain simulation was conducted, mimicking the output of the real detector in order to test PAX and easily compare real data with simulated data. The discrepancies shown in Table 3.3 are due to an excess of

high energy and spurious events present in real data when comparing to simulation, expected to come from gas events, accidental coincidence events and/or flashes. A study was conducted on several analysis cuts, their efficiency and how they behave on real versus simulated data, presented in Tables 3.4 to 3.11 where, the overall behavior agrees between real and simulated data. This method proves to be a quick and efficient way to check if the analysis cuts behave properly in both simulated and real data and was of great importance during the development phase of analysis.

Finally, in Section 3.3.3, the datasets from the 2018 NG calibration runs of the XENON1T detector are used to model an empirical NR band. All the analysis cuts of SR1 were employed to select the proper events for the fit, shown in Table 3.13. The distance to the neutron source was also taken into account, aiming to decrease the number of leakage events of the NR band (Figure 3.13 and Figure 3.14). The result on the fitting of the NR band to the empirical model (equation 3.4) is presented and compared to previous band models in Figure 3.17 and discussed. Overall, the different results match up to a $cS1$ value of 80 photoelectrons and stay up to 5% of each other up to 130 photoelectrons.

In Chapter 4, the subject changes to the next generation multi-tonne detector, XENONnT. Planned to start operation during 2019, it will use most of the infrastructure of the XENON1T detector, expanding the TPC and inner cryostat, as described in Section 4.1. The goal was set on testing and optimizing the geometry and voltage distribution of the resistive chain responsible for the uniformity of the field inside the TPC. Different geometries were computed using finite-element simulations in the COMSOL Multiphysics software package and the results obtained are shown in Section 4.2. The oval-like geometry of the XENON1T FSR was surpassed by a T-shape FSR with the tip touching the PTFE wall. Different sizes of the *nose* of the FSR were simulated, leading to the conclusion that a thinner and longer *nose* gives much better results in terms of uniformity of the field. Furthermore, smaller and tightly spaced FSR given even better results (Figure 4.10). The conclusions reached in this work, are of great relevance to the on-going studies leading to a final decision by the XENON Collaboration on the field cage design and properties.

5.2. Future work

Both major topics covered in this dissertation have room for improvement and deeper studies. Note that any future work can be related to the re-analysis of XENON1T data but should mostly look forward to any improvements to be added to the XENONnT detector.

As for the first subject, following the results from LUX [57,101] a very low energy NR calibration using a NG should prove an important study of the detector response and provide much stronger input for low energy searches. To make this possible operation wise a new NG with the possibility of pulsed emission must be acquired and a collimator, from the neutron source up to the cryostat, designed. Then, single and multiple scatter selection of events will become much more efficient, leading to stronger discrimination quality.

Regarding the FSR optimization, the conclusions reached here are just part of a collaborative process leading to the final design. Improvements should be easily achieved if a design where smaller T-shape rings touch the PTFE. Another important subject is the uniformity of the field dependence on the field magnitude, in other words, on cathode voltage. During XENON1T operation, the detector was operated at lower cathode voltage than the one designed. This change did not stop data taking but might have increased the problems with wall events. From simulations, when the cathode voltage changes, the FSRs need a new fine tuning, which implies changing the first and last couple resistors of the chain. A system of variable resistivity on those resistors could be considered for tuning the resistive chain during operation.



Figure 5.1.: The XENON collaboration. Coimbra, 06/09/2018.

Appendix A.

Simulation and Analysis environment

This appendix aims to give an overview on the simulation and analysis environment and steps taken for the results shown in Chapter 3.

Within the XENON Collaboration, a vast set of analysis tools and procedures is shared between everyone to work with and apply to their own research topic. This is the case of the Geant4 model of the XENON1T detector and most of the analysis tools, including standard event selection cuts.

A.1. Simulation framework

There are several stages in Monte Carlo production:

- **Geant4 MC** – a Geant4 geometry, material and physics model is loaded and the simulation computed.
- **nSort** – a python script takes the Geant4 output, adds experimental uncertainty (detector energy resolution) and converts deposited energy into S1 and S2 signals. For details about the conversion the reader is pointed to reference [64].
- **FAX** – The FAke Xenon experiment is a waveform simulator for Xenon TPCs. FAX simulates the real detector in the sense that it determines the production times of photons from drift, S1 and S2 signals, decides which PMTs see the photons (using a Light Collection Efficiency map) and the resulting PMT hitpattern and simulates the PMTs response to the photons and the digitizers response to the PMT signals. In the end, FAX outputs a PAX event raw data file.

- **PAX** – The Processor for Analyzing Xenon is the main processor for the events registered in the detector. From the output of FAX this same processor can be used for simulation, mimicking not only the hardware but also the software response of the real experiment.
- **HAX** – The Handy Analysis tools for XENON package equips the XENON analyst with tools for common analysis tasks on PAX processed data, such as the creation of Pandas DataFrames with reduced data (*minitrees*) from the PAX ROOT files, select and load datasets of a particular source or reference from the XENON1T runs database, apply event selections from LAX (Lichens for Analyzing XENON1T) or from custom built references and load metadata from the slow control and trigger monitor databases. HAX is, therefore, one of the first and most important tools one has to learn to be able to look into XENON1T data.

The MC code may run remotely with OSG resources or locally, selecting the type of simulation script that best suits the needs of the user.

A Monte Carlo production can stop in any of the above steps accordingly to the purpose of the study at hands. For instance, the main output for calibration are only energy based and only need simulations up to de nSort stage. On the other hand, if one wants to study the analysis event selection in MC data, a full-chain simulation must be performed. These are the cases of the MC data shown in Section 3.2 and Section 3.3.2, respectively.

A.2. Analysis framework

A.2.1. Data from simulation

In order to extract information from Geant4 or nSort stages of simulation for the mentioned sections, a ROOT reading script was used, transcribed bellow in pseudo-code:

Listing A.1: Script to load data from *Geant4* simulations

```
1 simpath = '<simpath>'
2 datasets_sim = get_file_list(simpath)
3 dfs = []
4 for i in datasets_sim:
```

```

5     nSort_file = i + '.root'
6     f_nSort = ROOT.TFile(simpath+nSort_file)
7     tree_nSort = f_nSort.Get('events/events')
8     Nevents_nSort = tree_nSort.GetEntries()
9
10    treedata= tree2array(tree_nSort, branches=['eventid',
11                                             'type',
12                                             'PreStepEnergy',
13                                             'xp',
14                                             'yp',
15                                             'zp',
16                                             'ed',
17                                             'e_pri',
18                                             ])
19    print('done')
20    _data = pd.DataFrame(treedata)
21    _data['pre_step_n'] = _data.PreStepEnergy.str[0]
22    dfs.append(_data)
23    data = pd.concat(dfs)

```

The output of the above script is a Pandas DataFrame with 8 columns: eventid, type, PreStepEnergy – energy of the particle before a given interaction, xp - x position of a particle, yp - y position of a particle, zp - z position of a particle, ed - deposited energy of a particle in a given interaction, e_pri - energy of the primary neutron and NR - 1 if the interaction is a NR, 0 if it is ER). Except e_pri, which is just one float value per event, all the other columns have N-value size lists, where each value is a recorded interaction from the same chain of events. The analysis done in Section 3.2 is done based on these parameters.

For reference, the script to generate Figure 3.7 is the following:

Listing A.2: Script to generate a plot of the spatial distribution of simulated NR and ER first scatters from a NG simulation (Figure 3.7)

```

1 NR = data[data.NR.str[0] == 1]
2 ER = data[data.NR.str[0] == 0]
3 fig = plt.figure(figsize = (24,16))
4 ax1 = plt.subplot2grid((2,3), (0,0), colspan=2, rowspan=2)
5
6 hist1 = plt.hist2d(data.X.str[0], data.Y.str[0], bins = 700, cmin = 1,\
7                  norm=LogNorm(vmin=1, vmax=np.nanmax(np.array([np.ravel(
8                  hist1[0]))]))))
8 tlt1 = plt.title('All_1st_scatters', fontsize = 30)

```

```

9  tlt1.set_position([.5,1.02])
10 plt.xlabel('x_(cm)')
11 plt.ylabel('y_(cm)')
12 plt.colorbar(label = 'events')
13 plt.gca().set_aspect('equal', adjustable='box')
14
15 ax2 = plt.subplot2grid((2,3), (0,2), colspan=1, rowspan=1)
16 hist2 = plt.hist2d(ER.X.str[0], ER.Y.str[0], bins = 700, cmin = 1,\
17                  norm=LogNorm(vmin=1, vmax=np.nanmax(np.array([np.ravel(
18                      hist1[0]) ]))))
19 tlt2 = plt.title('ER_1st_scatters')
20 tlt2.set_position([.5,1.02])
21 plt.xlabel('x_(cm)')
22 plt.ylabel('y_(cm)')
23 plt.gca().set_aspect('equal', adjustable='box')
24
25 ax3 = plt.subplot2grid((2,3), (1,2), colspan=1, rowspan=1)
26 hist3 = plt.hist2d(NR.X.str[0], NR.Y.str[0], bins = 700, cmin = 1,\
27                  norm=LogNorm(vmin=1, vmax=np.nanmax(np.array([np.ravel(
28                      hist1[0]) ]))))
29 tlt3 = plt.title('NR_1st_scatters')
30 tlt3.set_position([.5,1.02])
31 plt.xlabel('x_(cm)')
32 plt.ylabel('y_(cm)')
33 plt.gca().set_aspect('equal', adjustable='box')
34
35 plt.savefig('nSortspacial.png', format='png', dpi=100, bbox_inches='tight')
36 plt.show()

```

For simulated data coming from full-chain simulations the process is much similar to real taken data because it has been processed by PAX and can be managed through HAX. The main difference comes in telling HAX where to look for the data: instead of search the XENON1T runs databases, it must be directly pointed to the simulation output directory where the PAX-processed files are located. From this point forward the process is the same as the one described below, for real data.

A.2.2. Data from the XENON1T detector

In the case of real data analysis, the core part is also done in a Python and Pandas friendly environment, using DataFrames. In order to load the DataFrames, the HAX custom package is used:

Listing A.3: Script to load XENON1T data

```
1 import hax
2 hax.init(experiment='XENON1T',
3         pax_version_policy = 'latest',
4         main_data_paths= ['/ <path_to_main_data>'],
5         minitree_paths = ['/ <path_to_minitrees>'],
6         )
7 datasets = hax.runs.datasets
8
9 dataset_select = datasets[(datasets['source__type']=='neutron_generator')
10                          ]
11 run_numbers = dataset['number'].values
12 for dset in run_numbers:
13     df_temp = hax.minitrees.load(dset,
14                                 treemakers = tmakers, #list with
15                                             treemakers names
16                                 preselection = cs1 <200)
17     dfs.append(df_temp)
18 data = pd.concat(dfs)
```

The output of the above script is a DataFrame with a row for each event and a column for each loaded parameter of said event. The parameters to load are defined by which minitree is called. If the minitree is absent in '`/ < path_to_minitrees >`', it is created (as long as the user has writing permissions on the directory).

The next step in analysis is usually refine the loaded data with event selection cuts. Another already mentioned package, called LAX, stores updated versions of each cut and works with HAX to apply them:

Listing A.4: Script to process loaded data with LAX

```
1 import lax
2 cutlist= [lax.cut1, lax.cut2, lax.cut3, etc ...]
3 for cut in (cut_list):
4     df = cut.process(df)
5 df_cut = df.copy()
6 for cut in (cut_list):
```

```
7 df_cut = hax.cuts.selection(df_cut, df_cut[cut.name], cut.name)
```

The event selection is a two step process, as can be seen in the above script:

- For each cut, check if each event passes the cut and store the result (boolean) in a new column in the DataFrame.
- For each cut, remove from the dataset any event that didn't pass the cut (False in the created column).

The result is a new (or the same if the user chooses the same variable name) DataFrame with only the event that passed the selected LAX cuts.

From this point forward the analysis process diverges based on the end goal. To the results presented in this work, apart from plotting the standard variables (position, cS1, cS2), the main writing of code was put into studying leakage event and their relation with distance to source (Figure 3.13) and on the band percentiles fit, from data selection to computing the binned percentiles and fitting the results (Figure 3.15, Figure 3.16 and Figure 3.17). The functions written for these calculations and analysis are as follows: versions of each cut and works with HAX to apply them:

Listing A.5: Script to compute the ratio between leakage and non-leakage event in a binned histogram (used in Figure 3.13)

```
1 def get_leakage_ratio(_data_cut, r_scan):
2     leakage_ratio = []
3     leakage_ratio_err = []
4
5     for r in r_scan:
6         N_is = len(_data_cut[( _data_cut['dts'] < r) &
7                               ( _data_cut['is_leakage'] )])
8         N_tot = len(_data_cut[( _data_cut['dts'] < r)])
9         N_is_err = np.sqrt(N_is)
10        N_tot_err = np.sqrt(N_tot)
11
12        leakage_ratio.append(N_is/N_tot)
13        leakage_ratio_err.append(np.sqrt(np.power(N_is_err/N_tot,2) + np.
14                                         power(N_is*N_tot_err/np.power(N_tot,2),2)))
15
16    leakage_ratio = np.array(leakage_ratio)
17    leakage_ratio_err = np.array(leakage_ratio_err)
18    return leakage_ratio, leakage_ratio_err
```


Listing A.6: Scripts to compute the binned percentiles of a given histogram, applied to the 5th, 50th and 95th percentiles and fitting the results to the empirical function shown in equation 3.4.

```

1 def get_percentile_bin(hist, xbinnumber, percentage):
2     ybinsize = hist[2][1] - hist[2][0]
3     ybins_middle = hist[2][-1] + ybinsize/2
4     size = len(hist[0][xbinnumber])
5     cumsum = np.cumsum(hist[0][xbinnumber])
6     totalsum = cumsum[-1]
7     for n in range(size):
8         nsum = cumsum[n]
9         perc = nsum/totalsum *100
10        if perc >= percentage -0.00001:
11            return ybins_middle[n]
12    return None
13
14 def get_percentile_all(df_cut, percentsneeded = [5,95,50], bins=50):
15     hist = np.histogram2d(df_cut['cs1'], np.log10(df_cut['cs2_bottom'] /
16         df_cut['cs1']),
17         bins=bins,
18         range = [[1,150],[0,3]])
19     ans = {'bins':bins}
20     for percent in percentsneeded:
21         _perc_list = []
22         for xbin in range(len(hist[0])):
23             _perc_list.append(get_percentile_bin(hist, xbin, percent))
24         ans[percent] = np.array(_perc_list)
25     return ans
26
27 def fit_function(x,a,b,c,d):
28     ans = a*np.exp(-x/b) + c + d*x
29     return ans
30
31 def get_fit_values(percentiles, function = fit_function_SR1):
32     perc5 = percentiles[5]
33     perc50 = percentiles[50]
34     perc95 = percentiles[95]
35
36     fit5 = curve_fit(function_SR1, np.linspace(0.1,150, len(perc5)),
37         perc5, p0=[28.12,0.687,1.38,0.0021,0.45])
38     fit50 = curve_fit(function_SR1, np.linspace(0.1,150, len(perc50)),
39         perc50, p0=[28.12,0.687,1.38,0.0021,0.45])

```

```
37     fit95 = curve_fit(fit_function_SR1, np.linspace(0.1, 150, len(perc95)),  
38                     perc95, p0=[28.12, 0.687, 1.38, 0.0021, 0.45])  
39     return fit5, fit50, fit95
```

Bibliography

- [1] F. Zwicky. Spectral displacement of extra galactic nebulae. *Helv. Phys. Acta*, 6:110–127, 1933.
- [2] F. Zwicky. *Astrophys. J.*, 86:217, 1936.
- [3] M. Girardi. *Astrophys. J.*, 530:62, 2000.
- [4] V. C. Rubin and W. K. Ford. Rotation of the andromeda nebula from a spectroscopic survey of emission regions. *Astrophys. J.*, 159:379, 1970.
- [5] K. G. Begeman, A. H. Broeils, and R. H. Sanders. Extended rotation curves of spiral galaxies: dark haloes and modified dynamics. *Monthly Notices of the Royal Astronomical Society*, 249(3):523–537, 1991.
- [6] E. Pécontal, T. Buchert, Ph. Di Stefano, Y. Copin, and K. Freese. Review of observational evidence for dark matter in the universe and in upcoming searches for dark stars. *European Astronomical Society Publications Series*, 36:113–126, 2009.
- [7] P. A. R. Ade et al. Planck 2015 results. XIII. Cosmological parameters. *Astron. Astrophys.*, 594:A13, 2016.
- [8] R. Adam and others (Planck Collaboration). Planck 2015 results. i. overview of products and scientific results. *Astron. Astrophys.*, 594:A1, 2016.
- [9] Andrew Liddle. *An Introduction to Modern Cosmology (2nd ed.)*. Wiley, 2003.
- [10] Andre Maeder. An alternative to the Λ CDM model: The case of scale invariance. *Astrophys. J.*, 834(2), 2017.
- [11] Mordehai Milgrom. MOND theory. *Can. J. Phys.*, 93(2):107–118, 2015.
- [12] Constantinos Skordis. The tensor-vector-scalar theory and its cosmology. *Classical and Quantum Gravity*, 26(14):143001, 2009.

- [13] David P. Bennett et al. The First data from the MACHO experiment. In *Proceedings, 16th Texas Symposium on Relativistic Astrophysics and 3rd Particles, Strings, and Cosmology Symposium (Texas/PASCOS 92): Berkeley, California, December 13-18, 1992, 1992*. [Annals N. Y. Acad. Sci.688,612(1993)].
- [14] C. Afonso et al. Limits on galactic dark matter with 5 years of eros smc data. *Astron. Astrophys.*, 400:951–956, 2003.
- [15] R. D. Peccei and Helen R. Quinn. Cp conservation in the presence of instantons. *Phys. Rev. Lett.*, 38:1440–1443, 1977. [,328(1977)].
- [16] K. Zioutas et al. First results from the cern axion solar telescope (cast). *Phys. Rev. Lett.*, 94:121301, 2005.
- [17] N. et all (ADMX Collaboration) Du. Search for invisible axion dark matter with the axion dark matter experiment. *Phys. Rev. Lett.*, 120, Apr 2018.
- [18] Dmitry et all (CASPEr Collaboration) Budker. Proposal for a Cosmic Axion Spin Precession Experiment (CASPEr). *Phys. Rev.*, X4(2):021030, 2014.
- [19] D. S. Akerib et al. First Searches for Axions and Axionlike Particles with the LUX Experiment. *Phys. Rev. Lett.*, 118(26):261301, 2017.
- [20] E. Aprile et al. First Axion Results from the XENON100 Experiment. *Phys. Rev.*, D90(6):062009, 2014. [Erratum: *Phys. Rev.*D95,no.2,029904(2017)].
- [21] Achille Corsetti and Pran Nath. SUSY dark matter. In *Proceedings, 14th Rencontres de Physique de la Vallee d’Aoste: La Thuile, Italy, February 27-March 4, 2000*, pages 583–597, 2000.
- [22] Kim Griest. Cross sections, relic abundance, and detection rates for neutralino dark matter. *Phys. Rev. D*, 38:2357–2375, Oct 1988.
- [23] Robert J. Scherrer and Michael S. Turner. On the relic, cosmic abundance of stable, weakly interacting massive particles. *Phys. Rev. D*, 33:1585–1589, Mar 1986.
- [24] Jonathan L. Feng. Dark Matter Candidates from Particle Physics and Methods of Detection. *Ann. Rev. Astron. Astrophys.*, 48:495–545, 2010.
- [25] Alison Elliot. Dark matter searches with the ATLAS detector. *EPJ Web Conf.*, 158:01007, 2017.

- [26] Adish Vartak. Dark matter search in CMS. In *Proceedings, 52nd Rencontres de Moriond on Very High Energy Phenomena in the Universe: La Thuile, Italy, March 18-25, 2017*, pages 225–233, Geneva, 2017. CERN, CERN.
- [27] Louis E. Strigari. Galactic searches for dark matter. *Physics Reports*, 531(1):1 – 88, 2013. Galactic searches for dark matter.
- [28] M. et al. Fermi-Lat Collaboration Ackermann. Dark matter constraints from observations of 25 Milky Way satellite galaxies with the Fermi Large Area Telescope. *Phys. Rev.*, D89:042001, 2014.
- [29] M. Aguilar et al. AMS Collaboration. The alpha magnetic spectrometer (ams) on the international space station: Part i – results from the test flight on the space shuttle. *Physics Reports*, 366(6):331 – 405, 2002.
- [30] M. G. Aartsen et al. Search for Neutrinos from Dark Matter Self-Annihilations in the center of the Milky Way with 3 years of IceCube/DeepCore. *Eur. Phys. J.*, C77(9):627, 2017.
- [31] H. Abdallah et al. Search for γ -Ray Line Signals from Dark Matter Annihilations in the Inner Galactic Halo from 10 Years of Observations with H.E.S.S. *Phys. Rev. Lett.*, 120(20):201101, 2018.
- [32] Jeffrey Peter Filippini. *A Search for WIMP Dark Matter Using the First Five-Tower Run of the Cryogenic Dark Matter Search*. PhD thesis, University of California, Berkeley, 2008.
- [33] R. Agnese et al. Low-mass dark matter search with CDMSlite. *Phys. Rev.*, D97(2):022002, 2018.
- [34] E. Armengaud et al. Final results of the EDELWEISS-II WIMP search using a 4-kg array of cryogenic germanium detectors with interleaved electrodes. *Phys. Lett.*, B702:329–335, 2011.
- [35] J. Schieck et al. Direct Dark Matter Search with the CRESST II Experiment. *PoS*, ICHEP2016:217, 2016.
- [36] P. et al. DarkSide Collaboration Agnes. Low-mass dark matter search with the darkside-50 experiment. *Phys. Rev. Lett.*, 121:081307, Aug 2018.
- [37] R. Bernabei et al. First model independent results from DAMA/LIBRA-phase2. 2018.

- [38] E. et al. Aprile. Dark matter search results from a one ton-year exposure of xenon1t. *Phys. Rev. Lett.*, 121:111302, Sep 2018.
- [39] D. S. et al. Akerib. Limits on spin-dependent wimp-nucleon cross section obtained from the complete lux exposure. *Phys. Rev. Lett.*, 118:251302, Jun 2017.
- [40] G. Bellini et al. Cosmic-muon flux and annual modulation in Borexino at 3800 m water-equivalent depth. *JCAP*, 1205:015, 2012.
- [41] W. R. Leo. *Techniques for Nuclear and Particle Physics Experiments: A How to Approach*. 1987.
- [42] J.H. Hubbell and S.M. Seltzer. Tables of x-ray mass attenuation coefficients and mass energy-absorption coefficients (version 1.4), 2004.
- [43] Anna-Leena Manninen. *Clinical applications of radiophotoluminescence (RPL) dosimetry in evaluation of patient radiation exposure in radiology: determination of absorbed and effective dose*. PhD thesis, 2014.
- [44] Glenn F Knoll. *Radiation detection and measurement*. John Wiley & Sons, 2010.
- [45] RL Platzman. Total ionization in gases by high-energy particles: An appraisal of our understanding. *The International Journal of Applied Radiation and Isotopes*, 10(2-3):116–127, 1961.
- [46] E Aprile and T Doke. Liquid xenon detectors for particle physics and astrophysics. *Reviews of Modern Physics*, 82(3):2053, 2010.
- [47] Teresa Marrodán Undagoitia and Ludwig Rauch. Dark matter direct-detection experiments. *Journal of Physics G: Nuclear and Particle Physics*, 43(1):013001, 2016.
- [48] D. S. Akerib et al. Liquid xenon scintillation measurements and pulse shape discrimination in the LUX dark matter detector. *Phys. Rev.*, D97(11):112002, 2018.
- [49] F. Neves, A. Lindote, A. Morozov, V. Solovov, C. Silva, P. Bras, J. P. Rodrigues, and M. I. Lopes. Measurement of the absolute reflectance of polytetrafluoroethylene (PTFE) immersed in liquid xenon. *JINST*, 12(01):P01017, 2017.
- [50] Aprile, E. et al. (XENON Collaboration). The xenon1t dark matter experiment. *Eur. Phys. J. C*, 77(12):881, 2017.
- [51] T. Doke, A. Hitachi, S. Kubota, A. Nakamoto, and T. Takahashi. Estimation of fano factors in liquid argon, krypton, xenon and xenon-doped liquid argon.

- Nuclear Instruments and Methods*, 134(2):353 – 357, 1976.
- [52] A.J.P.L. Policarpo. Ionizations scintillation detectors. *Nuclear Instruments and Methods in Physics Research*, 196(1):53 – 62, 1982.
- [53] E. Aprile, K. L. Giboni, P. Majewski, Kaixuan Ni, and M. Yamashita. Proportional light in a dual-phase xenon chamber. *IEEE Transactions on Nuclear Science*, 51(5):1986–1990, Oct 2004.
- [54] Tadayoshi Doke, Akira Hitachi, Jun Kikuchi, Kimiaki Masuda, Hiroyuki Okada, and Eido Shibamura. Absolute scintillation yields in liquid argon and xenon for various particles. *Japanese journal of applied physics*, 41(3R):1538, 2002.
- [55] A. Hitachi, T. Doke, and A. Mozumder. Luminescence quenching in liquid argon under charged-particle impact: Relative scintillation yield at different linear energy transfers. *Phys. Rev. B*, 46:11463–11470, Nov 1992.
- [56] G. Plante, E. Aprile, R. Budnik, B. Choi, K.-L. Giboni, L. W. Goetzke, R. F. Lang, K. E. Lim, and A. J. Melgarejo Fernandez. New measurement of the scintillation efficiency of low-energy nuclear recoils in liquid xenon. *Phys. Rev. C*, 84:045805, Oct 2011.
- [57] D. S. Akerib et al. Low-energy (0.7-74 keV) nuclear recoil calibration of the LUX dark matter experiment using D-D neutron scattering kinematics. 2016.
- [58] E. et al. Aprile. Response of the xenon100 dark matter detector to nuclear recoils. *Phys. Rev. D*, 88:012006, Jul 2013.
- [59] Zach Green. Er and nr light/charge yield posteriors. Xenon Collaboration internal note, 2018.
- [60] J. Angle et al. First Results from the XENON10 Dark Matter Experiment at the Gran Sasso National Laboratory. *Phys. Rev. Lett.*, 100:021303, 2008.
- [61] E. Aprile et al. Dark Matter Results from 225 Live Days of XENON100 Data. *Phys. Rev. Lett.*, 109:181301, 2012.
- [62] E. Aprile et al. First Dark Matter Search Results from the XENON1T Experiment. *Phys. Rev. Lett.*, 119(18):181301, 2017.
- [63] P. Barrow et al. Qualification Tests of the R11410-21 Photomultiplier Tubes for the XENON1T Detector. *JINST*, 12(01):P01024, 2017.

- [64] E. Aprile et al. Physics reach of the xenon1t dark matter experiment. *Journal of Cosmology and Astroparticle Physics*, 2016(04):027, 2016.
- [65] Hardy Simgen. The 222rn pie: Distribution of 222rn sources in xenon1t. Xenon Collaboration internal note, April 2017.
- [66] R. F. Lang, J. Pienaar, E. Hogenbirk, D. Masson, R. Nolte, A. Zimbal, S. Röttger, M. L. Benabderrahmane, and G. Bruno. Characterization of a deuterium–deuterium plasma fusion neutron generator. *Nucl. Instrum. Meth.*, A879:31–38, 2018.
- [67] S. Agostinelli et al. Geant4—a simulation toolkit. *Nuclear Instruments and Methods in Physics Research Section A: Accelerators, Spectrometers, Detectors and Associated Equipment*, 506(3):250 – 303, 2003.
- [68] Jacques Pienaar. Detailed neutron generator simulation. Xenon Collaboration internal note, 2013.
- [69] Jacques Pienaar. Producing fusion spectra for the neutron generator. Xenon Collaboration internal note, 2017.
- [70] Ruth Pordes et al. The Open Science Grid. *J. Phys. Conf. Ser.*, 78:012057, 2007.
- [71] Zeev Alfassi. *Activation analysis*, volume 2. CRC Press, 1990.
- [72] Roland Diehl. Nucleosynthesis and gamma-ray line spectroscopy with integral. *arXiv preprint arXiv:1202.0481*, 2012.
- [73] M. P. Unterweger, D. D. Hoppes, F. J. Schima, and J. S. Coursey. Radionuclide half-life measurements data, 2016.
- [74] Georges Audi, O Bersillon, J Blachot, and AH Wapstra. The nubase evaluation of nuclear and decay properties. *Nuclear Physics A*, 729(1):3–128, 2003.
- [75] E Aprile et al. Analysis of the xenon100 dark matter search data. *Astroparticle Physics*, 54:11–24, 2014.
- [76] Jelle Aalbers. *Dark Matter Search with XENON1T*. PhD thesis, Universiteit van Amsterdam, Amsterdam, 2018.
- [77] Christopher Tunnel. Interaction peak biggest. Xenon Collaboration internal note, 2017.

- [78] Jelle Alberts et al. Digitizer, trigger, and processor efficiency. Xenon Collaboration internal note, 2017.
- [79] Adam Brown and Shingo Kazama. A cs2 area fraction top cut for sr1. Xenon Collaboration internal note, 2018.
- [80] Jelle Alberts, Yuehuan Wei, and Tianyu Zhu. Drift and diffusion in xenon1t. Xenon Collaboration internal note, 2017 - 2018.
- [81] Tianyu Zhu. S2 pattern likelihood cut tuning for sr1. Xenon Collaboration internal note, 2017 - 2018.
- [82] Daniel Coderre, Jelle Alberts, and Diego Ramírez. S2tailcut in sr1. Xenon Collaboration internal note, 2017.
- [83] Tianyu Zhu. Single scatter (s2) cut sr1 summary. Xenon Collaboration internal note, 2017.
- [84] Ricardo Peres. Ng 2018 data analysis. Xenon Collaboration internal note, 2018.
- [85] Daniel Coderre. Daq veto cut for science run 1. Xenon Collaboration internal note, 2017.
- [86] Darryl Masson. Updates for s1areafractiontop cut. Xenon Collaboration internal note, 2017 - 2018.
- [87] Fei Gao and Evan Shockley. Reducing single electron s2s with ml approach. Xenon Collaboration internal note, 2018.
- [88] Julien Wolf. S1 maxpmt cut - science run 1. Xenon Collaboration internal note, 2017.
- [89] Jacques Pienaar. S1singlscatter cut and its validity for sr1. Xenon Collaboration internal note, 2017.
- [90] The SciPy community. `scipy.optimize.curve_fit` module, 2016. https://docs.scipy.org/doc/scipy/reference/generated/scipy.optimize.curve_fit.html.
- [91] Python Software Foundation. Python3. <https://www.python.org/>.
- [92] Patrick de Perio. Er and nr band lines. Xenon Collaboration internal note, 2018.
- [93] Guillaume Plante. The xenonnt project. Dark Matter 2016 - UCLA, 2016.

-
- [94] Aprile et al. XENONnT at LNGS. 2017.
- [95] D. S. Akerib et al. Projected WIMP Sensitivity of the LUX-ZEPLIN (LZ) Dark Matter Experiment. 2018.
- [96] N. Ackerman et al. Observation of Two-Neutrino Double-Beta Decay in ^{136}Xe with EXO-200. *Phys. Rev. Lett.*, 107:212501, 2011.
- [97] Ricardo Peres. Study of shaping rings and their geometry for xenonnt. Xenon Collaboration internal note, 2018.
- [98] COMSOL INC. Comsol multiphysics[®].
- [99] Junji Naganoma. resistive chain tuning effect (example). Xenon Collaboration internal note, 2017.
- [100] Nikolina Sarcevic. Field shaping elements: Conclusion. Xenon Collaboration internal note, 2018.
- [101] James Richard Verbus. *An Absolute Calibration of Sub-1 keV Nuclear Recoils in Liquid Xenon Using D-D Neutron Scattering Kinematics in the LUX Detector*. PhD thesis, Brown University, Rhode Island, 2016.

